Spring 2014

PROBABILISTIC FAULT DETECTION AND DIAGNOSTICS FOR PACKAGED AIR-CONDITIONER OUTDOOR-AIR ECONOMIZERS

Andrew L. Hjortland
Purdue University

Graduate School ETD Form 9
(Revised 01/14)

PURDUE UNIVERSITY
GRADUATE SCHOOL
Thesis/Dissertation Acceptance

This is to certify that the thesis/dissertation prepared

By Andrew Leroy Hjortland

Entitled
Probabilistic Fault Detection and Diagnostics for Packaged AIr-Conditioner Outdoor-Air Economizers

For the degree of Master of Science in Mechanical Engineering

Is approved by the final examining committee:

James E. Braun

Eckhard A. Groll

William T. Horton

To the best of my knowledge and as understood by the student in the *Thesis/Dissertation Agreement. Publication Delay, and Certification/Disclaimer (Graduate School Form 32)*, this thesis/dissertation adheres to the provisions of Purdue University's "Policy on Integrity in Research" and the use of copyrighted material.

James E. Braun

Approved by Major Professor(s): _____

Approved by: David C. Anderson 03/07/2004

Head of the Department Graduate Program Date

PROBABILISTIC FAULT DETECTION AND DIAGNOSTICS FOR PACKAGED AIR-CONDITIONER OUTDOOR-AIR ECONOMIZERS

A Thesis

Submitted to the Faculty

of

Purdue University

by

Andrew L. Hjortland

In Partial Fulfillment of the

Requirements for the Degree

of

Master of Science in Mechanical Engineering

May 2014

Purdue University

West Lafayette, Indiana

To my parents

TABLE OF CONTENTS

LIST OF TABLES

Table Page

LIST OF FIGURES

Figure Page

Figure Page

Figure Page

Figure Page

SYMBOLS

COP	coefficient of performance for RTU cooling cycle
h	enthalpy
h_{oa}	outdoor-air enthalpy
h_{ra}	return-air enthalpy
h_{ma}	mixed-air enthalpy
h_{sa}	supply-air enthalpy
OAF	outdoor-air fraction
OAF_{ma}	estimated outdoor-air fraction based on mixed-air temperature
OAF_{sa}	estimated outdoor-air fraction based on supply-air temperature
OAF_{oad}	outdoor-air fraction based on outdoor-air damper control signal
$\dot{m}$	mass flow rate
$\dot{m}_{\text{oa}}$	outdoor-air mass flow rate
$\dot{m}_{\text{ra}}$	return-air mass flow rate
$\dot{m}_{\text{ma}}$	mixed-air mass flow rate
$\dot{m}_{\text{sa}}$	supply-air mass flow rate
$\dot{m}_{\text{sa,virtual}}$	virtual supply-air mass flow rate
ΔP	differential pressure
ΔP_{idf}	differential pressure across the indoor fan
Q	cooling load
Q_{load}	total cooling load
$Q_{\text{load,actual}}$	actual total cooling load, possibly under faulty operation
$Q_{\text{load,normal}}$	normal cooling load under normal operation
Q_{space}	cooling load not attributed to ventilation
$Q_{\text{space,actual}}$	actual cooling load not attributed to ventilation
$Q_{\text{space,normal}}$	normal cooling load not attributed to ventilation

Q_{vent}	ventilation cooling load
$Q_{\text{vent,actual}}$	actual ventilation cooling load, possibly under faulty operation
$Q_{\text{vent,normal}}$	normal ventilation cooling load under normal operation
$\dot{Q}$	cooling rate
$\dot{Q}_{\text{evap}}$	cooling capacity
$\dot{Q}_{\text{evap,actual}}$	actual available capacity
$\dot{Q}_{\text{evap,normal}}$	normal available capacity under normal operation
$\dot{Q}_{\text{vent,actual}}$	actual capacity used to cool ventilation portion of load
$\dot{Q}_{\text{vent,normal}}$	normal capacity used to cool ventilation portion of load
r	residual or degradation ratio
$r_{\text{1-9}}$	diagnosis residual
r_{COP}	efficiency impact ratio
r_{capacity}	capacity impact ratio
$r_{\Delta\text{load}}$	total run-time impact ratio
r_{space}	conditioned space load impact ratio
r_{vent}	ventilation load impact ratio
r_{SHR}	sensible heat ratio impact ratio
$r_{\Delta\text{vent}}$	ventilation load run-time impact ratio
$r_{\Delta\text{space}}$	conditioned space load run-time impact ratio
r_W	RTU energy consumption impact ratio
$x_{\text{vent,normal}}$	fraction of ventilation load to total cooling load under normal operation
Δt	run-time
Δt_{load}	total run-time required to meet cooling load
$\Delta t_{\text{load,actual}}$	actual run-time required to meeting cooling load
$\Delta t_{\text{load,normal}}$	normal run-time required to meet cooling load under normal operation
Δt_{space}	total run-time required to meet cooling load not attributed to ventilation
$\Delta t_{\text{space,actual}}$	actual run-time required to meet the conditioned space load not attributed to ventilation

$\Delta t_{\text{space,normal}}$	normal run-time required to meet the conditioned space load under normal operation
Δt_{vent}	total run-time required to meeting cooling load attributed to ventilation
$\Delta t_{\text{vent,actual}}$	actual time required to meet the ventilation cooling load
$\Delta t_{\text{vent,normal}}$	normal time required to meet the ventilation cooling load under normal operation
SHR	sensible heat ratio
$\text{SHR}_{\text{normal}}$	sensible heat ratio under normal operation
T	temperature
T_{oa}	outdoor-air temperature
$T_{\text{oa,ave}}$	9-point average outdoor-air temperature
$T_{\text{oa,meas}}$	single-point measured outdoor-air temperature
$T_{\text{oa,corr}}$	corrected single-point measured outdoor-air temperature
T_{ra}	return-air temperature
$T_{\text{ra,ave}}$	9-point average return-air temperature
$T_{\text{ra,meas}}$	single-point measured return-air temperature
T_{ma}	mixed-air temperature
$T_{\text{ma,ave}}$	16-point average mixed-air temperature
$T_{\text{ma,meas}}$	single-point measured mixed-air temperature
$T_{\text{ma,corr}}$	corrected single-point measured mixed-air temperature
T_{sa}	supply-air temperature
$T_{\text{sa,ave}}$	9-point average supply-air temperature
$T_{\text{sa,meas}}$	single-point measured supply-air temperature
$T_{\text{sa,adj}}$	adjusted single-point measured supply-air temperature
ΔT	temperature difference
ΔT_{idf}	temperature rise across the indoor fan
W_{elec}	energy consumption
$W_{\text{elec, normal}}$	RTU energy consumption under normal operation
$\dot{W}$	power

$\dot{W}_{\text{idf}}$	indoor fan power
$\dot{W}_{\text{idf,virtual}}$	virtual indoor fan power
x_{vent}	fraction of ventilation load to total cooling load
γ	normalized control signal
γ_{oad}	outdoor-air damper normalized control signal
γ_{idf}	indoor fan normalized control signal
ϕ	relative humidity
ϕ_{oa}	outdoor-air relative humidity
ϕ_{ra}	return-air relative humidity
ϕ_{ma}	mixed-air relative humidity
ϕ_{sa}	supply-air relative humidity
ψ	control signal voltage
ψ_{oad}	outdoor-air damper control signal voltage
ω	humidity ratio
ω_{oa}	outdoor-air humidity ratio
ω_{ra}	return-air humidity ratio
ω_{ma}	mixed-air humidity ratio
ω_{sa}	supply-air humidity ratio

ABBREVIATIONS

AFDD	automated fault detection and diagnosis
ASME	American Society of Mechanical Engineers
EEV	electronic expansion valve
evap	evaporator
FS	full-scale
idf	indoor fan
load	total load on RTU
ma	mixed-air
oa	outdoor-air
oad	outdoor-air damper
ra	return-air
RTU	rooftop unit
sa	supply-air
space	conditioned space
TXV	thermostatic expansion valve
vent	ventilation
VFD	variable frequency drive

ABSTRACT

Hjortland, Andrew L. M.S.M.E, Purdue University, May 2014. Probabilistic Fault Detection and Diagnostics for Packaged Air-Conditioner Outdoor-Air Economizers. Major Professor: James E. Braun, School of Mechanical Engineering.

Approximately $60\,\%$ of commercial floor space in the US is served by rooftop air-conditioners (RTUs), many of which utilize outdoor-air economizers to reduce building energy consumption [1, 2]. However, preventative maintenance in the field is uncommon for these types of units and service calls are generally only made during emergencies. Because of this, it is not uncommon for faults to persist in RTUs unnoticed, decreasing system efficiency and increasing run-time and operating costs. The result of these faults leads to an additional $15\,\%$ to $30\,\%$ energy consumption in commercial cooling equipment, according to some studies [3, 4].

Poor economizer control, economizer damper failure, and excess outdoor-air contribute to these performance degradations. In order to promote optimal RTU performance and reduce operating costs, an automated fault detection and diagnostics (AFDD) tool has been designed for RTUs with integrated economizers. Based on previously proposed methods, the proposed method advances the economizer fault detection and diagnosis components by using statistical classifiers in order to provide more robust, probabilistic fault outputs. A set of air-side virtual sensors has also been added to the method in order to expand the applicable range of conditions fault detection and diagnostics can be applied.

The proposed method is designed to be integrated into the RTU controller during manufacturing. An integrated approach was pursued in order to increase the fault detection sensitivity and to decrease the fault alarm rate by training normal performance models using laboratory test data collected using psychrometric chambers. This method is promising for RTUs since these systems are mass produced and the normal performance of one unit is representative of entire family of units.

The operational performance of the outdoor-air damper was characterized using a series of laboratory tests in order to model the expected outdoor-air fraction at different damper actuator control signals and ambient conditions. Two temperature correction models were developed in order to minimize the sensor error caused by stratification. The first correction was to the outdoor-air temperature sensor. This sensor was influenced by return-air that was recirculated back into the outdoor-air stream, an effect of economizer hood design. The second temperature correction modeled was for the single-point mixed-air temperature. At the mixed-air temperature sensor location, significant thermal stratification and non-uniform flow is present due to ineffective mixing in the RTU mixing box. Finally, the temperature rise across the indoor fan was modeled, along with the expected mass-air flow rate and power consumption of the indoor fan.

Using these models of normal performance, deviations from normal are detected using a fault detection classifier. Using a Bayesian classifier a comparison of expected and actual performance is made when the RTU operates at steady-state. Outdoor-air damper position faults and temperature sensor faults, including faults in the outdoor-air, return-air, mixed-air, or supply-air temperature measurements, are considered by the AFDD tool. After a fault has been detected, an active economizer diagnostic procedure is performed by sweeping the outdoor-air damper from the fully-closed to fully-open position. When the damper is at these positions, redundant system measurements can be compared and a set a fault diagnosis residuals can be calculated. These residuals yield unique responses to different faults when they are present in the system. Using this as a guide, faults are isolated using a statistical fault diagnosis classifier.

Experimentally collected data were used to test the effectiveness of the AFDD method under different normal and faulty conditions. The false alarm rate of the fault detection method was approximately $1.0\,\%$. The misdiagnoses rate of the diagnosis classifier for normal data was approximately $4.9\,\%$. When taken together, the overall false alarm rate of the AFDD tool was approximately $0.05\,\%$. This low false alarm rate can be attributed to the accuracy of the temperature sensor correction and outdoor-air fraction models that can be attained when using experimentally obtained training data for an individual RTU. This

also shows of the advantage of embedding diagnostics into the equipment over a tool that is applied retroactively. The diagnosis tool was also able to correctly identify greater than $90\,\%$ of the different faults studied. The most significant faults studied, stuck outdoor-air damper faults, were correctly diagnosed in $93.2\,\%$ of the fault cases.

As a first step towards determining optimal FDD thresholds, several performance tests were conducted in the laboratory in order to observe the affects of a stuck damper fault on system performance. Tests with warm, humid outdoor-air temperatures were considered. Different damper positions were tested and their impact on the outdoor-air fraction entering the system were examined. The damper faults were shown to increase system capacity and efficiency due to the higher evaporation temperature caused by the higher fraction of warm outdoor-air at the evaporator air inlet. However, a negative impact on required RTU run-time was also determined, yielding increases in required energy consumption in order to meet equivalent conditioned space loads. The cause of this increased run-time was the increased ventilation load component introduced by the opened damper. These conditions lead to a reduction in available cooling capacity to meet the space load.

1. INTRODUCTION

1.1 Fault Detection and Diagnostics

In applications where the presence of faults may lead to premature failure, increased operating costs, or other undesirable consequences, fault detection and diagnostics (FDD) tools are often implemented. The objectives of these tools are earlier detection of problems and expedited service processes that minimize the fault's impact on the system. In addition, an FDD tool may signal corrective action before further damage occurs or before the system completely fails. Generally, FDD tools have three main components: the monitoring, the detection,and the diagnostic components. The relationships or data flows between components commonly found in many FDD applications are shown for a generic application in Figure 1.1. The figure and discussion that follows is presented originally by Rossi [5]. Additional details in the following discussion were orginally presented by Katipamula and Brambley [3, 4].

In the monitoring component, one or several characteristics of a system are observed by means of sensors, control signals, or system outputs. In most cases, detection is performed passively (without interrupting the observed system's normal behavior). Examples of characteristics that could be monitored by an FDD system are a building's daily energy consumption, magnitude of a control deviation in feedback control, or the dimensions of a part produced at a manufacturing plant. In all of these cases, there is a measurement of the current status of the system which could be compared with what is expected or has been observed historically.

The comparison between the expected and correct states of a system comprises the detection component of an FDD system. Intuitively, the objective of fault detection is to determine when a fault exists. Depending on the FDD system, this can be accomplished in any number of ways. For some applications, heuristic based methods may be suitable. In

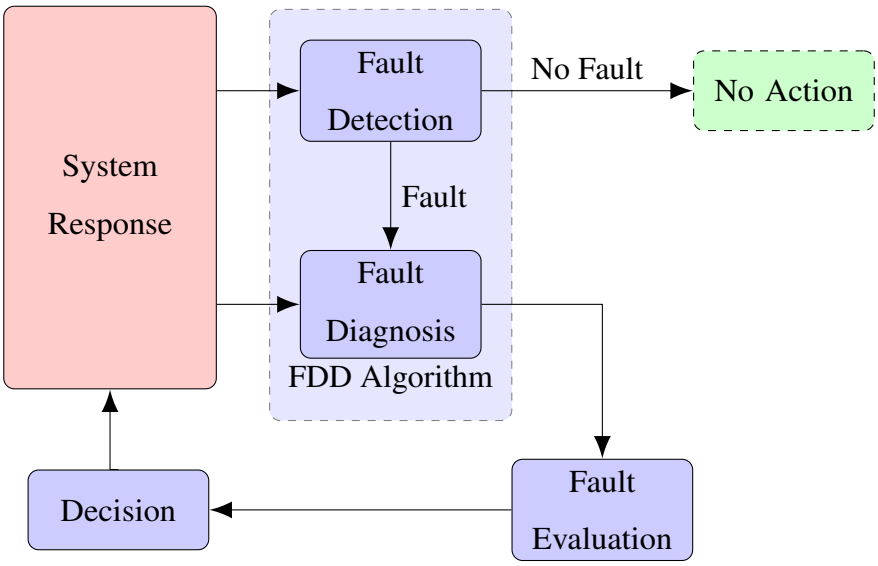

Figure 1.1. Example FDD algorithm used to monitor performance of an system whose response is affected in the presence of faults.

more critical applications, advanced statistical methods have been applied in order to detect slight deviation from the desired performance.

Fault diagnosis is a critical component of a complete FDD system because of its potential to reduce service time and costs. By isolating the cause of a fault, a service technician can spend less time determining the cause of the problem and instead simply correct the issue. Because labor costs are often one of the largest service expenses, diagnostic capability has the potential to reduce service costs significantly. Additionally, a more advanced diagnostic tool could list any required tools or replacement parts required to correct the fault, reducing the amount of time the system is offline. In the case of FDD applied to monitor the operation of a system, actual damage or increased operating costs could be diagnosed.

Using this information, preventative maintenance could be coordinated optimally to reduce these impacts. Further, a fault impact evaluation could be made in order to provide service recommendation. In applications where common faults are not critical, service equipment may not be warranted due to significant costs or minimal operational impact. Besides economic impact, other considerations sometimes need to be made before prescribing recommended action. For instance in a HVAC application, consideration about the impact on human comfort or equipment life could be considered along with operating cost impact.

FDD has been well studied and widely applied to critical applications such as the aerospace, automotive, nuclear, and process controls fields. Less effort has been focused on noncritical applications such as HVAC&R, however implementation of such tools in this field is growing. Growth in these applications can be attributed to falling cost of hardware, economic concerns, and adoption of FDD requirement standards.

In order to overcome the relatively high cost of hardware compared to the price of a packaged air conditioner, FDD methods have been designed using low-cost and virtual sensors [6, 7]. Virtual sensors enable expensive measurements such as flow rate or pressure or impossible measurements such as refrigerant charge level using lower-cost sensors. With the falling cost of computation, FDD developers have have been able to implement more complex algorithms aimed at making the tools as sensitive as possible from the limited measurements available.

Due to the presence of faults introduced during installation or developed during operation, HVAC system performance is not often optimal. This is especially true of rooftop and other packaged air conditioners since they tend not to be well-maintained [8, 9]. Moreover, equipment with economizers show high frequencies of faults causing as much as $30\,\%$ extra energy usage [10]. These reasons have made it more economically feasible for packaged air-conditioner FDD and have influenced the adoption of at least one HVAC standard requiring economizer FDD on these systems [11].

1.2 Economizer FDD Literature Review

Several economizer fault detection and diagnostics (FDD) tools have been described in the literature. Some of these methods are described in this section, including Outdoor Air/Economizer Diagnostician, Air-Handler Performance Assessment Rules, and an integrated economizer fault detection and diagnostics method [10, 12–14]. A thorough review of FDD methods for building systems in general, prior to 2005, was compiled by Katipamula and Brambley [3, 4]. A comparison of some of the economizer FDD methods is included at the end of this section.

1.2.1 Outdoor Air/Economizer Diagnostician

Brambley et al. proposed the Outdoor Air/Economizer (OAE) Diagnostician, a tool used for detecting and diagnosing ventilation and economizer problems in air handling units (AHUs) [10]. The tool detects problems using sensors that are commonly installed on AHUs and can be used on constant-volume or variable-air-volume (VAV) systems that do not use volume compensation (systems where the outdoor-air flow rate is a constant fraction of the supply-air flow rate). The diagnostician also supports integrated economizer operation (ability to use the economizer and mechanical cooling simultaneously) to meet the cooling load. The method can be applied to systems using differential or changeover control strategies based on either dry-bulb or enthalpy measurements.

The OAE Diagnostician is designed to detect faults normally not experienced by occupants or noticed by building operators. These types of faults include stuck dampers, temperature or humidity sensor failures, economizer controller failure or air flow restrictions. Based on the diagnostic information determined, a suggested action is also made by the tool detailing how to fix the problem.

The OAE Diagnostician is implemented as software that can be embedded as part of a larger building's monitoring and control system. In order to perform fault detection, the current operational state of the the system is determined using sequential logical tests first. Once the status of the AHU is known, a set of rules are evaluated on collected data to determine whether the economizer is performing correctly or incorrectly. Using the set of rules, the following diagnoses can be concluded using the rule-based method:

- low economizer flow
- high ventilation
- high economizer flow
- OK or no detection
- low ventilation
- control or other problem.

The root cause of the fault cannot be determined by the OAE Diagnostician.

In order to reduce the occurrence of false alarms and misdiagnoses, the data that are processed passes through a high-low range checking algorithm before diagnostics is performed. No steady-state detection is performed, so transient data may be processed. In order to evaluate the diagnosis rules, fault detection thresholds must be defined either using default values or manually. The choice of these values influences the methods sensitivity and false alarm rate. An additional filter is used to determine whether the outdoor-air, return-air, and mixed-air temperatures are too close to each other to perform diagnostics as these measurements are used to determine outdoor-air fraction. When these temperatures

are too close, the outdoor-air fraction cannot be calculated accurately and diagnostics is not performed.

Using simulation and field testing data, the method was proven effective by detecting known faults, including stuck damper faults [12].

1.2.2 Air-Handler Performance Assessment Rules

Schein et al. describe a method for detecting AHU faults called Air-Handler Performance Assessment Rules (APAR) [15–17]. APAR evaluates a set of rules based on energy and mass balances of various subsystems of an AHU in three steps. In Step 1, the mode of operation is determined based on the status of the heating coil valve, cooling coil valve, and mixing box damper as well as the occupancy information. Step 2 determines which rules are applicable to the current mode of operation. There are five different modes identified by the method:

1. Heating Mode
2. Economizing or "Free-Cooling" Mode
3. Integrated Cooling Mode
4. Mechanical Cooling Mode
5. Unknown Mode

After this determination, the applicable rules are evaluated and possible diagnoses of the fault are returned in Step 3.

In order to evaluate its rules, APAR requires various sensors, set points, and control signals as inputs. The sensors include outdoor-air, return-air, mixed-air, and supply-air temperatures as well as outdoor-air and return-air relative humidity when enthalpy-based economizers are used. Occupancy status and supply-air temperature set point are required along with cooling coil valve, heating coil valve, and mixing box damper control signals. This information is commonly available for AHUs controlled with a direct digital control

(DDC) system however not common in packaged air conditioning equipment. For this reason, the APAR tool is intended to be embedded in an AHU controller.

Unlike the OAE Diagnostician, which is focused on only the ventilation and economizer subsystems of an AHU, APAR is designed to detect problems in all subsystems of the AHU. APAR uses its rule set to identify the faults below.

- Stuck heating or cooling coil valves
- Stuck mixing box dampers
- Temperature sensor faults
- Design faults (such as undersized coils)
- Controller faults
- Inappropriate operator intervention

Much of the method focuses on detecting control faults since these are commonly present in AHUs installed in the field. The researchers also looked at embedding the FDD method into the controls of the AHU in order to lower cost and improve performance. Field testing was conducted by the researchers focused at detecting mechanical and control faults.

Despite being focused on AHU and not specifically economizers, APAR still is able to diagnose faults relating to economizer performance with a subset of the rules. Additionally, the method can be applied to a rooftop air-conditioner when cooling and heating coil valve faults are not considered.

1.2.3 Integrated AHU Fault Detection by Seem & House

Seem and House describe a method for integrated control and fault detection of AHUs [14]. The method uses sensors commonly installed in AHUs performance fault detection using data collected when steady-state conditions are imposed on the AHU by its sequencing logic. By using this, the method does not need to rely on a steady-state detector, however, fault detection may only be performed when the AHU sequences to a new mode.

A model-based fault detection method processes the data collected and generates residual values that can be further processed to diagnose faults. These models are similar to the APAR rule set in that they are derived from mass and energy balances within the AHU. In the presence of a fault, one or more of the calculated residuals should deviate from 0, the expected value for normal operation.

The method was assessed using simulations of 16 different faults. These faults consisted of biased temperature sensor faults, stuck and leaking damper faults, and stuck and leaking cooling or heating valve faults. Including outdoor-air damper faults, relief-air damper faults were also simulated and tested. A limitation of the method described was that only fault detection could be performed using the residuals. The authors stated that additional steps were needed in order to isolate the cause of the fault's impact on the different residuals calculated.

1.2.4 Improved Economizer FDD Method by Wichman

Wichman tested and improved the economizer diagnostics algorithm by Field Diagnostics Services, Inc. [18]. To perform this evaluation and enhancement, experimental data was collected from a rooftop unit installed with an integrated economizer. Using the experimental data, an economizer model was developed on which faults could be implemented. The provided FDD method was able to detect the following faults by evaluating a set of rules:

- outdoor-air temperature out of range
- return-air temperature out of range
- mixed-air temperature out of range
- no economizer cooling at low outdoor-air temperature
- high outdoor-air fraction at high outdoor-air temperature
- low outdoor-air fraction during occupied period
- low mixed-air temperature.

A major contribution of this work was the method proposed for improving the accuracy of the mixed-air temperature sensor [19]. Because of the size limitation of the rooftop unit, the mixed-air temperature measurement is influenced by the temperature and velocity distribution in the mixing box. Wichman determined the best ways to place combinations of mixed-air temperature sensors as well as a method to correct a single-point temperature sensor to make it more representative of the bulk mixed-air temperature.

1.2.5 Active Economizer Diagnostics Method

Fernandez et al. developed algorithms that address faults for temperature sensors, humidity sensors, and dampers in AHUs [20]. The method employs passive, observational fault detection and proactive tests for fault isolation when they are needed. The faults impact the system energy use and are frequently unnoticed. The algorithms proposed are a set of integrated flow charts that narrow down the cause of the fault using system redundancy. In addition to the FDD components, a fault correction method using mathematical compensation to fix certain sensor faults is described.

1.3 Research Objectives

Economizer fault detection and diagnostics methods previously described in the literature are mostly rule-based with limited diagnosis capability. Many economizer methods are designed primarily with built-up AHU systems in mind, rather than packaged air conditioners. The first goal is to design a economizer FDD method for rooftop air conditioners that could be embedded into its controller. The focus on embedding the method within the RTU controller enables information not readily available in retrofit applications as well as an opportunity to perform active testing in order to diagnose faults. The second goal is to design a statistical based FDD method that reports a statistical level of confidence along with the fault diagnoses. This should increase the robustness of the FDD method. Thirdly, the impacts of stuck outdoor-air dampers will be studied with respect to cooling capacity,

cycle efficiency, and system run-time. This is a first step towards determining optimal fault detection thresholds as well as optimal service recommendations.

In order to meet these goals, a rooftop air conditioner will be performance tested in order to build models to improved FDD performance. Models improving single-point temperature measurements will also be designed in order to improve the accuracy of the FDD inputs. Characterizing the performance in this way also enables implementing these models within the embedded FDD method before installation which could be beneficial for equipment manufacturers.

1.4 Thesis Organization

This chapter presented an overview of previous work in the field of fault detection and diagnostics for HVAC equipment, focused primarily on packaged air conditioners with economizers. Additionally the motivation behind and the approach taken to provide the contributions of this thesis have been presented.

Chapter 2 provides a description of the experimental set-up and testing procedure used to develop and validate the models and FDD methods produced in this thesis. A description of how faults were implemented in the system is also described.

Chapter 3 describes the physical models developed to describe normal and faulty economizer performance. These models are also validated in this chapter.

The proposed economizer AFDD method is described in Chapter 4. A description of both the fault detection algorithm as well as the active diagnostics algorithm is described and test results are presented. A development of FDD thresholds is also presented in this chapter.

Chapter 5 describes economizer fault impact models developed using laboratory test data. Impact on cooling capacity, COP, run-time are all discussed for stuck damper faults when the outdoor-air temperature and humidity is greater than the return-air conditions.

Finally, Chapter 6 summarizes the important results of the work reported in this thesis and gives recommendations for future work.

2. EXPERIMENTS AND DATA COLLECTION

2.1 Experimental Goals

In order to build a sensitive and robust FDD tool, experiments were conducted in order to characterize normal economizer performance. This included gathering data to generate models that captured outdoor-air damper behavior both when the system operated normally and during the inclusion of faults. Additionally, many data were collected in order to increase the accuracy of the mixed-air temperature measurement. For more details on these models, see Chapter 3. These experiments also provided data used to train the fault detection and diagnostics methods and evaluate their effectiveness (see Chapter 4). Thirdly, the performance of the air-conditioner under normal and faulty operation was analyzed in order to evaluate performance degradation models. Degradation in capacity, efficiency, load, and run-time were assessed using these data in Chapter 5.

2.2 Experimental Setup

2.2.1 Air-Conditioner Information

A Carrier 4-ton packaged air conditioner (known also as a rooftop unit) with an integrated economizer was used to perform the experiments. An integrated economizer is one that is packaged and controlled in combination with the mechanical cooling system [12]. The system was manufactured with variable speed indoor and outdoor fans. Control of the indoor fan was accomplished using the variable frequency drive (VFD) controller installed on the unit. The system was packaged with a thermal expansion valve, however this was replaced with an electronic expansion valve part way through testing. The rooftop unit (RTU) was installed inside a set of psychrometric chambers at Ray W. Herrick Laboratories, Purdue

University in order to simulate outdoor and indoor ambient conditions. A schematic of the installed system is shown in Figure 2.1.

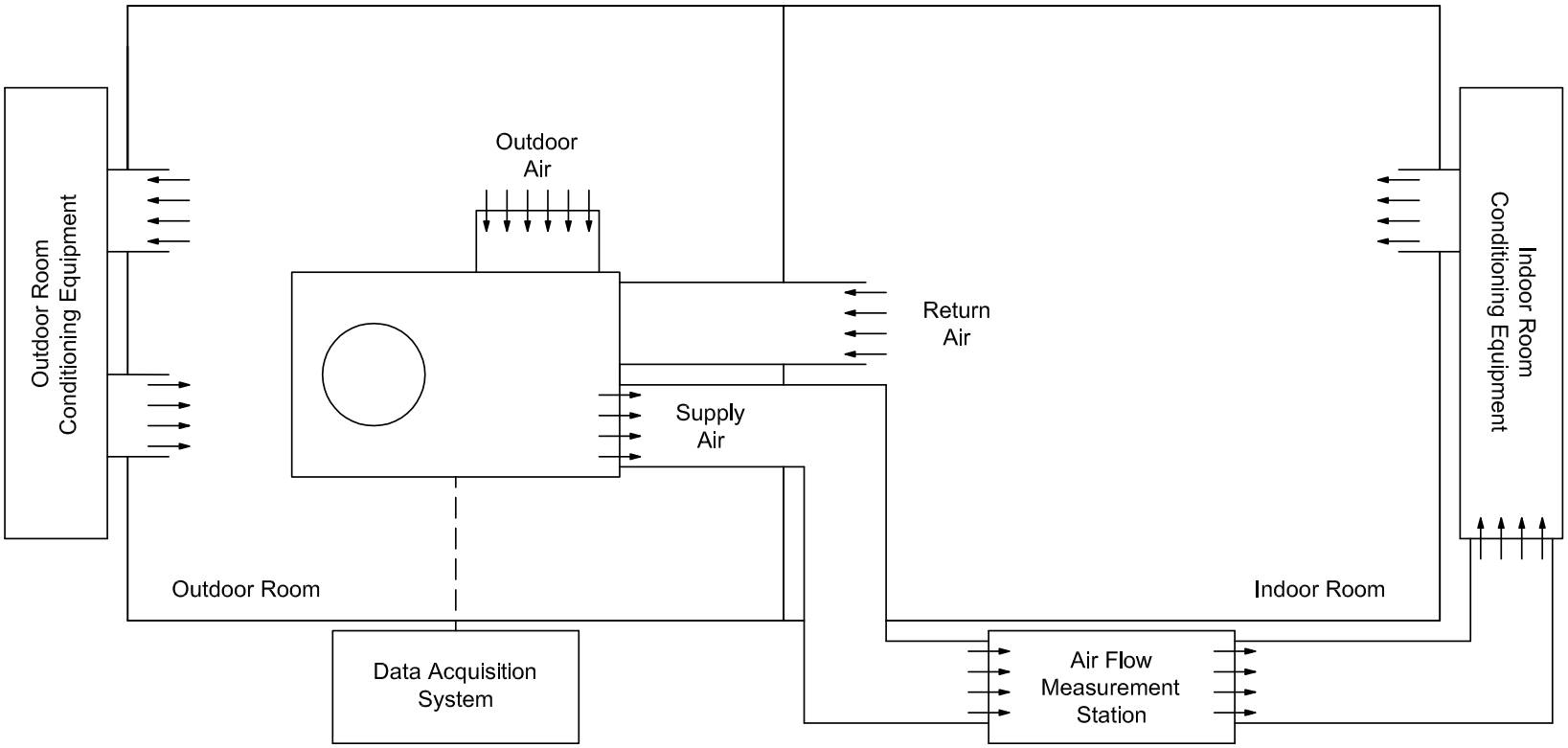

Figure 2.1. Experimental setup inside psychrometric rooms at Ray W. Herrick Laboratories.

Air ducts were used to connect the RTU to the indoor room and the air flow measurement station. The return-air duct entered the RTU at the bottom of the mixing box at one end and the indoor room at the opposite. Outdoor-air was drawn into the system using the manufactured economizer hood that also connected to the mixing box of the RTU. A supply-air duct was connected at the bottom of the RTU and was connected to the air flow measurement station. A diagram of how the ducts were connected to the RTU is shown in Figure 2.2. After the air flow measurement station, an external, variable speed fan was utilized to overcome the pressure drop created by the air flow measurement station nozzles and to achieve the range of desired air flow rates.

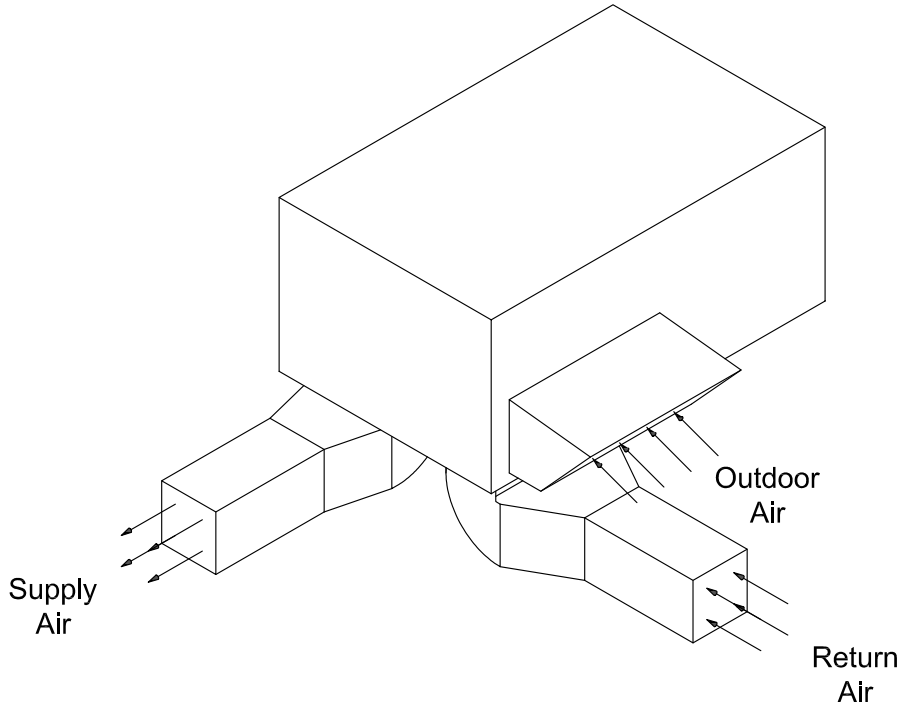

Figure 2.2. Duct configuration on RTU.

2.2.2 Instrumentation and Data Acquisition

Air-Temperature Measurements

Temperatures of the air streams were measured using equally spaced thermocouple grids at different locations of the RTU. Since the return-air and supply-air ducts had identical cross-sections, the thermocouple placement for these temperature sensors were also identical. In these air streams, a three-by-three temperature sensor grid was installed, as shown by Figure 2.3.

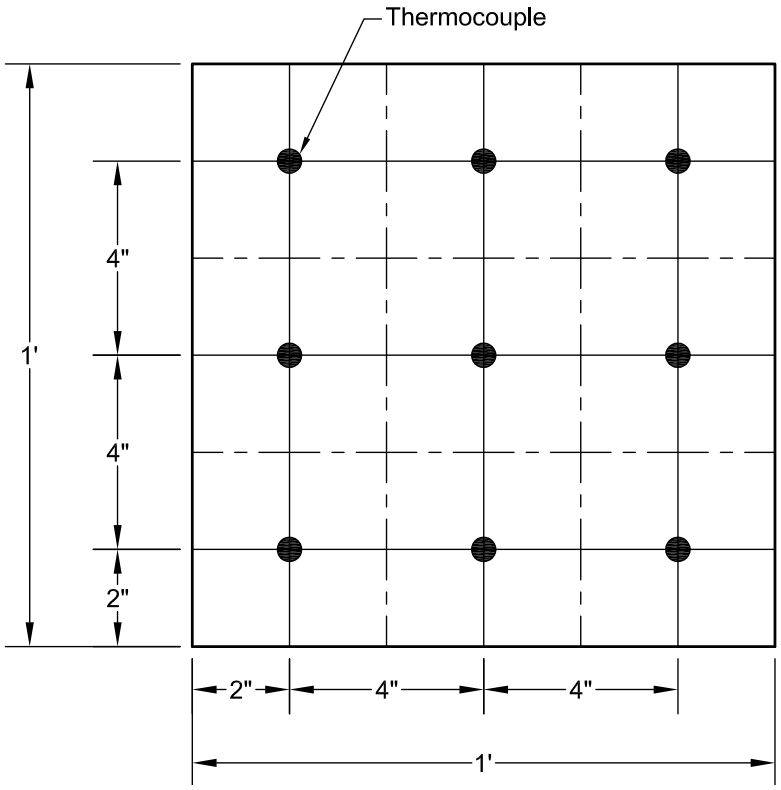

Figure 2.3. Thermocouple grid configuration for the return-air and supply-air temperature measurement.

A four-by-four thermocouple grid was used to measure the mixed-air temperature at the evaporator inlet, shown in Figure 2.4. The thermocouples were installed in the space between the air filters and the evaporator coil within the mixing box.

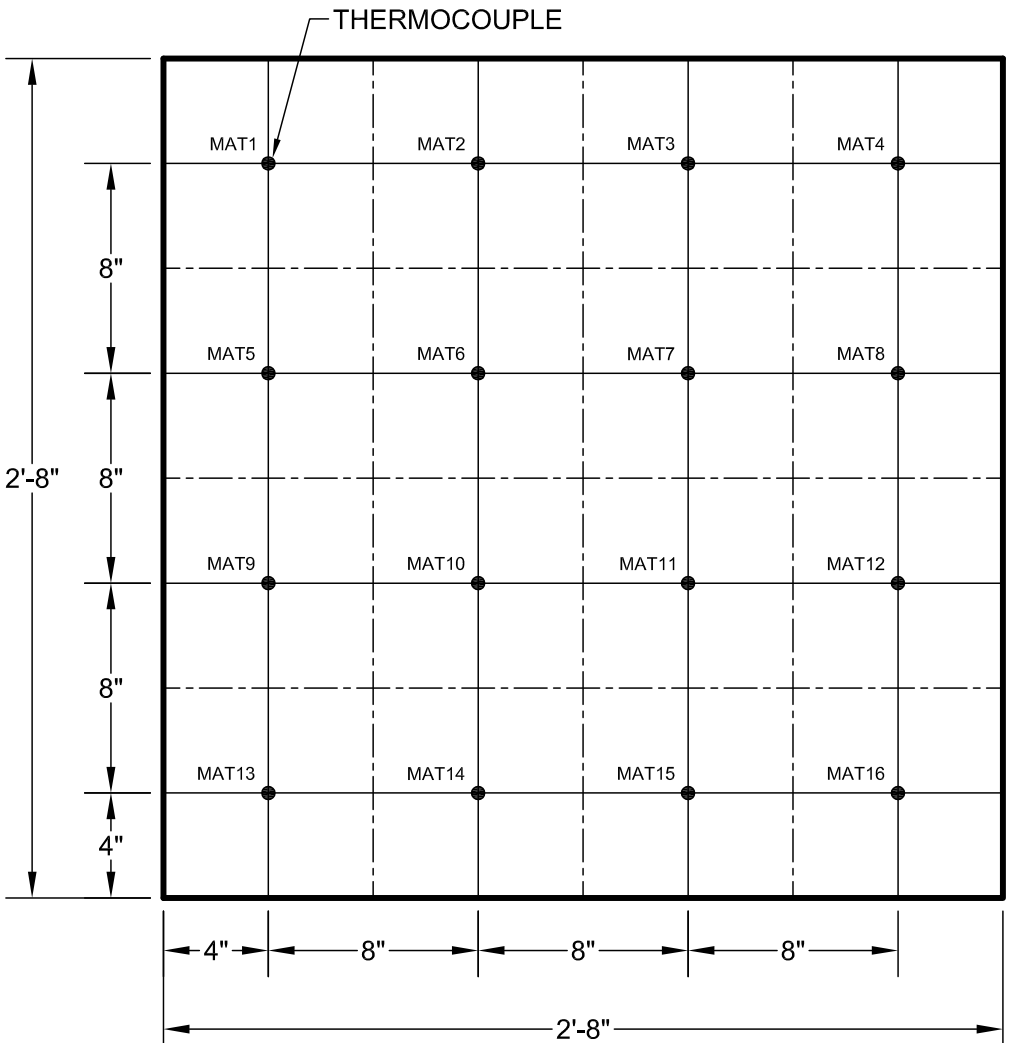

Figure 2.4. Thermocouple grid configuration for the mixed-air temperature measurement.

The outdoor-air temperature measurement was taken using a similar thermocouple grid, however the spacing was adjusted in order to comply with the economizer hood dimensions. In the economizer hood, the thermocouples were located immediately after the outdoor-air filter (sometimes known as the “squirrel cage”). The economizer hood was installed per the manufacturer’s instructions. A schematic of the outdoor-air temperature sensor grid is shown in Figure 2.5.

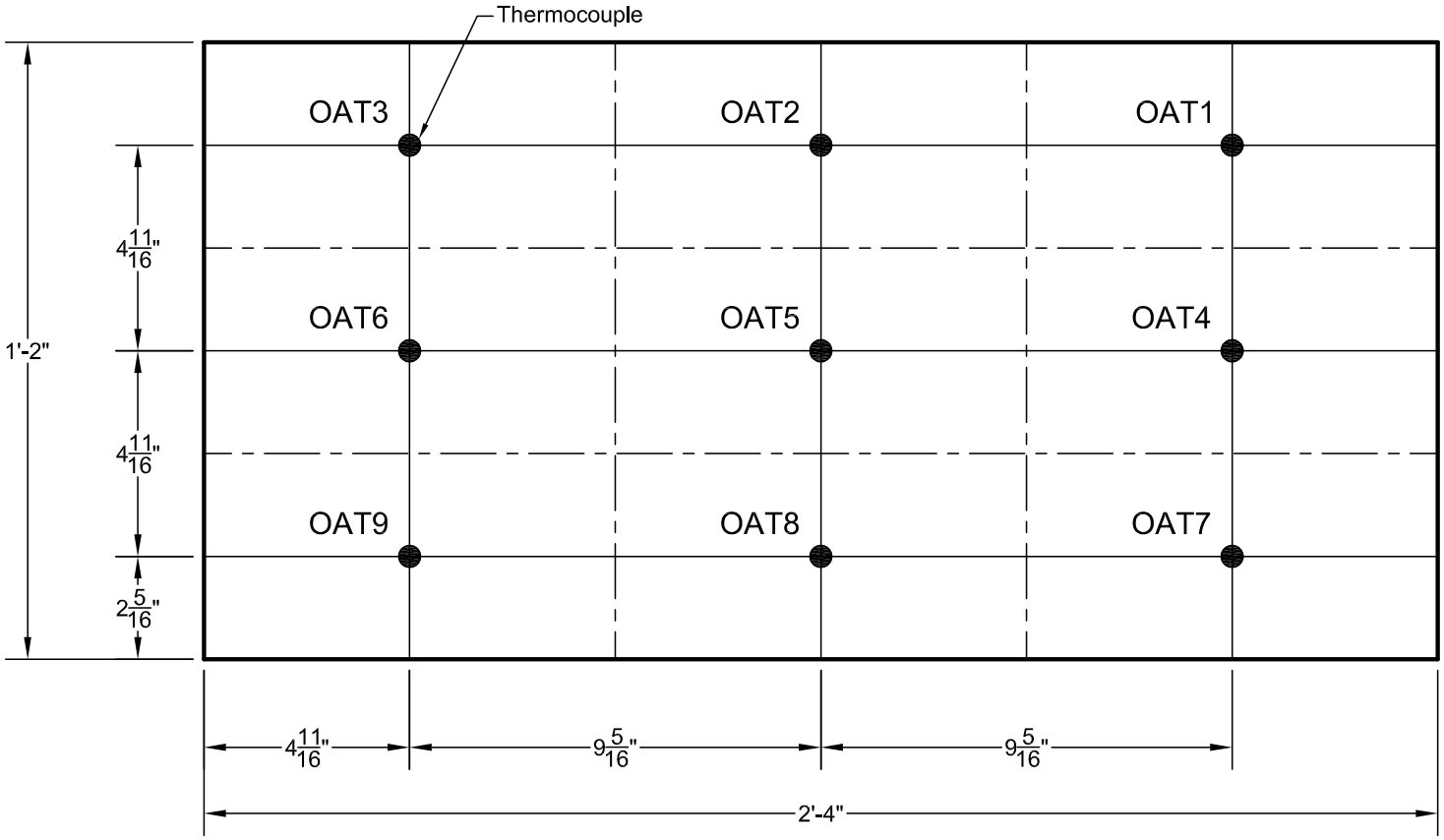

Figure 2.5. Thermocouple grid configuration for the outdoor-air temperature measurement.

The condenser air inlet and outlet temperatures were also measured using T-type thermocouple measurement grids. To measure the condenser inlet temperature, twenty thermocouples were equally spaced around the condenser air intake grill. This measurement was also used as the outdoor-air ambient temperature because its accuracy was greater than the single-point room temperature sensor used to control the psychrometric room cooling system. The condenser air outlet temperature was measured after the condenser fan on the exhaust grill using nine thermocouples in equally spaced concentric rings. The thermocouples used for all the air temperature measurements on the RTU were T-type thermocouple with a rated accuracy of $\pm 0.5\,^{\circ}\mathrm{C}$.

Using measurement grids at different locations around the RTU to measure the temperature of an air stream enables the calculation of an average temperature by calculating the simple mean of the individual sensors:

$$T_{\mathrm{x,ave}} = \frac{1}{n}\sum_{i=1}^{n} T_{\mathrm{x},i} \tag{2.1}$$

where $T_{\mathrm{x},i}$ are the i individual temperature sensors in the n-temperature sensor grid at location x. Air flow is said to be well-mixed when it has a uniform temperature and humidity at a cross-section. With this in mind, Equation (2.1) is valid for either uniform velocity or uniform temperature (well-mixed) conditions. If all temperature sensors in the grid have equal uncertainty, σ_T, then the systematic uncertainty of $T_{\mathrm{x,ave}}$ can be calculated using Equation (2.2),

$$\sigma_{T_{\mathrm{x,ave}}} = \frac{\sigma_T\sqrt{n}}{n}. \tag{2.2}$$

Thus, using the average temperature measurement from the collection of temperature sensors installed in a grid reduces the uncertainty of an individual sensor by $\sqrt{n}/n$ when the air flow is well mixed or has uniform mass flux. The individual and combined uncertainties of each of the thermocouple measurement grids are shown in Table 2.1. Note that in Chapter 3, it will be shown that the temperature at the mixed-air location is stratified and the flow at each individual sensor location is dependent on the outdoor-air damper position.

Table 2.1.
Individual and combined uncertainties of the thermocouple grid air temperature measurements, under a well-mixed or uniform velocity conditions.

Location	n	σ_T [°C]	$\sigma_{T,\text{ave}}$ [°C]
Return-Air	9	0.5	0.17
Outdoor-Air	9	0.5	0.17
Mixed-Air	16	0.5	0.13
Supply-Air	9	0.5	0.17
Condenser Inlet Air	20	0.5	0.17
Condenser Outlet Air	9	0.5	0.11

Humidity Measurements

Three humidity measurements were observed at different locations of the RTU. The return-air dew point was measured using a General Eastern (model: 1111H) dew point hygrometer with a single stage chilled mirror probe. At this location, return-air flow was assumed to be well mixed and thus a single-point probe was used at this location. The rated accuracy for this dew-point measurement was $\pm 0.2\,^{\circ}$C.

The outdoor-air dew point was measured at the the same location as the outdoor-air temperature sensor grid shown by Figure 2.2. Air sampling tubes were arranged in an equally-spaced 2-by-3 grid at this location and were measured using a General Eastern dew point hygrometer (model: D-2) via an air sampling pump (model: SSM-1). The rated accuracy of this device was also $\pm 0.2\,^{\circ}$C.

In a similar manner to the outdoor-air dew point measurement, a supply-air dew point measurement was made using air sampling tubes in an equally-spaced 2-by-2 grid. This grid was arranged at the supply-air outlet of the RTU, following the electric heating coil. The dew point was measured using a General Easter dew-point hygrometer (model: D-2) via an

air sampling pump (model: SSM-1). The rated accuracy of this measurement was $\pm 0.2\,^{\circ}$C. A summary of the dew-point measurements is shown in Table 2.2.

Table 2.2.
Summary of the dew point measurements on the RTU. The abbreviation "*GE*" corresponds to "General Eastern".

Location	Grid	Accuracy [°C]	Hygrometer Model	Pump Model
Return-Air	1-by-1	0.2	*GE* 1111H	N/A
Outdoor-Air	2-by-3	0.2	*GE* D-2	*GE* SSM-1
Supply-Air	2-by-2	0.2	*GE* D-2	*GE* SSM-1

Because there were only three available dew point hygrometers, an approximation was used to estimate the humidity ratio at the mixed-air location. The approximation is given by Equation (2.3) and (2.4),

$$\omega_{\text{ma}} = \frac{T_{\text{ma,ave}} - T_{\text{ra,ave}}}{T_{\text{oa,ave}} - T_{\text{ra,ave}}} \left(\omega_{\text{oa}} - \omega_{\text{ra}}\right) + \omega_{\text{ra}} \tag{2.3}$$

$$\frac{h_{\text{ma}} - h_{\text{ra}}}{h_{\text{oa}} - h_{\text{ra}}} \approx \frac{T_{\text{ma}} - T_{\text{ra}}}{T_{\text{oa}} - T_{\text{ra}}} \approx \frac{\omega_{\text{ma}} - \omega_{\text{ra}}}{\omega_{\text{oa}} - \omega_{\text{ra}}} \tag{2.4}$$

which is valid for a air mixing process. Equation (2.3) is valid for any RTU mode of operation. A better approximation can be made using Equation (2.5) when the RTU operates in "Fan-Only Mode",

$$\omega_{\text{ma}} = \frac{T_{\text{sa,ave}} - T_{\text{ra,ave}}}{T_{\text{oa,ave}} - T_{\text{ra,ave}}} \left(\omega_{\text{oa}} - \omega_{\text{ra}}\right) + \omega_{\text{ra}}. \tag{2.5}$$

This estimation is more accurate because the supply-air flow at the measurement location is mixed more effectively than the mixed-air flow. Thus, Equation (2.6) is a better approximation there is no active heating or cooling,

$$\frac{h_{\text{sa}} - h_{\text{ra}}}{h_{\text{oa}} - h_{\text{ra}}} \approx \frac{T_{\text{sa}} - T_{\text{ra}}}{T_{\text{oa}} - T_{\text{ra}}} \approx \frac{\omega_{\text{sa}} - \omega_{\text{ra}}}{\omega_{\text{oa}} - \omega_{\text{ra}}}. \tag{2.6}$$

In addition to the dew point measurements, relative humidity measurements of the outdoor room and indoor room were measured. These humidities corresponded to the outdoor ambient and indoor ambient relative humidity of the RTU, respectively. The relative humidity sensors used for these measurements had a rated accuracy of $\pm 2\,\%$. Because the dew point sensors were more accurate, these measurements were not used in the remaining analysis.

Air-Flow Measurements

An ASME standard nozzle was used to measure volumetric and mass air flow rates supplied by the RTU indoor fan. The RTU indoor fan frequency was controlled manually to produce different air flow rates for some tests. In order to obtain accurate air flow measurements, the nozzle combinations were chosen so that the acceptable measurement range matched the target air-flow rate. A Setra (model: M267MR3) pressure transducer was used to measure the nozzle pressure drop with a rated accuracy of $\pm 6.23\,$Pa ($\pm 1\,\%$ FS). This transducer was calibrated prior to testing using a micrometer U-tube manometer. A T-type thermocouple was used to measure the temperature of the air at the nozzle inlet with a rated accuracy of $\pm 1.0\,^{\circ}$C. In order to calculate the density of air at the inlet, the supply-air temperature dew point was used along with the dry-bulb temperature. To make up for the nozzle box pressure drop, a booster fan was controlled downstream of the measurement station to maintain a constant pressure drop across the RTU. The layout of the air flow measurement is shown in Figure 2.1.

Described in Chapter 3, a virtual supply-air flow sensor was developed. The sensor utilizes the differential pressure measurement between the indoor fan air inlet and outlet. This measurement was made using a Setra differential pressure transducer (model: M260). The rated accuracy of the pressure transducer was $\pm 2.491\,$Pa ($\pm 1\,\%$ FS). The pressure transducer was calibrated before testing using a micrometer U-tube manometer in order to improve this accuracy.

Another measurement used for the virtual air-flow sensor is a measurement of the indoor fan speed. An optical tachometer was built in order to measure the indoor fan shaft speed directly. Due to inconsistencies in this measurement, the indoor fan speed was measured directly from the output of the variable frequency drive controlling the fan instead. This output frequency had an accuracy of 0.05 Hz. A schematic of the measurements taken to characterize the indoor fan mass flow rate is shown in Figure 2.6.

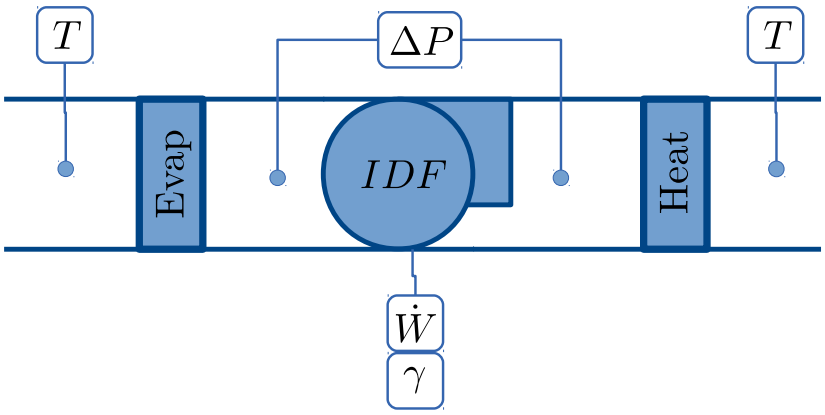

Figure 2.6. Instrumentation schematic for indoor fan measurements. Not pictured is a nozzle box air flow measurement station located downstream of the RTU.

Power Measurements

There were four power measurements taken on the RTU during its testing: the indoor fan, outdoor fan, compressor, and total power. The indoor fan power was measured using a power transducer made by Ametek Power Instruments (model: PCE-20) with a rated accuracy of ± 6.0 W (± 0.25 % FS). The condenser fan power was measured using a power transducer made by Ametek Power Instruments (model: PCE-15) with a rated accuracy of ± 4.5 W (± 0.25 % FS). The compressor power was measured using a Scientific Columbus (model: XL311K542-2-RS) with a rated accuracy of ± 2 W (± 0.2 % FS). The total power of the

RTU was measured using an Exceltronic power transducer (model: XL31K5A4-2-7-SC-RS) with a rated accuracy of ± 2 W (± 0.2 % FS).

Refrigerant Temperature Measurements

Several T-type immersion thermocouples were installed around the refrigerant circuit of the RTU in order to measure different temperatures. A schematic detailing the relative positions of these temperature measurements are shown in Figure 2.7. The temperatures measured are as follows: compressor suction, compressor discharge, condenser outlet, expansion valve inlet, and the evaporator inlet. Some temperature sensors are not shown in Figure 2.7; each evaporator circuit inlet and outlet temperature, and the temperature at the refrigerant mass flow meter. The rated accuracy of the immersion thermocouples were ± 1.0 °C.

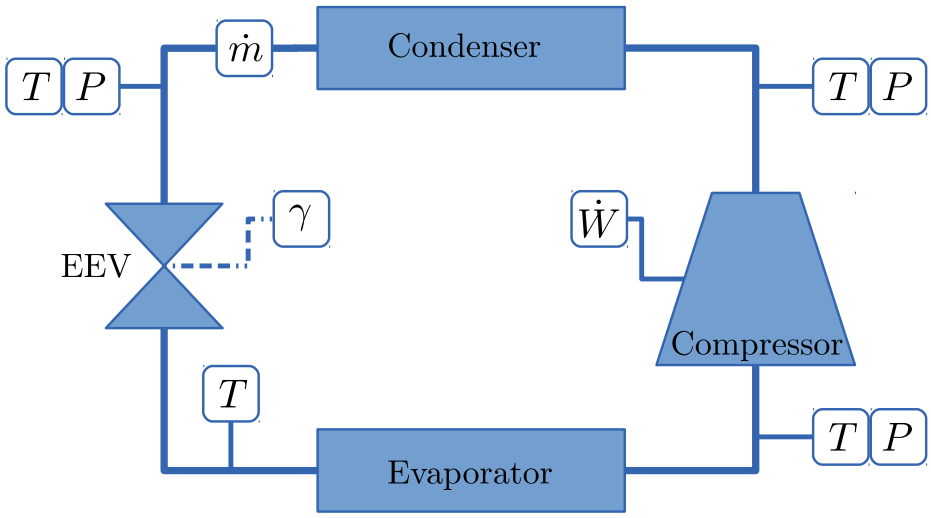

Figure 2.7. RTU vapor-compression cycle schematic detailing measurements recorded in order to analyze damper faults impact on cooling performance.

Refrigerant Pressure Measurements

The refrigerant compressor suction, compressor discharge, and evaporator inlet pressure were measured, shown in Figure 2.7. The pressure transducers used were made by Setra (model: M207). The rated accuracy of the pressure transducers were $\pm 0.13\,\%$. The pressure transducers were calibrated using a Setra sensor calibration device prior to testing.

Refrigerant Mass Flow Measurement

The mass flow rate of refrigerant was measured using a Micro Motion (model: DH-25) Coriolis mass flow meter with a rated of accuracy of $\pm 0.2\,\%$. The mass flow meter was installed between the condenser outlet and expansion valve inlet on the refrigerant circuit. Because the refrigerant lines had to be extended at this location, the system was charged according to manufacturer test data by matching the subcooling under the same operating mode and ambient conditions.

Data Acquisition System

For data collection and monitoring, an Agilent Technologies multifunction switch/measure unit (model: 34980A) and a Hewlett Packard mainframe (model: HP75000 Series B) were used in combination with LabView monitoring software.

2.2.3 Damper Operation and Control

In order to collect data that includes all modes of economizer operation, the economizer controller was disconnected and the outdoor-air damper was controlled manually. The actuator was controlled using a $2\,\mathrm{V}$ to $10\,\mathrm{V}$ control signal, operated through the data acquisition system user interface. A $2\,\mathrm{V}$ signal corresponds to the fully-closed damper position; a $10\,\mathrm{V}$ corresponds to the fully-open damper position. Intermediate control signals could be commanded in order modulate the outdoor-air damper the full-range of damper positions.

2.3 Description of Experiments

2.3.1 Damper Performance Tests

In order to characterize the outdoor-air damper behavior, several tests were conducted with the RTU in "Fan-Only" mode. Active heating or cooling was not used for these tests in order to observe the ventilation performance of the unit, as well as assess the mixing characteristics of the air streams at different locations within the RTU. A range of ambient outdoor temperatures were controlled while maintaining a constant ambient indoor temperature in order to observe mixing characteristics at different conditions. These combinations are listed in Table 2.3, along with the controlled damper position.

Table 2.3.
Summary of outdoor-air damper test conditions along with the different damper positions controlled during the tests.

Outdoor Temp. [°C]	Indoor Temp. [°C]	Damper Positions [%]
6.11	26.11	0, 10, 20, 30, 40, 50, 60, 70, 80, 90, 100
12.57	25.56	0, 10, 20, 30, 40, 50, 60, 70, 80, 90, 100
15.56	26.67	0, 5, 10, 15, 20, 25, 30, 35, 40, 45, 50, 55, 60, 65, 70, 75, 80, 85, 90, 95, 100
18.33	25.56	0, 20, 40, 60, 80, 100
29.44	25.56	0, 20, 40, 60, 80, 100
35.00	25.56	0, 10, 20, 30, 40, 50, 60, 70, 80, 90, 100

In order to measure the outdoor-air fraction during the tests, the following method based on the mass and energy balance of the mixing box was used:

$$\text{OAF} = \frac{T_{\text{sa,ave}} - T_{\text{ra,ave}}}{T_{\text{oa,ave}} - T_{\text{ra,ave}}}.$$

The average supply-air temperature was used in this calculation instead of the mixed-air temperature because it was more accurate. The accuracy of the mixed-air temperature sensor is reduced due to temperature stratification and non-uniform mass flux across the measurement grid. A summary of the results of outdoor-air fractions determined from measurements for different tests is shown by Figure 2.8.

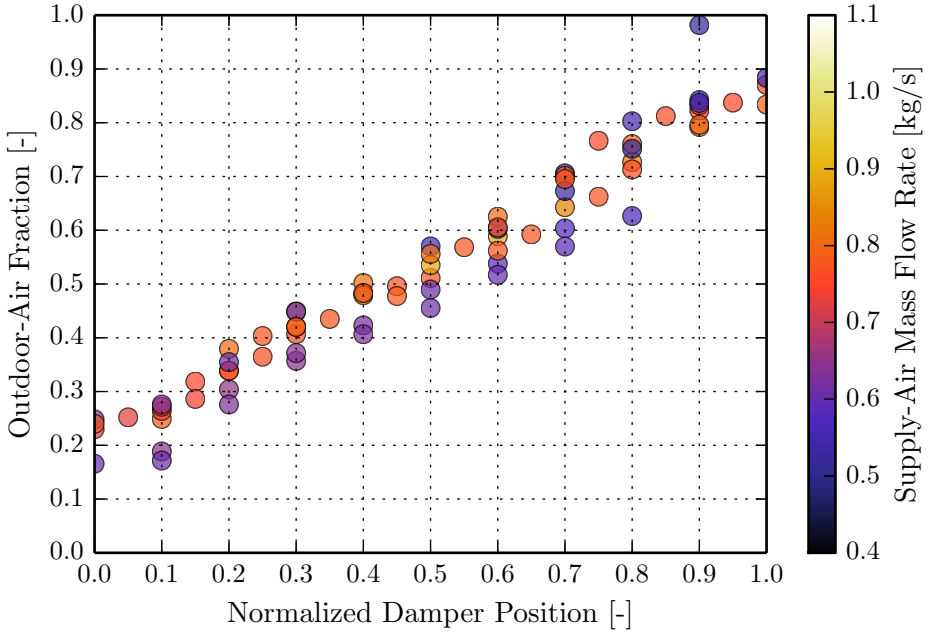

Figure 2.8. Measured outdoor-air fraction for different controlled damper positions and mass air flow rates.

2.3.2 Indoor Fan Performance Tests

A set of fan performance tests were conducted in order to characterize the performance of the indoor fan. In order to eliminate errors caused by temperature stratification on measurements, the tests were performed with the same outdoor and indoor ambient conditions. This was important because one of the characteristics studied was the indoor fan temperature rise. Furthermore, temperature stratification was noticed at the mixed-air location along with non-uniform air flow rates leading to error. The measured indoor fan volumetric flow rate is mapped as a function of the differential pressure across the fan and the normalized control frequency in Figure 2.9.

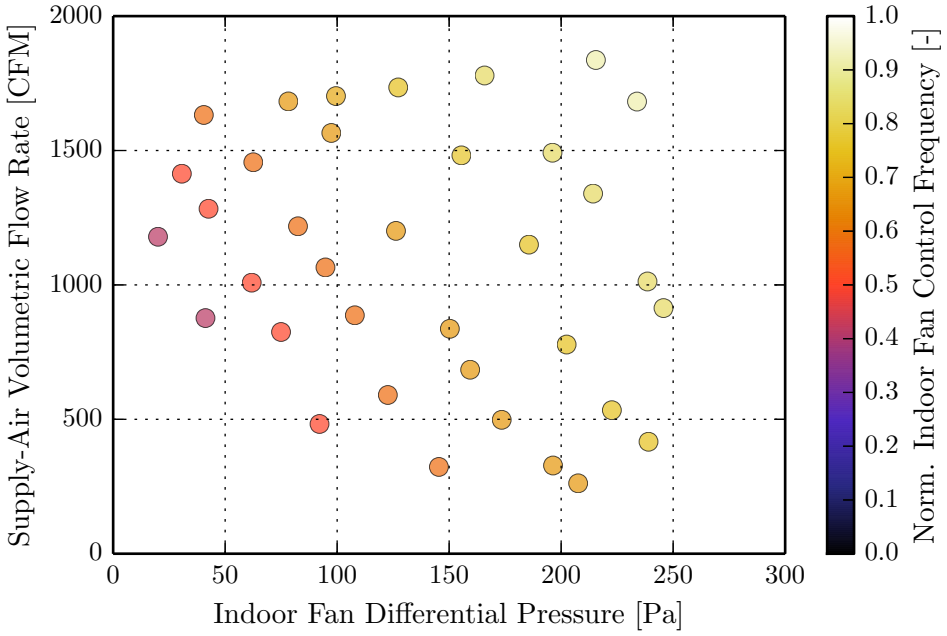

Figure 2.9. Volumetric flow rate supplied by the indoor fan under different differential pressure and speed combinations.

2.3.3 Damper Fault Impact Tests

The impact of incorrect damper position on cycle performance was studied using the RTU described previously. Several temperature and pressure sensors were installed on the refrigerant cycle in order to characterize the performance of the different components. The refrigerant-side instrumentation schematic is shown in Figure 2.7. The suction and discharge conditions were determined using temperature and pressure sensors at the compressor inlet and outlet respectively.

The refrigerant mass flow rate was controlled using an electronic expansion valve (EEV). The EEV opening was controlled manually in order to maintain a constant superheat at the compressor inlet, calculated using the difference between the suction temperature and evaporator inlet temperature.

A summary of the test conditions used to investigate damper fault impacts on RTU performance is shown in Table 2.4. In order to observe impacts on both sensible and latent loads on performance, varying degrees of outdoor-air temperature and humidity were used with constant return-air conditions.

Table 2.4.
Damper fault impact test conditions for the outdoor and indoor environments as well as the damper positions controlled.

T_{oa} [°C]	ϕ_{oa} [%]	T_{ra} [°C]	ϕ_{ra} [%]	γ_{oad} [-]
31.50	40	26.00	50	20, 40, 60, 80
31.50	50	26.00	50	10, 30, 50, 70
37.78	50	26.00	50	0, 33, 50, 67, 100

Figures 2.10, 2.11, and 2.12 show a comparison of RTU capacity and efficiency as functions of outdoor-air damper position under different outdoor-air conditions. In each of the cases, the capacity, $\dot{Q}_{\text{evap}}$, was calculated using Equation (2.7),

$$\dot{Q}_{\text{evap}} = \dot{m}_{\text{ref}} \left(h_{\text{suc}} - h_{\text{eri}} \right) \tag{2.7}$$

where $\dot{m}_{\text{ref}}$ is the measured refrigerant mass flow rate, h_{suc} is the refrigerant enthalpy at the compressor suction, h_{eri} is the refrigerant enthalpy at the evaporator inlet. In order to calculate h_{eri}, an isenthalpic expansion valve was assumed. The RTU cycle efficiency, COP, was calculated using Equation (2.8),

$$\text{COP} = \frac{\dot{Q}_{\text{evap}}}{\dot{W}_{\text{comp}}} \tag{2.8}$$

where $\dot{W}_{\text{comp}}$ is the measured compressor power. A more detailed analysis of the impact on performance of outdoor-air damper faults is discussed in Chapter 5, including discussion of ventilation load, sensible heat ratio, and run-time impacts.

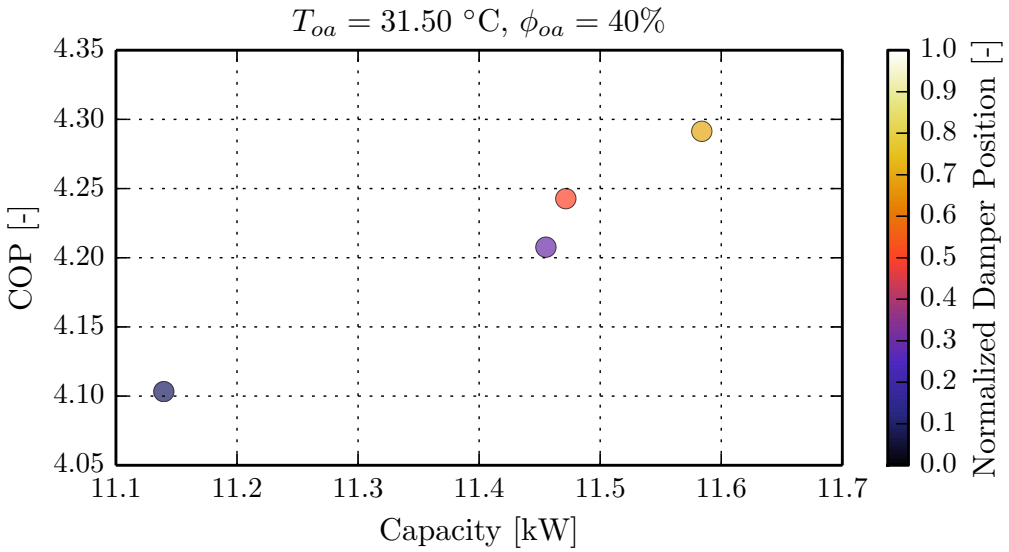

Figure 2.10. Effect of damper position on RTU capacity and COP under 31.50 °C, 40% outdoor-air temperature and relative humidity, while maintaining 26.00 °C, 50% return-air temperature and relative humidity.

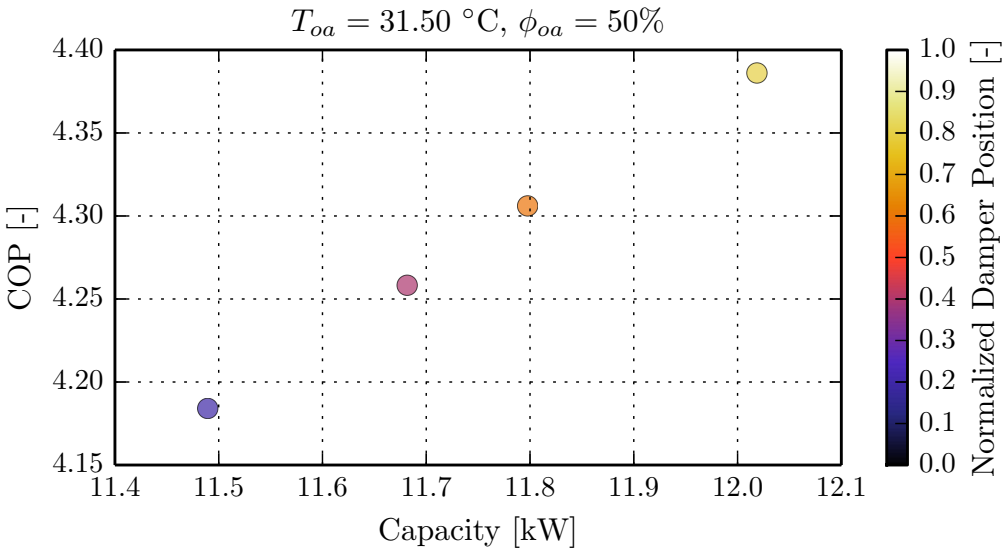

Figure 2.11. Effect of damper position on RTU capacity and COP under 31.50 °C, 50% outdoor-air temperature and relative humidity, while maintaining 26.00 °C, 50% return-air temperature and relative humidity.

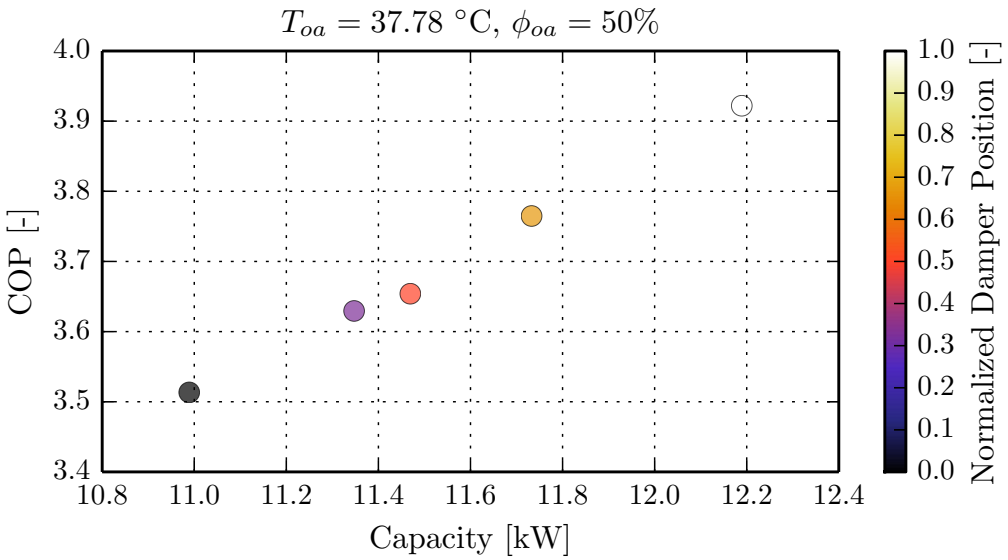

Figure 2.12. Effect of damper position on RTU capacity and COP under 37.78 °C, 50% outdoor-air temperature and relative humidity, while maintaining 26.00 °C, 50% return-air temperature and relative humidity.

3. MODELING AND SENSOR CORRECTIONS

Physical models and sensor corrections were developed in order to predict normal economizer performance as well as provide accurate inputs into the FDD algorithms. The models were trained and validated using experimentally collected data from the 4-ton RTU described in Chapter 2. Two sensor correction models were designed in order to improve the accuracy of the outdoor-air and mixed-air temperature sensors. A model for predicting the expected outdoor-air fraction as a function of outdoor-air damper position was also designed. Finally, a virtual indoor fan sensor was developed to provide estimations of supply-air mass flow rate and indoor fan power.

3.1 Return-Air Recirculation and Outdoor-Air Temperature Correction

On the RTU, the outdoor-air and return-air streams are controlled by the outdoor-air damper. This damper is located within the economizer hood and is controlled by the economizer controller. This provides enables modulation of the outdoor-air in order to meet indoor-air quality requirements and to reduce the mechanical cooling requirement when ambient conditions are favorable. A cross-section of the economizer hood assembly is pictured in Figure 3.1 when the damper is in the closed position. At this position, mostly return-air is supplied to the mixing box where it enters the evaporator coil. One scenario when the outdoor-air damper is controlled to this position is when the outdoor-air is warmer than the return-air. Ideally, zero outdoor-air enters the mixing box when the damper is fully-closed in order to reduce the ventilation load. Most outdoor-air dampers on RTUs are not ideal however, and significant outdoor-air can enter the mixing box.

Figure 3.2 shows the economizer hood cross-section when the damper is controlled 100% open. At this position, mostly outdoor-air is supplied to the conditioned space, though significant return-air leakage can be present in real dampers. To avoid over-pressurizing the

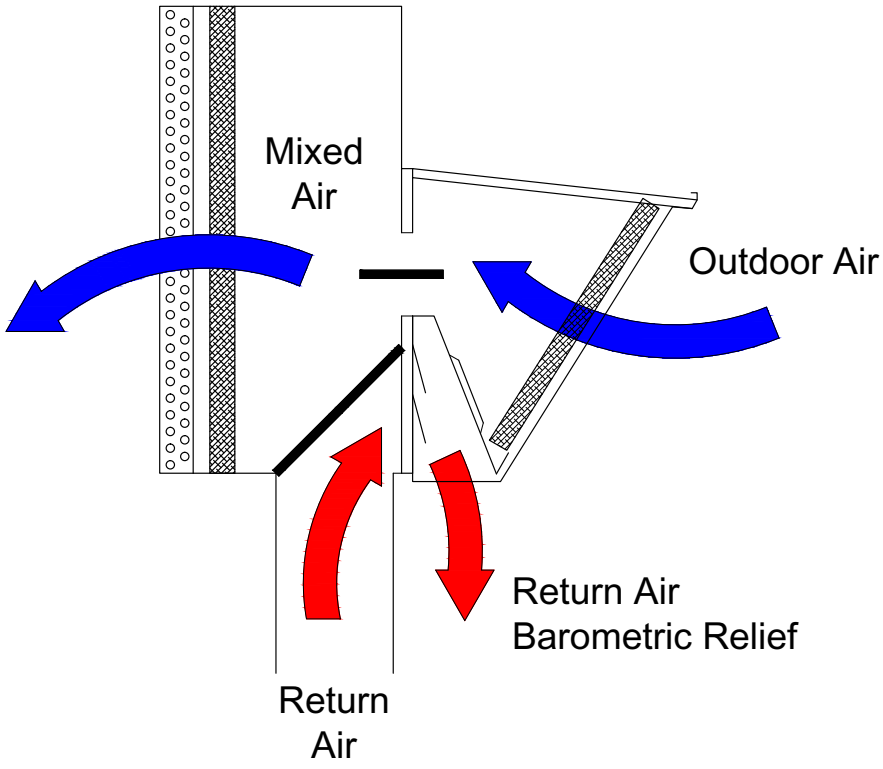

Figure 3.1. Cross-section of the economizer hood when the outdoor-air damper is in the closed position. In this position, mostly return-air is supplied to the conditioned space.

building, a barometric relief vent opens to exhaust the return-air. The damper is commanded fully-opened by the economizer controller when the outdoor-air conditions become favorable. Depending on the economizer control algorithm, this may be based on the outdoor-air dry-bulb temperature or enthalpy compared to a set point (known as a high-limit strategy) or based on a difference between outdoor-air and return-air dry-bulb temperatures or enthalpy (known as a differential strategy). More detailed or complex strategies can also be used to control the outdoor-air damper. Taylor and Cheng give a detailed description of many of these strategies and a comparison of their shortcomings [21].

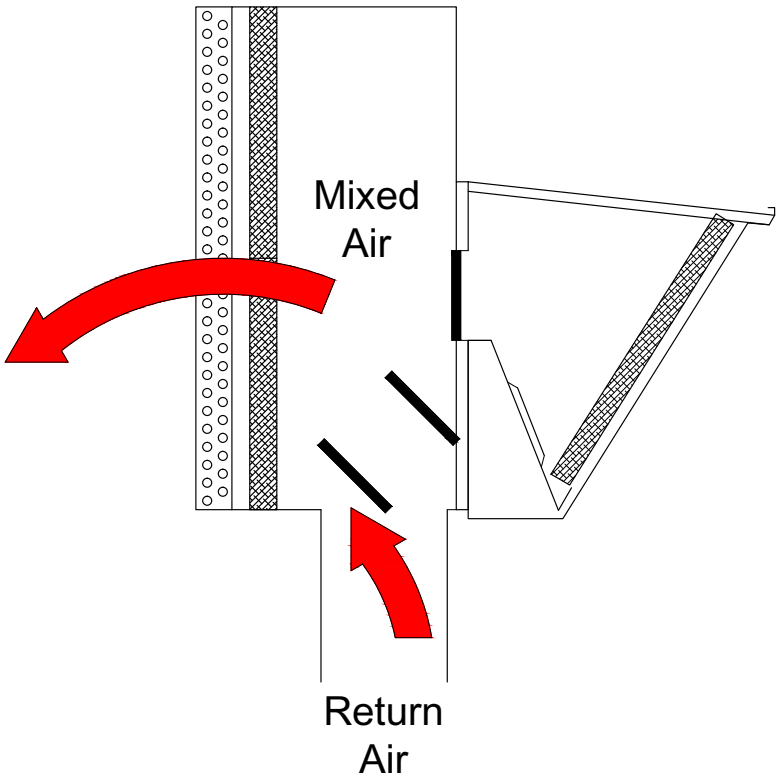

Figure 3.2. Cross-section of the economizer hood when the outdoor-air damper is in the fully-open position. In this position, mostly outdoor-air is supplied to the conditioned space. Return-air is exhausted through barometric relief vents to maintain building pressure.

During testing of the RTU at different outdoor-air conditions and damper positions, a dependence of outdoor-air temperature, T_{oa}, on the damper position was noticed. This is counter-intuitive since the outdoor-air damper is downstream of the outdoor-air temperature measurement location. After investigation, it was realized that a portion of the return-air stream exhausted from the RTU was being recirculated back into the unit due to the economizer hood design. This phenomena is illustrated in Figure 3.3. In order to confirm this behavior, the single-point outdoor-air temperature sensors were examined at different damper positions. Evidence of this return-air recirculation is shown in Figure 3.4. As the damper opens, the temperature measurements nearest to the barometric relief ventilation deviated from the other temperature measurements as the damper opened.

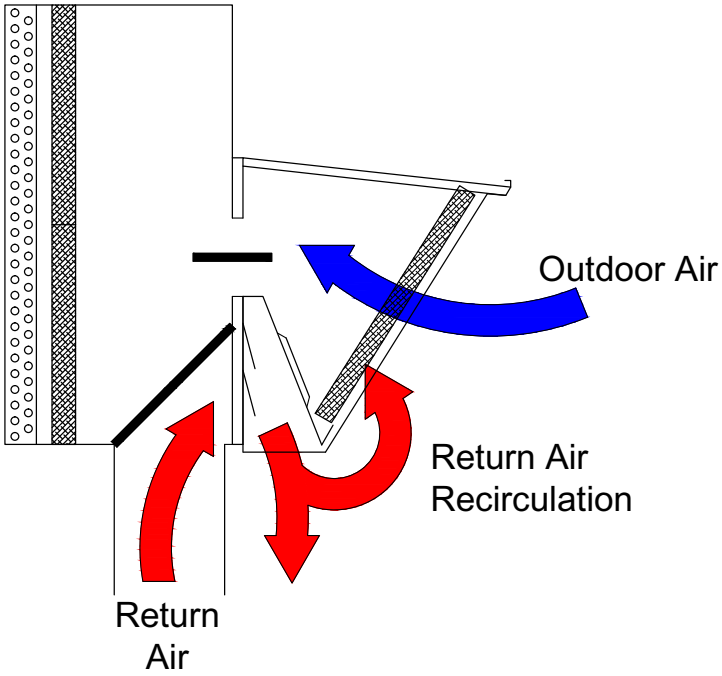

Figure 3.3. The design of the outdoor-air intake hood allows a portion of the exhausted return-air to recirculate back into the RTU with the outdoor-air.

Because the temperature is not uniform across the outdoor-air intake, significant deviation between the bulk outdoor-air temperature and a single-point outdoor-air temperature

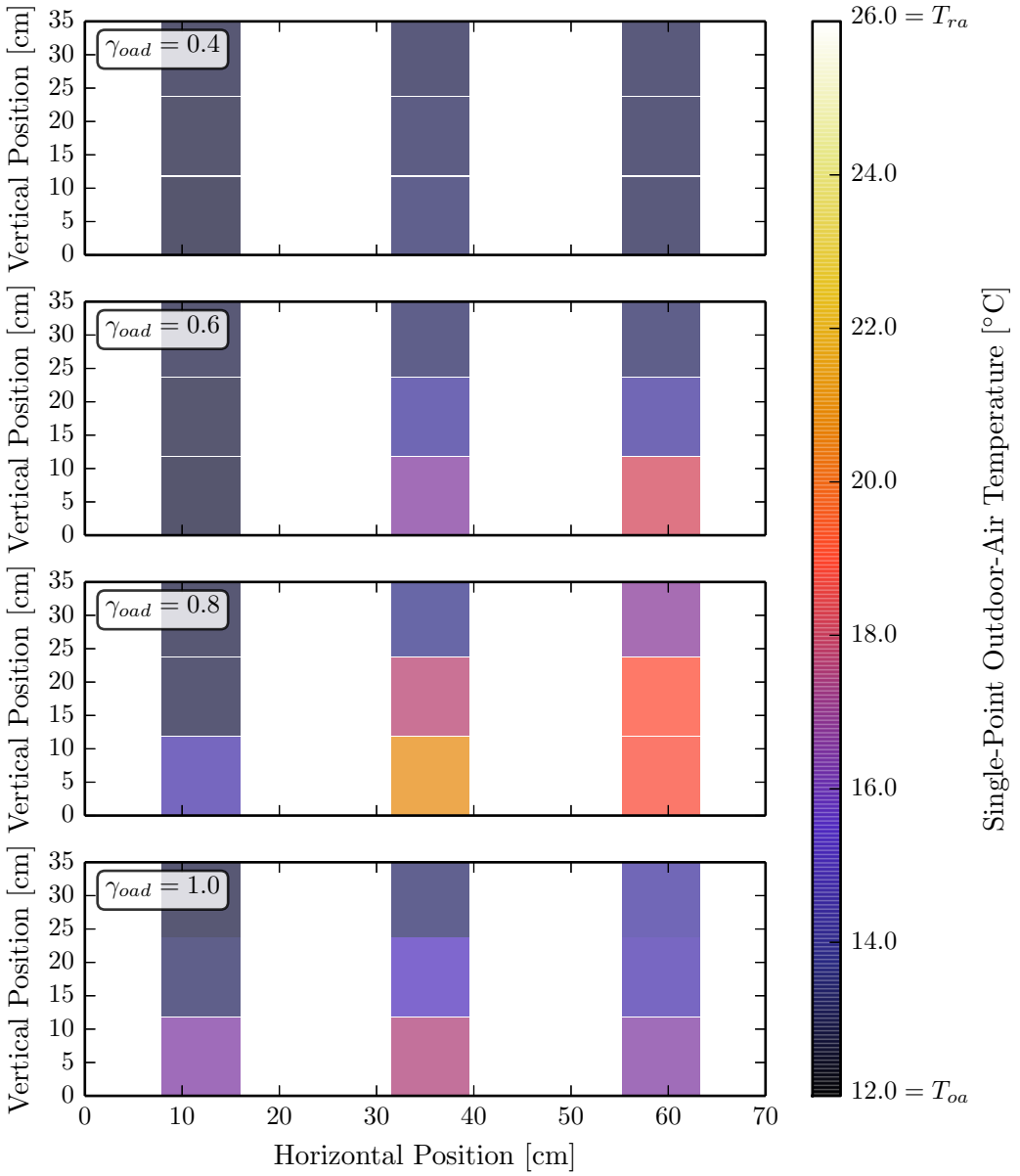

Figure 3.4. Single-point outdoor-air temperature measurements at different outdoor-air damper positions. As the outdoor-air damper opens, warmer return-air is recirculated back into the RTU with the outdoor-air stream. Evidence of this can be seen near the bottom of the outdoor-air intake since those temperatures tend to increase most with changing damper position.

measurement is possible. These errors can lead to improper economizer control by monitoring an incorrect outdoor-air temperature. Incorrect outdoor-air temperatures would also lead to inconsistent fault detection and diagnosis performance. In order to ensure that a single-point outdoor-air temperature measurement provides an accurate estimate of the bulk outdoor-air temperature entering the RTU mixing box, a correction model was created. The model, given by Equation (3.1), accounts for the difference in temperature of the outdoor-air and return-air streams as well as the normalized outdoor-air damper control signal, γ_{oad}:

$$T_{\text{oa,corr}} = c_0 + c_1 T_{\text{oa}} + c_2 \left(T_{\text{oa}} - T_{\text{ra}}\right) \gamma_{\text{oad}}. \tag{3.1}$$

Figure 3.5 shows the single-point T_{oa} taken at the middle of the outdoor-air intake as a function of the bulk outdoor-air temperature, $T_{\text{oa,ave}}$. It is clear that as the damper opens, the bulk outdoor-air temperature becomes closer to the return-air temperature due to recirculation. However, the single-point outdoor-air temperature measurement is influenced less by the damper position since it stays relatively constant over the range of damper positions.

The root-mean-square error, RMSE, as well as the maximum absolute deviation, MAD, between each single point outdoor-air temperature measurement and the average of the measurement grid are calculated in Table 3.1. Also calculated are the RMSE and MAD of the single-point sensors after the correction model in Equation (3.1) was applied. From the information shown in Table 3.1, a outdoor-air temperature sensor location can be made in order to minimize the error. The sensor location with the smallest RMSE, "Sensor 6", is compared with $T_{\text{oa,ave}}$ in Figure 3.6. This shows that with correction, the single-point sensor is able to give a more accurate measurement in the presence of temperature stratification caused by return-air recirculation.

3.2 Thermal Mixing Performance in RTU Mixing Box

Many FDD methods for air conditioning equipment rely on a mixed-air temperature measurement (T_{ma}). This measurement is important because it can be used to estimate the outdoor-air fraction supplied by the economizer. The outdoor-air fraction (or sometimes called fresh-air fraction) estimate is a very good indicator of economizer performance

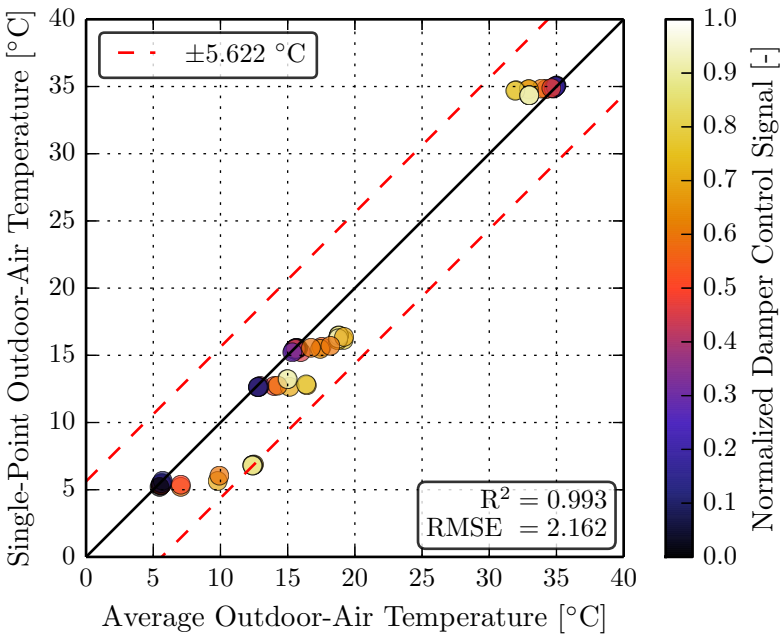

Figure 3.5. Measured single-point outdoor-air temperature, T_{oa}, as a function of averaged outdoor-air temperature, $T_{\text{oa,ave}}$. It is clear that as the damper opens, the single-point measurement deviates from the bulk temperature.

Table 3.1.
Root-mean-square error, RMSE, and maximum absolute devation, MAD, between the single-point outdoor-air temperature measurements and average outdoor-air temperature, before and after applying the correction model.

	Before Correction		After Correction	
Sensor	RMSE [°C]	MAD [°C]	RMSE [°C]	MAD [°C]
1	1.394	5.271	0.847	3.125
2	1.372	4.243	0.865	2.522
3	2.507	6.932	0.921	2.900
4	0.937	2.781	0.840	2.563
5	1.224	4.708	1.066	3.759
6	2.162	5.622	0.789	2.220
7	3.156	8.905	2.307	6.500
8	3.378	9.269	2.415	6.351
9	0.912	2.288	0.858	1.880

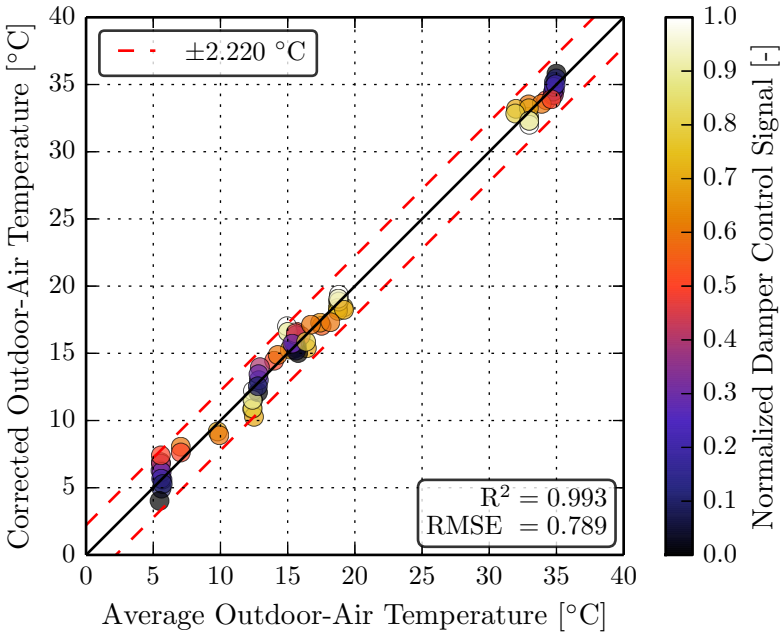

Figure 3.6. Corrected outdoor-air temperature, $T_{\text{oa,corr}}$, as a function of average outdoor-air temperature, $T_{\text{oa,ave}}$. By accounting for the damper position and temperature difference between outdoor-air and return-air streams, the measurement error is reduced.

because it is a surrogate measurement for outdoor-air damper position. Additionally, the mixed-air temperature is equivalent to the evaporator-air inlet temperature in packaged air conditioners. Existing FDD methods such as the SRB method [22] or the decoupling-based method [6] require T_{ma} in order to detect refrigerant-side faults in the system. The mixed-air temperature is also used in many FDD tools for air-side economizers [12, 13].

In order to determine outdoor-air fraction, direct measurements of the outdoor- and supply-air flow rates can be made. A hot-wire anemometer is a typical device used for this purpose where air-velocity is measurement and a volumetric flow-rate is calculated based on duct geometry. This quantity can then be used to calculate the mass flow rate using standard air psychrometric properties. If these two measurements are made, the outdoor-air fraction (OAF) can be calculated using Equation (3.2),

$$\text{OAF} = \frac{\dot{m}_{\text{oa}}}{\dot{m}_{\text{sa}}}. \tag{3.2}$$

where $\dot{m}_{\text{oa}}$ and $\dot{m}_{\text{sa}}$ are the outdoor-air and supply-air mass flow rates, respectively. Due to the relatively high cost of directly measuring flow rates compared to the cost of a packaged air conditioner, direct measurements of outdoor-air and supply-air flow rate are rarely installed in the field. Accurate and reliable measurements from these types of devices also require specific duct layouts that may not be available in some buildings. Because of this, most FDD applications use alternative measurements to determine outdoor-air fraction.

More commonly, the method used to determine the outdoor-air fraction relies on a set of three air-temperature measurements easily available in all packaged air conditioners. The three temperatures used in this method, described by Friedman and Piette [23], are outdoor-, return-, and mixed-air temperatures:

$$\text{OAF} = \frac{T_{\text{ma}} - T_{\text{ra}}}{T_{\text{oa}} - T_{\text{ra}}}. \tag{3.3}$$

Accurate temperature measurements are important when using Equation (3.3), as errors can lead to large deviations between the measured and actual OAF. Obtaining accurate measurements, especially the mixed-air temperature, can be difficult since T_{ma} is prone to inaccuracy due to stratification caused by poor mixing performance.

In order to quantify the mixing performance, the modified range mixing effectiveness (E_{RdT}) defined by Robinson was used, Equation (3.4):

$$E_{RdT} = \left(1 - \frac{T_{\max} - T_{\min}}{|T_{\text{oa}} - T_{\text{ra}}|}\right) \times 100\% \tag{3.4}$$

where $T_{\max}$ and $T_{\min}$ are the maximum and minimum measured T_{ma} from the mixed-air measurement grid. The modified range mixing effectiveness ranges from $0\,\%$ to $100\,\%$ where $100\,\%$ represents perfect mixing. Using averaged air temperature measurements and Equation (3.3), the modified range mixing effectiveness was calculated for all economizer test points and the results of these calculations are plotted as a function OAF in Figure 3.7. At its worst, the E_{RdT} was nearly zero when the OAF was around $60\,\%$ indicating very poor

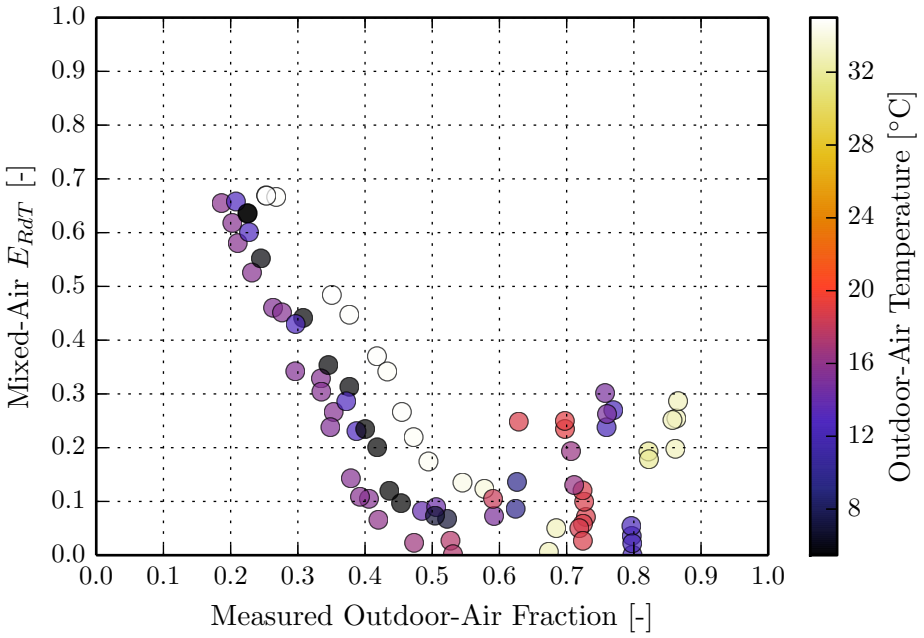

Figure 3.7. The mixed-air modified range mixing effectiveness as a function of outdoor-air fraction. Imperfect mixing is observed for the entire range of OAF tested.

mixing. The poor mixing performance observed in the mixing box of the RTU is due to its small size and geometry of the outdoor- and return-air inlets. The relative low air velocities entering contributes to imperfect mixing, as well as the lack of static mixing devices.

Because of the small footprint desired for packaged air conditioners, space dedicated for a mixing box is limited, so enlarging this can be impossible. It is also recommended that the air intakes be symmetrical in order to achieve greater mixing effectiveness [24], which is not always possible either.

Poor mixing performance introduces stratification within the RTU mixing box. Stratification can lead to severe problems such as coil freeze-ups but also to nuisances like freezestats frequently being tripped. From an economizer FDD perspective, temperature variations at the mixed-air temperature location, can lead poor fault detection and diagnostics performance. If normal sensor inaccuracy exists, fault detection sensitivity is decreased due to less confidence in normal behavior. False alarm rate can also be affected due to less robust OAF calculations.

3.3 Improving Mixed-Air Temperature Measurement Accuracy

Due to its importance for economizer FDD and the poor mixing performance within the RTU mixing box, the accuracy of the mixed-air temperature measurement has been studied. One method to improve the accuracy of T_{ma} is to use an average of multiple sensors instead of using a sensor at a single point in the mixing box. However, Wichman found that a more effective method is to develop correlations to correct the T_{ma} using measurements of T_{oa} and T_{ra} as well as the damper control signal γ_{oad} [18]. This method has the additional advantage of requiring less sensors, reducing instrumentation complexity and cost.

Due to poor mixing characteristics, a significant mixed-air temperature error $T_{\text{ma,error}}$ exists. In order to characterize this bias, a corrected supply-air temperature $T_{\text{sa,adj}}$ can be used when the cooling and heating coils are turned off. When there is no active heating or cooling, the supply-air sensor can be used as a surrogate for mixed-air temperature because the air stream is more thoroughly mixed after flowing through the evaporator coil and indoor fan. The effectiveness of this mixing process is shown in Figure 3.8. However, T_{sa} is not exactly T_{ma} due to heat gained from the indoor fan. The temperature rise caused by the indoor fan must be corrected in order to achieve better accuracy.

3.3.1 Characterizing Temperature Rise across the Indoor Fan

When the heating and cooling coils are inactive, the temperature difference between the mixed-air and supply-air is caused by the indoor fan. This temperature difference, called the indoor fan temperature rise, ΔT_{idf}, can be calculated using Equation (3.5),

$$\Delta T_{\text{idf}} = T_{\text{sa}} - T_{\text{ma}}. \tag{3.5}$$

Equation (3.5) assumes that there is zero heat transfer between the air stream and the heating or cooling coil. Additionally, it assumes minimal heat transfer by infiltration gains or leakage losses.

Since the supply-air stream is considered to be well mixed, based on the modified range mixing effectiveness shown in Figure 3.8, the supply-air temperature adjusted for the

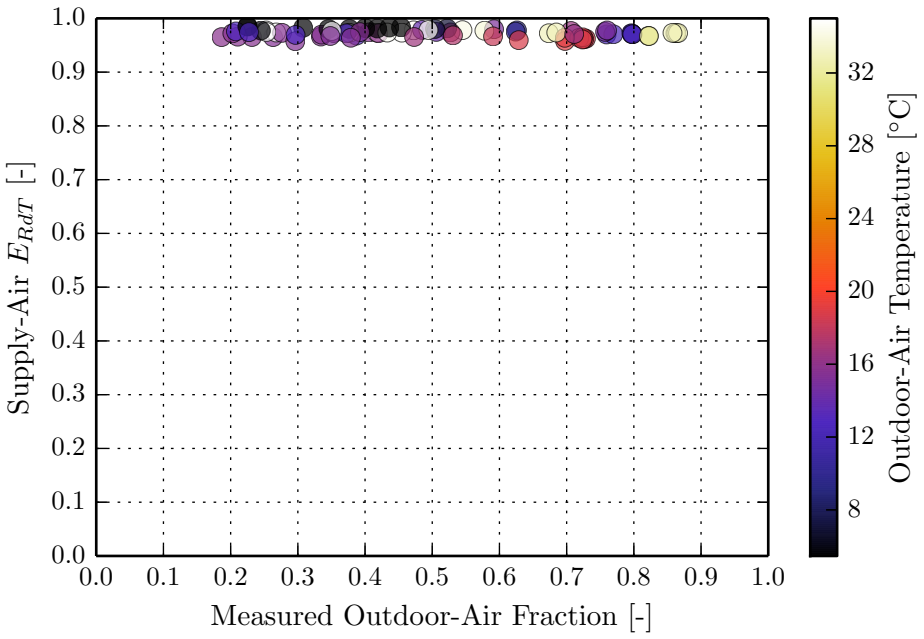

Figure 3.8. The supply-air modified range mixing effectiveness as a function of outdoor-air fraction. A significant improvement in mixing effectiveness is achieved when the air flows through the evaporator coil and indoor fan.

indoor-fan temperature rise, $T_{\text{sa,adj}}$, can be used as a surrogate for mixed-air temperature, T_{ma}, when the heating and cooling coils are inactive:

$$T_{\text{ma}} \approx T_{\text{sa,adj}} = T_{\text{sa}} - \Delta T_{\text{idf}}. \tag{3.6}$$

In addition, $T_{\text{sa,adj}}$ is a more accurate measurement of T_{ma} due to the poor mixing characteristics of the mixed-air stream. This is an especially important consideration when single-point temperature sensors are used to measure the different air temperatures.

In order to characterize ΔT_{idf}, T_{ma} and T_{sa} were measured when the outdoor and indoor conditions were equal while the RTU was in "Fan-Only Mode". This eliminates any thermal stratification in the mixing box and also minimizes any heat transfer due infiltration. Under these conditions, ΔT_{idf} was calculated using Equation (3.5).

An energy balance performed on the indoor fan control volume, enclosing the air inlet and outlet, yields an alternative form of ΔT_{idf} that illustrates other important system variables:

$$\Delta T_{\text{idf}} = \frac{\dot{W}_{\text{idf}}}{\dot{m}_{\text{sa}} C_p} \tag{3.7}$$

where $\dot{W}_{\text{idf}}$ is the indoor fan power, $\dot{m}_{\text{sa}}$ is the supply-air mass flow rate, and C_p is the specific heat of air at constant pressure. The efficiency of the fan has no impact on ΔT_{idf} in RTU applications because the fan and motor are in the flow stream so all the electrical power goes into the temperature rise. Equation (3.7) was used to calculate the indoor fan temperature rise using the measured supply-air mass flow rate and indoor fan power. This calculation was performed for each test case and the results are plotted against the measured indoor fan temperature rise calculated using Equation (3.5) in Figure 3.9.

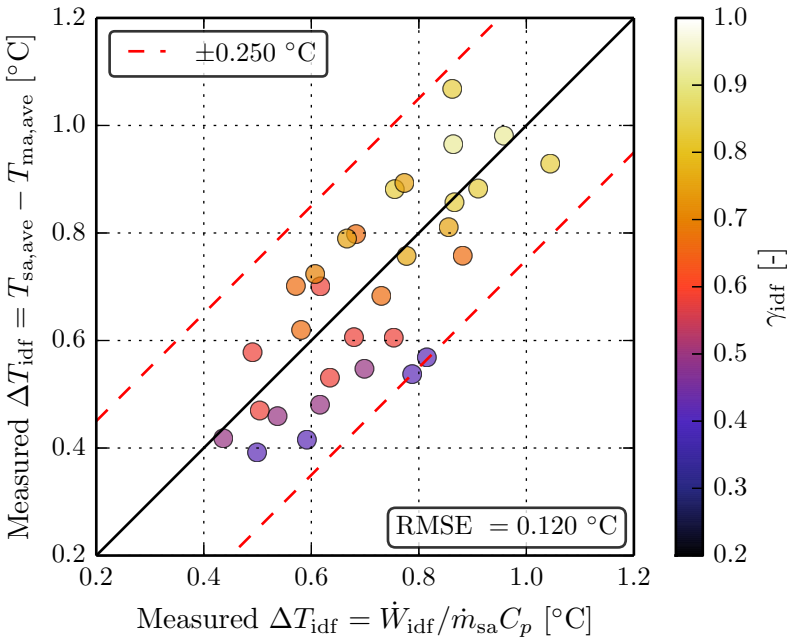

Figure 3.9. Comparison of the measured indoor fan temperature rise with the calculated indoor fan temperature rise using indoor fan power and supply-air mass flow rate measurements.

Air flow rate is an expensive measurement relative to the cost of an RTU. The same is true for direct power measurements. Because of this, alternative mass flow rate and power measurements are needed in order to apply (3.7) cost effectively. One alternative is to use virtual sensors to estimate these expensive quantities. A virtual sensor is a sensor based on low-cost measurements and a mathematical model used in place of difficult or expensive direct measurements. Derivations of virtual supply-air mass flow rate and virtual indoor fan power are provided in Sections 3.5.1 and 3.5.2, respectively.

Using the virtual sensors for supply-air mass flow rate and indoor fan power, Equation (3.7) was evaluated for each test case and is plotted against the measured temperature rise in Figure 3.10. A maximum error of $0.198\,°\text{C}$ resulted from the fit with an RMSE of $0.086\,°\text{C}$.

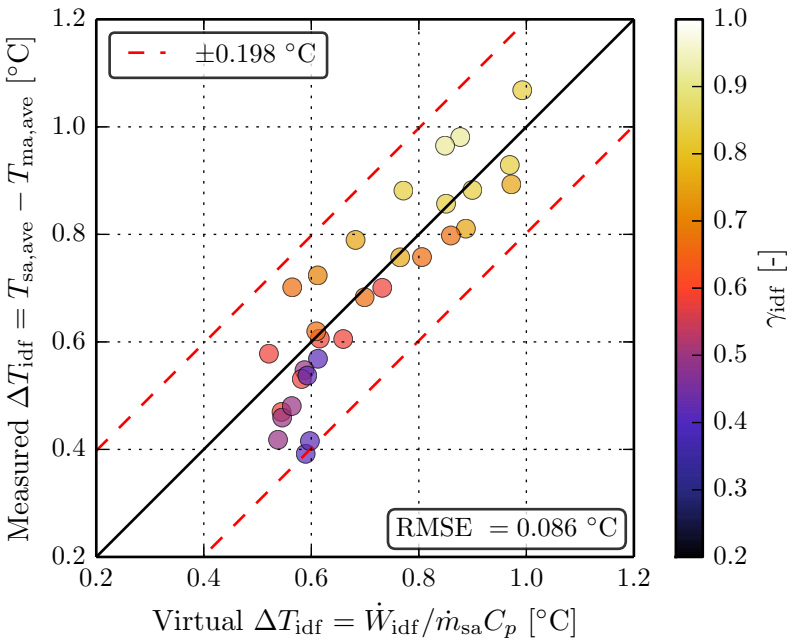

Figure 3.10. Comparison of the measured indoor fan temperature rise and the value calculated using Equation (3.7) evaluated using virtual sensor outputs.

The indoor fan temperature rise model was used to calculate $T_{\text{sa,adj}}$ when the RTU was running in "Fan-Only Mode". The 16-point mixed-air temperature grid average was plotted

as a function of $T_{\text{sa,adj}}$ and outdoor-air damper position, γ_{oad}, in Figure 3.11. The deviation between $T_{\text{sa,adj}}$ and $T_{\text{ma,ave}}$ illustrates that simply adding additional sensors at the evaporator air inlet does not necessarily eliminate the error caused by thermal stratification. This is because the simple average assumes uniform mass flux or velocity at each sensor location. The actual flow rate rates at each sensor location are nonuniform, especially near the corners of the mixing box.

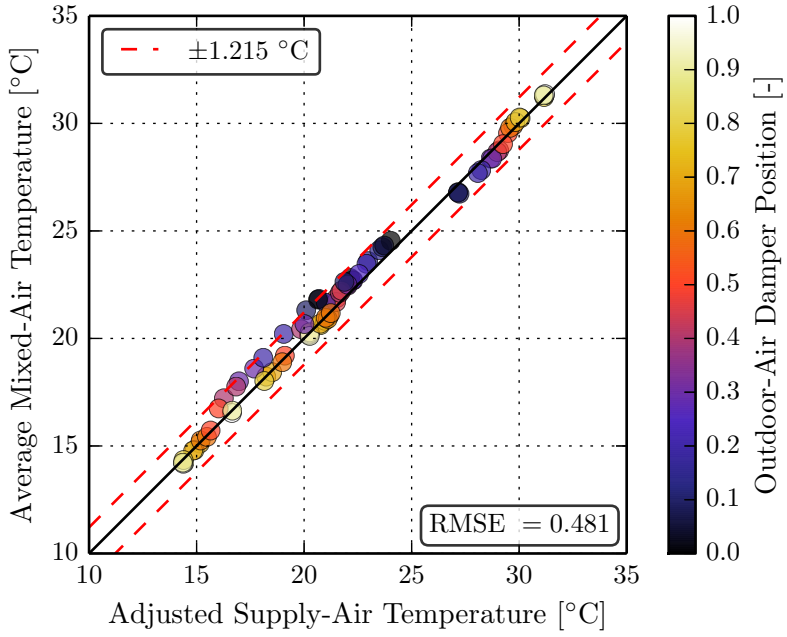

Figure 3.11. Comparison between the indoor fan temperature rise corrected supply-air temperature, $T_{\text{sa,adj}}$, and the 15-point average mixed-air temperature, $T_{\text{ma,ave}}$.

3.3.2 Effect of Poor Mixing on Mixed-Air Temperature Accuracy

The major effect that ineffective mixing has on T_{ma} is the deviation of a single-point mixed-air measurement from the bulk mixed-air temperature entering the evaporator coil. In

order to quantify this deviation, $T_{\text{ma,error}}$, the total error between a single-point temperature measurement and a robust mixed-air temperature measurement, $T_{\text{ma,rbst}}$,

$$T_{\text{ma,error}} = T_{\text{ma}} - T_{\text{ma,rbst}}. \tag{3.8}$$

In this case, $T_{\text{ma,rbst}}$ is equal to $T_{\text{sa,adj}}$. In order to characterize $T_{\text{ma,error}}$ dependence on damper position, a normalized damper control signal, γ_{oad} was used,

$$\gamma_{\text{oad}} = \frac{\psi_{oad} - 2\,\text{V}}{10\,\text{V} - 2\,\text{V}} \tag{3.9}$$

where ψ_{oad} is the $2\,\text{VDC}$ to $10\,\text{VDC}$ economizer control signal to the outdoor-air damper actuator ($2\,\text{V}$ represents the damper in the fully-closed position). A control signal was used to represent the outdoor-air damper position as opposed to an actual damper position sensor since it can be used in an embedded economizer FDD tool without additional sensors. Furthermore, this signal provides information about the desired damper position as determined by the controller that is not affected by a stuck damper fault.

The non-uniform temperature distribution at the evaporator inlet is shown for a range of outdoor-air damper positions in Figures 3.12 and 3.13.

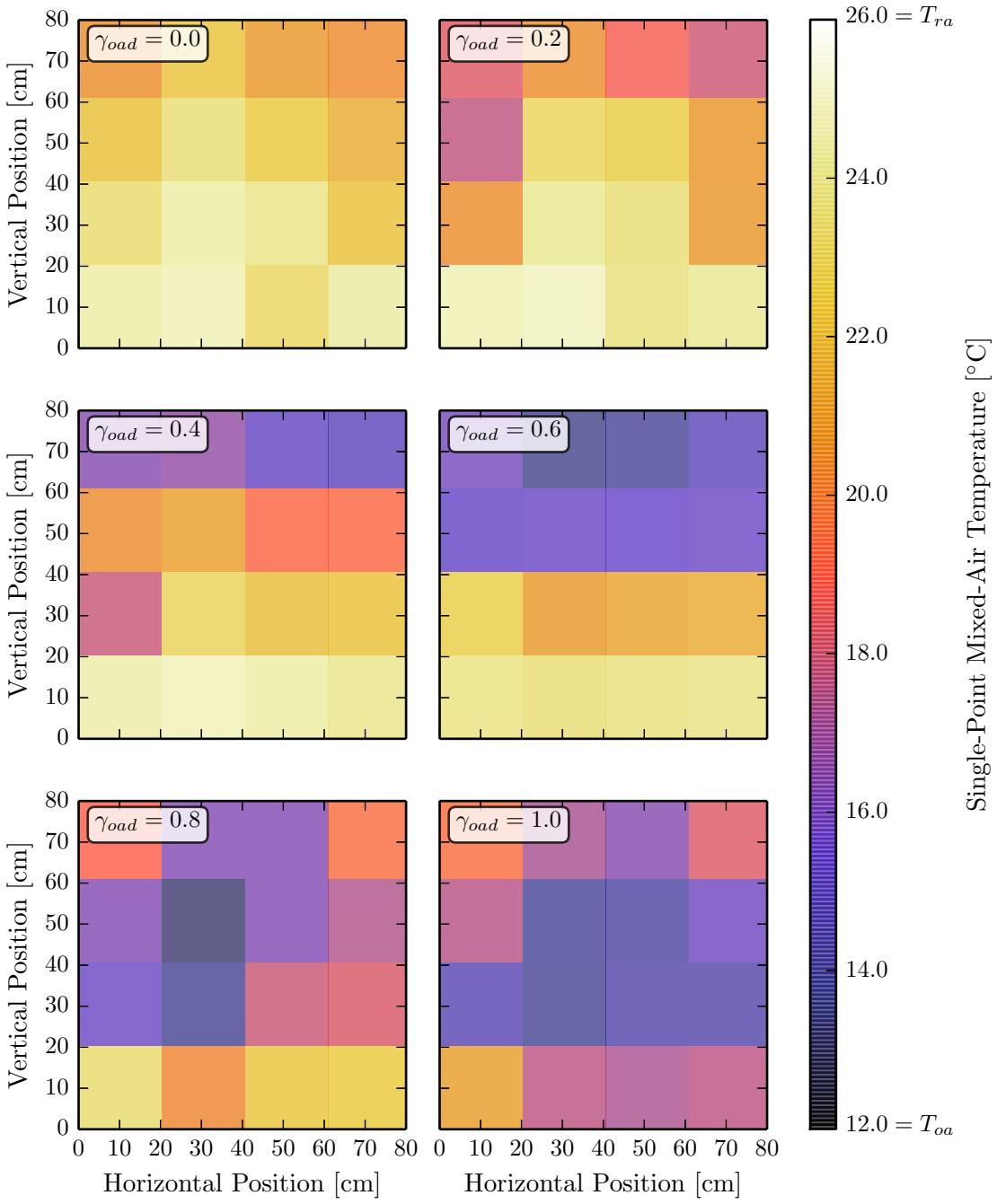

Figure 3.12. Single-point mixed-air temperature measurements at different positions at the evaporator inlet when the outdoor-air temperature was 12.57 °C. The temperature distribution is non-uniform and dependent on the outdoor-air damper position.

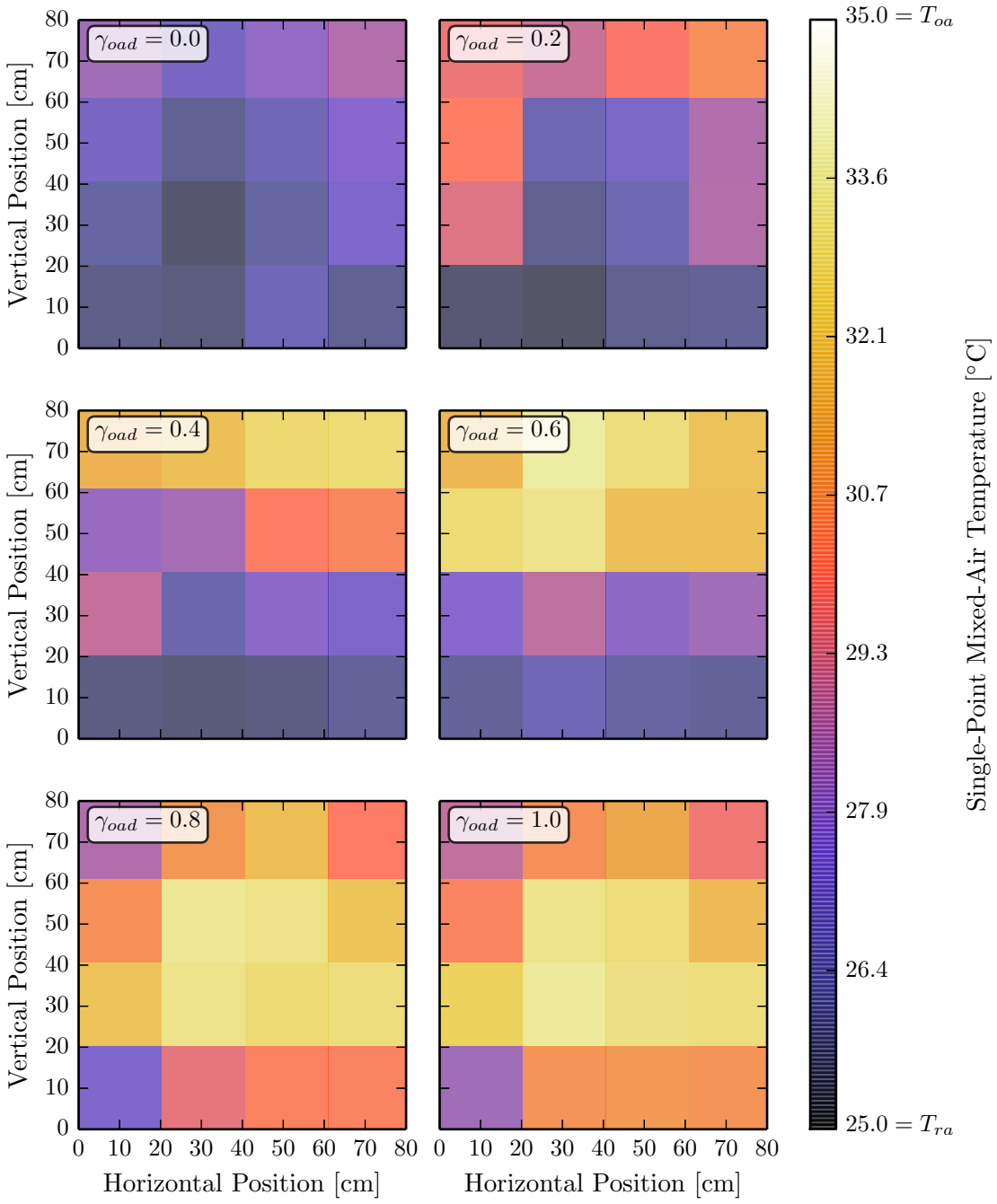

Figure 3.13. Single-point mixed-air temperature measurements at different positions at the evaporator inlet when the outdoor-air temperature was 35.00 °C. The temperature distribution is non-uniform and dependent on the outdoor-air damper position.

3.3.3 Effects of Hysteresis on Mixed-Air Temperature

A system that is said to be affected by hysteresis means that the system has dependence not only on its present environment or state but also its past environment or state. In the RTU, the outdoor-air damper showed signs of hysteresis which could be observed by the adjusted supply-air temperature, $T_{\text{sa,adj}}$. At the same damper position, $T_{\text{sa,adj}}$ had a dependence on whether the damper was opening or closing. This dependence is shown in detail for the range of damper positions in Figure 3.14. For the same outdoor-air and indoor temperature conditions, a difference exists between $T_{\text{sa,adj}}$ when the damper is opening versus when the damper is closing.

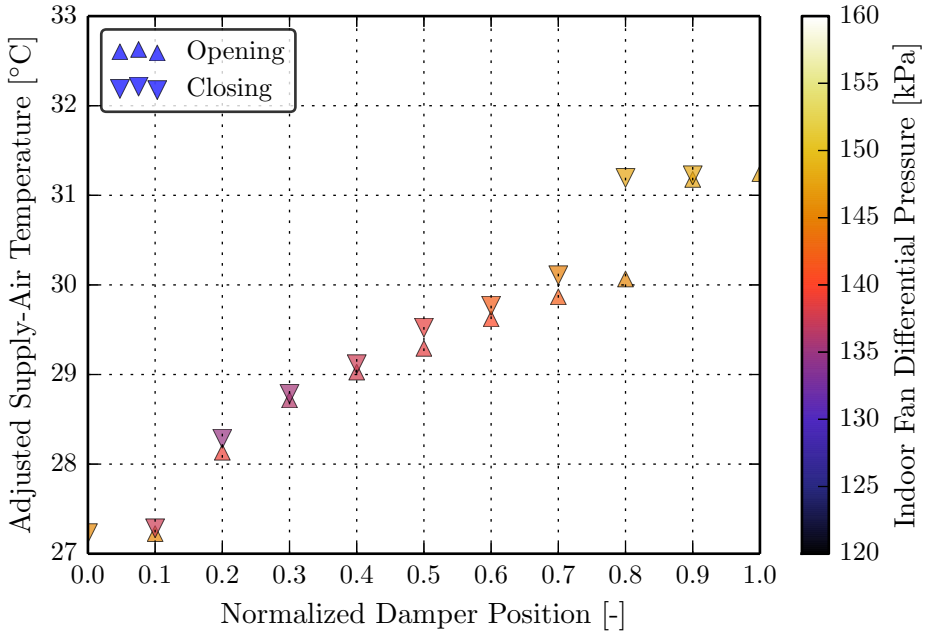

Figure 3.14. Outdoor-air damper position hysteresis effects on the adjusted supply-air temperature, $T_{\text{sa,adj}}$, for the full range of damper positions.

These effects are more clearly shown in Figure 3.15, where the outdoor-air fraction calculated using $T_{\text{sa,adj}}$ is plotted as a function of damper position. Figure 3.15 shows that the difference between opening and closing outdoor-air fractions can be greater than

10 %. Additionally, the plot shows that the difference caused by hysteresis becomes greatest between 40 % and 80 % damper positions. It can also be observed that the indoor-fan differential pressure is affected by hysteresis of the outdoor-air damper. The effect of hysteresis is also dependent on the pressure difference between the return-air and outdoor-air streams. A model to account for this would need to be trained after the RTU is installed on-site because of the uniqueness of different buildings' HVAC systems.

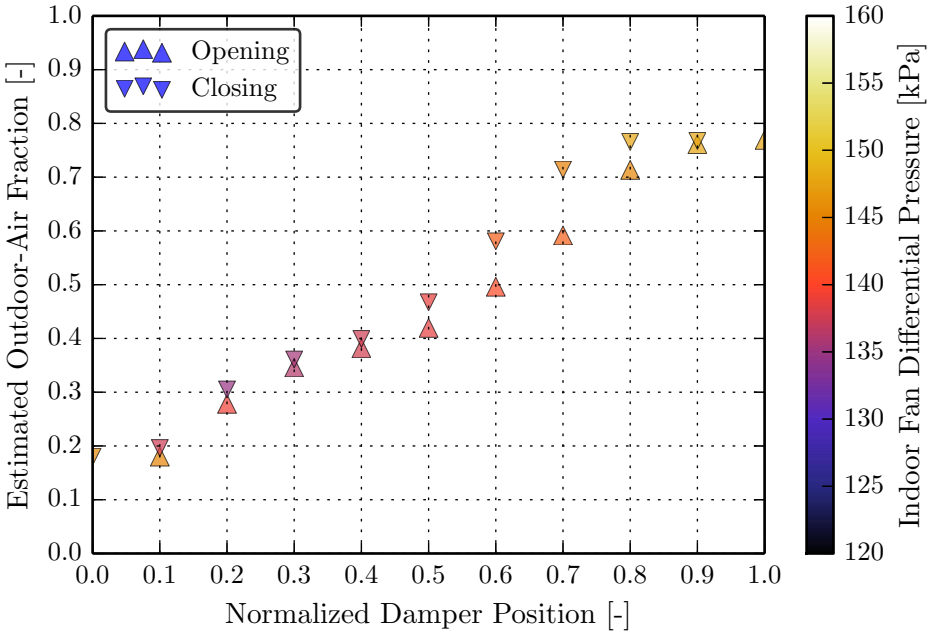

Figure 3.15. Outdoor-air damper position hysteresis effects on the outdoor-air fraction estimated using the adjusted supply-air temperature, $T_{\text{sa,adj}}$, for the full range of damper positions.

3.3.4 Mixed-Air Temperature Correction Model

In order to improve the accuracy of the mixed-air temperature measurement, a model was built accounting for temperature stratification across the evaporator inlet and outdoor-air

damper hysteresis. Using least squares regression, the coefficients of Equation (3.10) were determined using experimental data,

$$T_{\text{ma,corr}} = c_0 + c_1 T_{\text{ma,meas}} + c_2 \dot{m}_{\text{sa,virtual}} + c_3 \left(T_{\text{oa}} - T_{\text{ra}}\right) \gamma_{\text{oad}} \tag{3.10}$$

where $T_{\text{ma,meas}}$ is the measured mixed-air temperature, $\dot{m}_{\text{sa,virtual}}$ is the virtual supply-air mass flow rate measurement (see Section 3.5.1), T_{oa} is the measured outdoor-air temperature, T_{ra} is the measured return-air temperature and γ_{oad} is the normalized damper control signal. The virtual supply-air mass flow rate measurement, $\dot{m}_{\text{sa,virtual}}$, is included in Equation (3.10) in order to capture the influence mixing box flow on the outdoor-air fraction.

$T_{\text{ma,meas}}$ was measured at Location 6, near the center of the temperature measurement grid shown in Figure 2.4. Equation (3.10) was fit using experimental data collected for all sixteen mixed-air temperature sensors and the resulting RMSE and maximum absolute deviations, MAD, before and after correction are shown in Table 3.2. Because Location 6 had lowest combination of RMSE and MAD after correction, it was chosen as the best mixed-air temperature locations and will be used throughout the rest of the analysis. The resulting corrected mixed-air temperature, $T_{\text{ma,corr}}$, is shown in Figure 3.16 as a function of $T_{\text{sa,adj}}$.

Table 3.2.
Root-mean-square error, RMSE, and maximum absolute devation, MAD, between the single-point mixed-air temperature measurements and ajusted supply-air temperature, before and after applying the correction model.

	Before Correction		After Correction	
Sensor	RMSE [°C]	MAD [°C]	RMSE [°C]	MAD [°C]
1	2.714	6.717	0.703	2.194
2	3.359	8.778	0.680	1.909
3	3.779	8.987	0.688	2.090
4	3.592	9.211	0.704	2.224
5	2.378	6.457	0.614	1.504
6	3.534	8.938	0.554	1.320
7	2.123	6.336	0.649	1.916
8	2.463	6.745	0.587	1.416
9	2.697	6.502	0.643	1.942
10	3.558	7.407	0.583	1.597
11	2.395	4.897	0.590	1.635
12	2.287	5.379	0.616	1.565
13	4.876	9.419	0.653	2.337
14	4.210	9.108	0.668	2.192
15	4.631	9.154	0.695	2.243
16	4.223	8.884	0.681	2.328

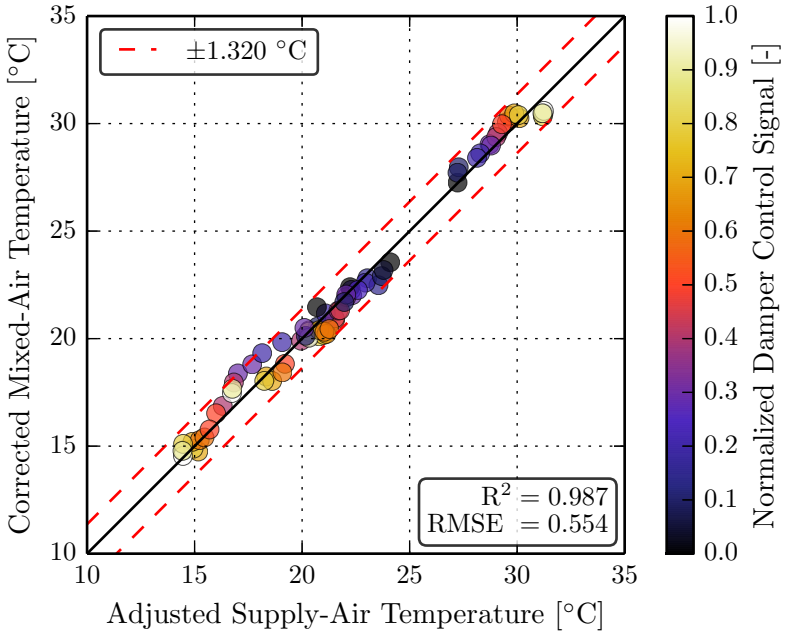

Figure 3.16. Corrected mixed-air temperature, $T_{\text{ma,corr}}$, as a function of adjusted supply-air temperature, $T_{\text{sa,adj}}$. By accounting for the stratification dependence on damper position and the effects of hysteresis, an improvement in mixed-air temperature measurement is achieved.

3.4 Outdoor-Air Fraction Prediction using Damper Control Signal

Air-side temperature measurements can be used to provide an accurate estimation of the current OAF provided by the economizer. The mixed-air temperature, T_{ma} can be used to calculate OAF_{ma} using Equation (3.3). This estimate can be made more accurate using the mixed-air temperature corrected for poor mixing characteristics inside the mixing box of the RTU, $T_{\text{ma,corr}}$. An alternative temperature-based method for estimating OAF uses the supply-air temperature adjusted for indoor fan temperature rise:

$$\text{OAF}_{\text{sa}} = \frac{T_{\text{sa,adj}} - T_{\text{ra}}}{T_{\text{oa}} - T_{\text{ra}}} \tag{3.11}$$

where $T_{\text{sa,adj}}$ is given by Equation (3.6). Equation (3.11) is only useful there is no active cooling or heating. Both OAF_{ma} and OAF_{sa} depend on accurate temperature measurements for each air stream. Moreover, the temperature difference between T_{oa} and T_{ra} in the denominator of each estimate can cause inaccurate OAF estimations when this difference approaches zero. For this reason, Equations (3.3) or (3.11) are not typically evaluated for small differences between T_{oa} and T_{ra}.

In order to make the outdoor-air fraction estimate more reliable, Equations (3.3) or (3.11) were calculated using the corrected outdoor-air, $T_{\text{oa,corr}}$, and corrected mixed-air temperature, $T_{\text{ma,corr}}$:

$$\text{OAF}_{\text{ma}} = \frac{T_{\text{ma,corr}} - T_{\text{ra}}}{T_{\text{oa,corr}} - T_{\text{ra}}} \tag{3.12}$$

and

$$\text{OAF}_{\text{sa}} = \frac{T_{\text{sa,adj}} - T_{\text{ra}}}{T_{\text{oa,corr}} - T_{\text{ra}}}. \tag{3.13}$$

A comparison of these estimates under the same ambient conditions is shown in Figure 3.17. The two OAF estimations are in agreement to within $10.66\,\%$ for all conditions tested and have a RMSE of $4.70\,\%$. Because of this agreement, a comparison between these two estimations can be made during fan-only mode for the purpose of temperature sensor fault detection.

Because temperature-based estimates of OAF rely on accurate measurements, temperature sensor faults can impact significantly. In order to avoid this problem, an OAF model

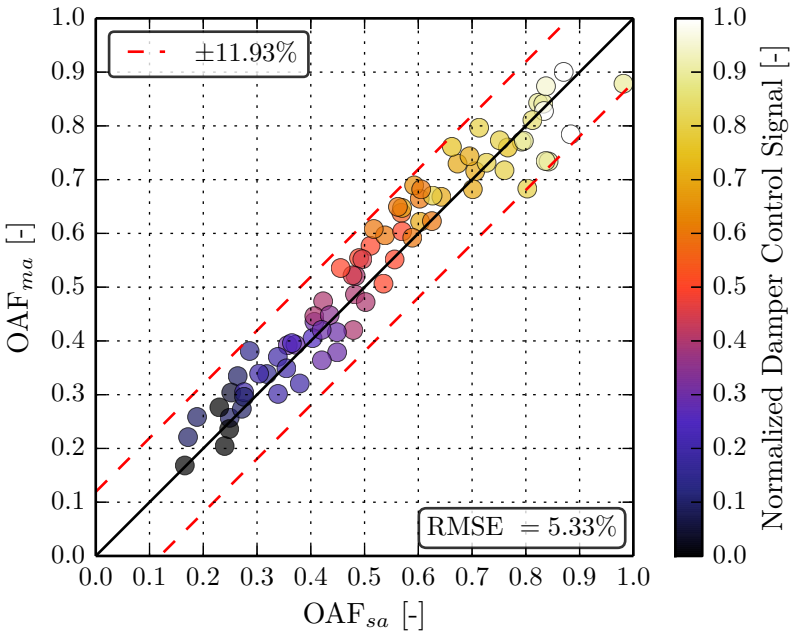

Figure 3.17. Comparison of temperature-based outdoor-air fraction estimations after applying correction models to the outdoor-air, mixed-air, and supply-air temperature measurements.

based on the outdoor-air damper control signal was designed. The purpose of this sensor is to provide an expected OAF estimation only based on the outdoor-air damper control signal. By using the control signal, an estimation of what the OAF should be in a normally operating system can be made. A comparison with this expected OAF with the air temperature-based estimates can be used to detect faults.

The expected OAF based on the outdoor-air damper control signal, OAF_{oad}, takes the form of the third-order polynomial in Equation (3.14).

$$\text{OAF}_{\text{oad}} = c_0 + c_1\gamma_{\text{oad}} + c_2\gamma_{\text{oad}}^2 + c_3\gamma_{\text{oad}}^3 \tag{3.14}$$

where γ_{oad} is the normalized outdoor-air damper control signal. The coefficients of Equation (3.14) were determined using ordinary least squares regression where OAF_{sa} was used for the dependent variable. A comparison of OAF_{oad} with OAF_{sa} is shown in Figure 3.18. A similar comparison between OAF_{oad} and OAF_{ma} is shown in Figure 3.19.

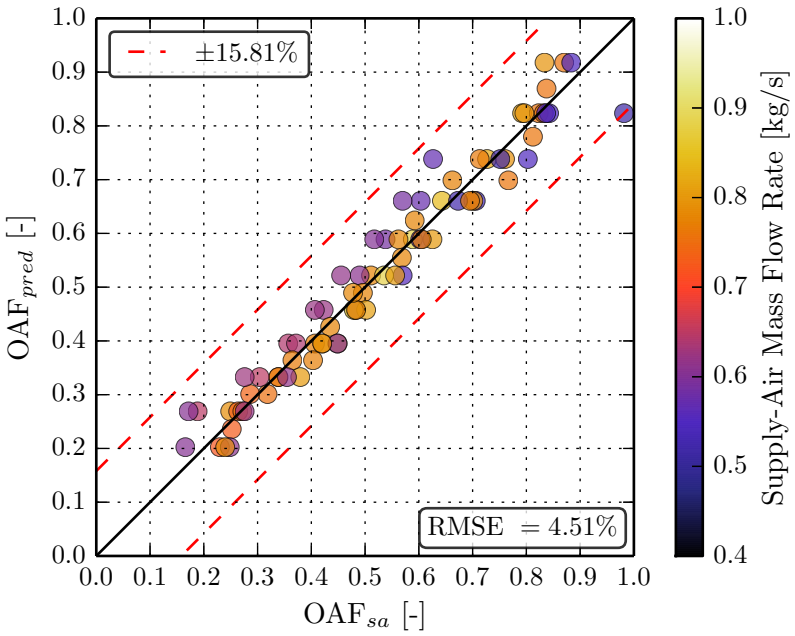

Figure 3.18. Comparison of of the predicted outdoor-air fraction using the damper control signal to the supply-air temperature-based outdoor-air fraction estimation.

3.5 Virtual Indoor Fan Performance Sensors using Air-side Measurements

3.5.1 Virtual Supply-Air Mass Flow Rate Sensor

In order to adjust the supply-air temperature measurement for the indoor fan temperature rise, a supply-air mass flow measurement is required. A mass air flow measurement in practice is expensive and typically converts a volumetric flow rate measurement using an air density correlation. Alternative estimates for supply-air that use low-cost measurements have been proposed previously in the literature.

Kim describes a virtual evaporator mass air flow sensor using refrigerant-side measurements [7]. In the method, an energy balance is performed on the refrigerant entering and leaving the evaporator. Using a virtual refrigerant mass flow rate sensor, the virtual evaporator air mass flow rate is determined. The virtual evaporator air flow rate sensor was

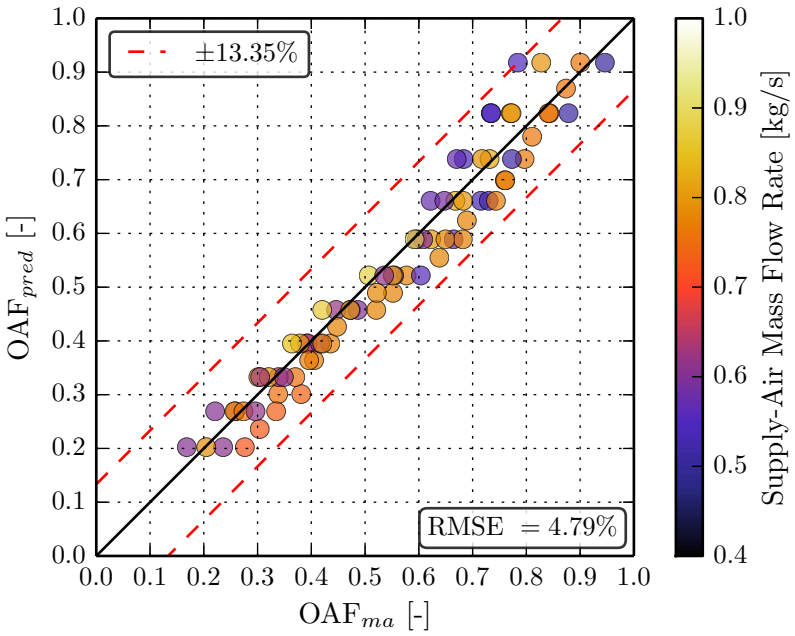

Figure 3.19. Comparison of of the predicted outdoor-air fraction using the damper control signal to the mixed-air temperature-based outdoor-air fraction estimation.

tested using a wide range of test conditions and equipment types with good accuracy. A disadvantage of the method is that it can only be applied when mechanical cooling is being provided. Because of this, the virtual evaporator air mass flow rate cannot be applied when the RTU is in "Fan-Only Mode".

The supply-air mass flow rate, $\dot{m}_{\text{sa}}$, is mapped as a function of indoor fan differential pressure, ΔP_{idf}, and normalized indoor fan control frequency, γ_{idf} in Figure 3.20. A sigmoidal function taking the form of Equation (3.15) was used to capture the relationship between $\dot{m}_{\text{sa}}$ and ΔP_{idf} and γ_{idf},

$$\dot{m}_{\text{sa,virtual}} = \frac{c_0 + c_1\gamma_{\text{idf}}}{1 + c_2 \exp\left(c_3 + c_4\Delta P_{\text{idf}}\right)} + c_5\Delta P_{\text{idf}}. \tag{3.15}$$

The coefficients c_{0-5} of Equation (3.15) were determined using non-linear least squares regression in order to minimize the mean-square error between the measured supply-air mass flow rate and the virtual supply-air mass flow rate. Because of the nonlinear form of

$\dot{m}_{\text{sa,virtual}}$, precaution was used to ensure that the initial guess values for c_{0-5} gave a global minimum value for the mean-square error.

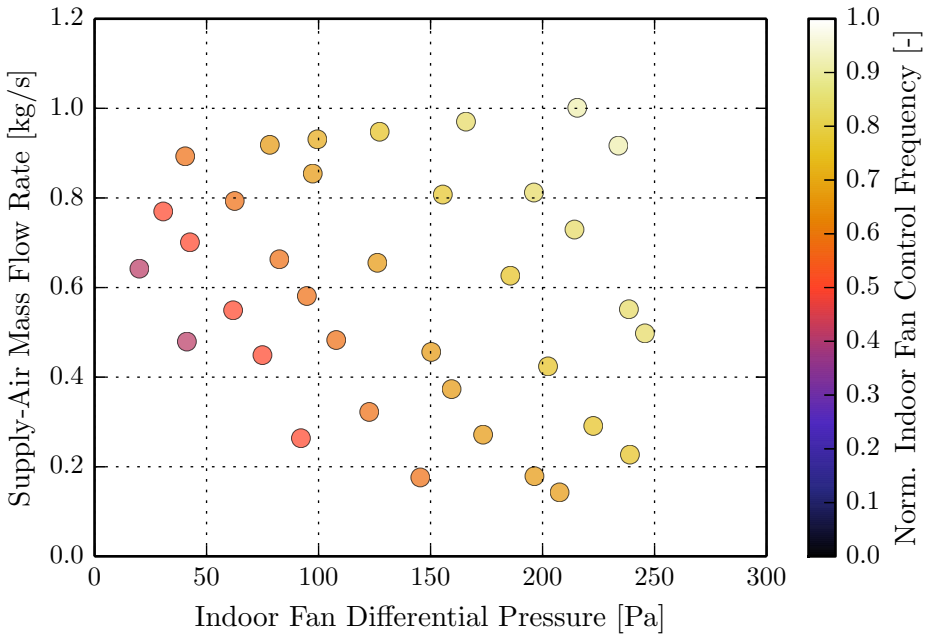

Figure 3.20. Supply-air mass flow rate, $\dot{m}_{\text{sa}}$, measured as a function of indoor fan differential pressure, ΔP_{idf}, and normalized indoor fan control frequency, γ_{idf}.

The resulting $\dot{m}_{\text{sa,virtual}}$ is plotted as a function of the measured $\dot{m}_{\text{sa}}$ in Figure 3.21. The $\dot{m}_{\text{sa,virtual}}$ has a maximum deviation of $0.072\,\text{kg/s}$ and a RMSE of $0.0332\,\text{kg/s}$. Utilizing the control frequency of the indoor fan variable frequency drive (VFD) and a differential pressure sensor observing air pressures at the inlet and outlet of the fan, an estimation of the supply-air mass flow rate can be obtained. The sensors required to make this estimation are also relatively low-cost when compared to the cost of a hot-wire or vane anemometer which could be used as an alternative.

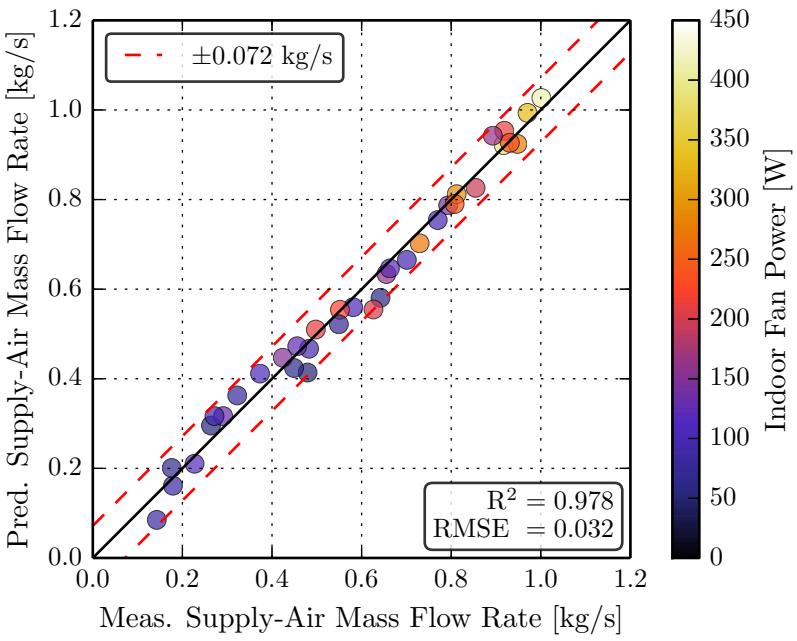

Figure 3.21. Virtual supply-air mass flow rate, $\dot{m}_{\text{sa,virtual}}$ based on indoor fan measurements as a function of the actual supply-air mass flow rate, $\dot{m}_{\text{sa}}$.

3.5.2 Virtual Indoor Fan Power Sensor

Indoor fan power is an important measurement used to determine the impact of RTU faults on system performance and operating cost. Faults such as evaporator fouling or loose indoor fan belt can reduce indoor fan flow rate or increase indoor fan power. In the case of a variable speed indoor fan, a fault may cause the system to operate the fan at a higher frequency, consuming more power.

The indoor fan power, $\dot{W}_{\text{idf}}$, is mapped as a function of indoor fan differential pressure, ΔP_{idf}, and normalized indoor fan control frequency, γ_{idf} in Figure 3.22. A sigmoidal function taking the form of Equation (3.16) was used to capture the relationship between $\dot{W}_{\text{idf}}$ and ΔP_{idf} and γ_{idf},

$$\dot{W}_{\text{idf,virtual}} = \frac{c_0 + c_1\gamma_{\text{idf}}}{1 + c_2 \exp\left(c_3 + c_4\Delta P_{\text{idf}}\right)} + c_5\Delta P_{\text{idf}}. \tag{3.16}$$

The coefficients c_{0-5} of Equation (3.16) were determined using non-linear least squares regression in order to minimize the mean-square error between the measured indoor fan power and the virtual indoor fan power calculated. Because of the nonlinear form of $\dot{W}_{\text{idf,virtual}}$, precaution was used to ensure that the initial guess values for c_{0-5} gave a global minimum value for the mean-square error.

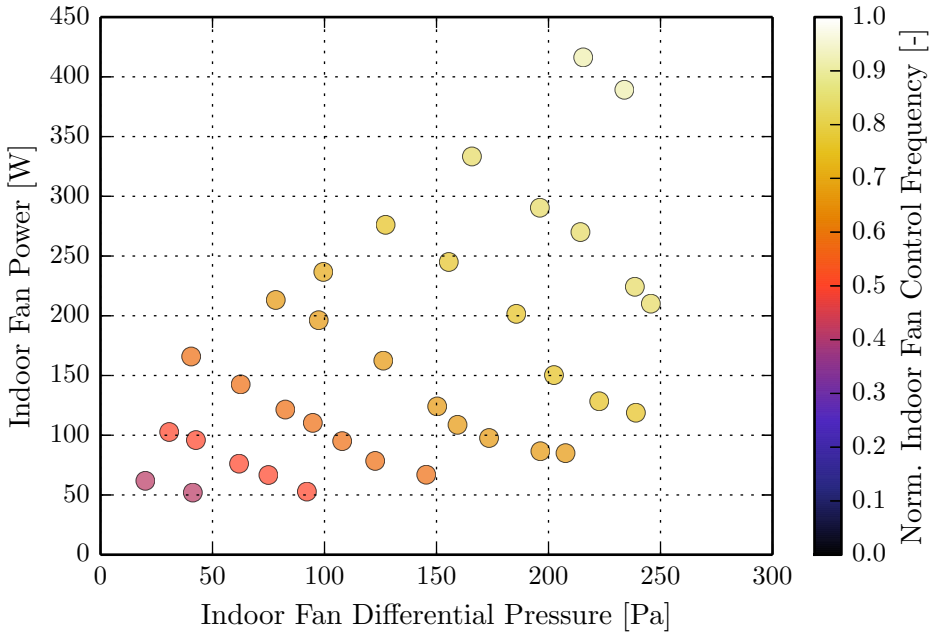

Figure 3.22. Indoor fan power, $\dot{W}_{\text{idf,virtual}}$, measured as a function of indoor fan differential pressure, ΔP_{idf}, and normalized indoor fan control frequency, γ_{idf}.

The resulting $\dot{W}_{\text{idf,virtual}}$ is plotted as a function of the measured $\dot{W}_{\text{idf}}$ in Figure 3.23. The $\dot{W}_{\text{idf,virtual}}$ has a maximum deviation of $33.44\,\text{W}$ and a RMSE of $15.06\,\text{W}$. Utilizing the control frequency of the indoor fan variable frequency drive (VFD) and a differential pressure sensor observing air pressures at the inlet and outlet of the fan, an estimation of the indoor fan power can be obtained. The sensors required to make this estimation are relatively inexpensive when compared to the cost of an actual power meter with similar obtainable accuracy.

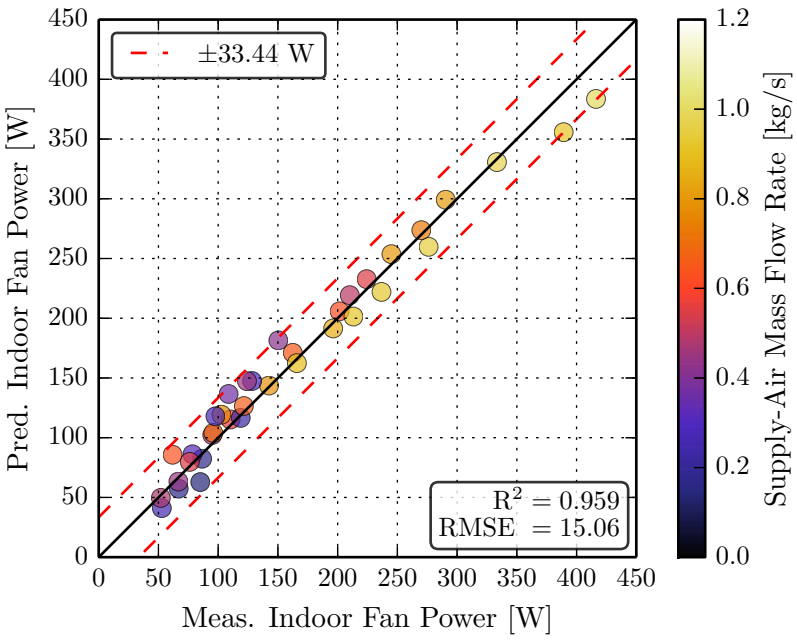

Figure 3.23. Virtual indoor fan power, $\dot{m}_{\text{sa,virtual}}$ based on indoor fan measurements as a function of the actual indoor fan power, $\dot{m}_{\text{sa}}$.

4. ECONOMIZER AFDD METHOD

4.1 Introduction

An economizer fault detection and diagnosis method is described in the following chapter. The methods and components, including the steady-state detector, fault detection method, and fault diagnosis method, are described in detail in Section 4.2. An evaluation of the method's performance against stuck damper faults and different temperature sensor faults follows in Section 4.3. Finally, conclusions and further recommendations are made Section 4.4.

4.2 Description of AFDD Technique

The data flow and operations of the fault detection and diagnosis method are shown in Figure 4.1. The FDD tool is connected to a data acquisition system and data is sequentially processed as it becomes available. During this step, the data acquisition is polled by the FDD tool at a predefined frequency for newly available data. For the analysis preformed in this section, the sampling frequency was set to the highest possible by the data acquisition system and LabView software, 6 s to 7 s between points. When new data is available, the tool enters a preprocessing stage.

In the preprocessing stage, the data collected from the data acquisition system is cleansed of any extreme values and a common set of variable names are defined for use in the rest of the tool. Additionally, any unit conversion required is performed on the data.

After the data is preprocessed, virtual sensors and temperature sensor correction models are evaluated. These include the outdoor-air temperature correction, mixed-air temperature correction, and predicted outdoor-air fraction based on the damper control signal described in Chapter 3. Virtual supply-air mass flow rate and indoor fan power sensors are also evaluated in order to account for the indoor-fan temperature rise.

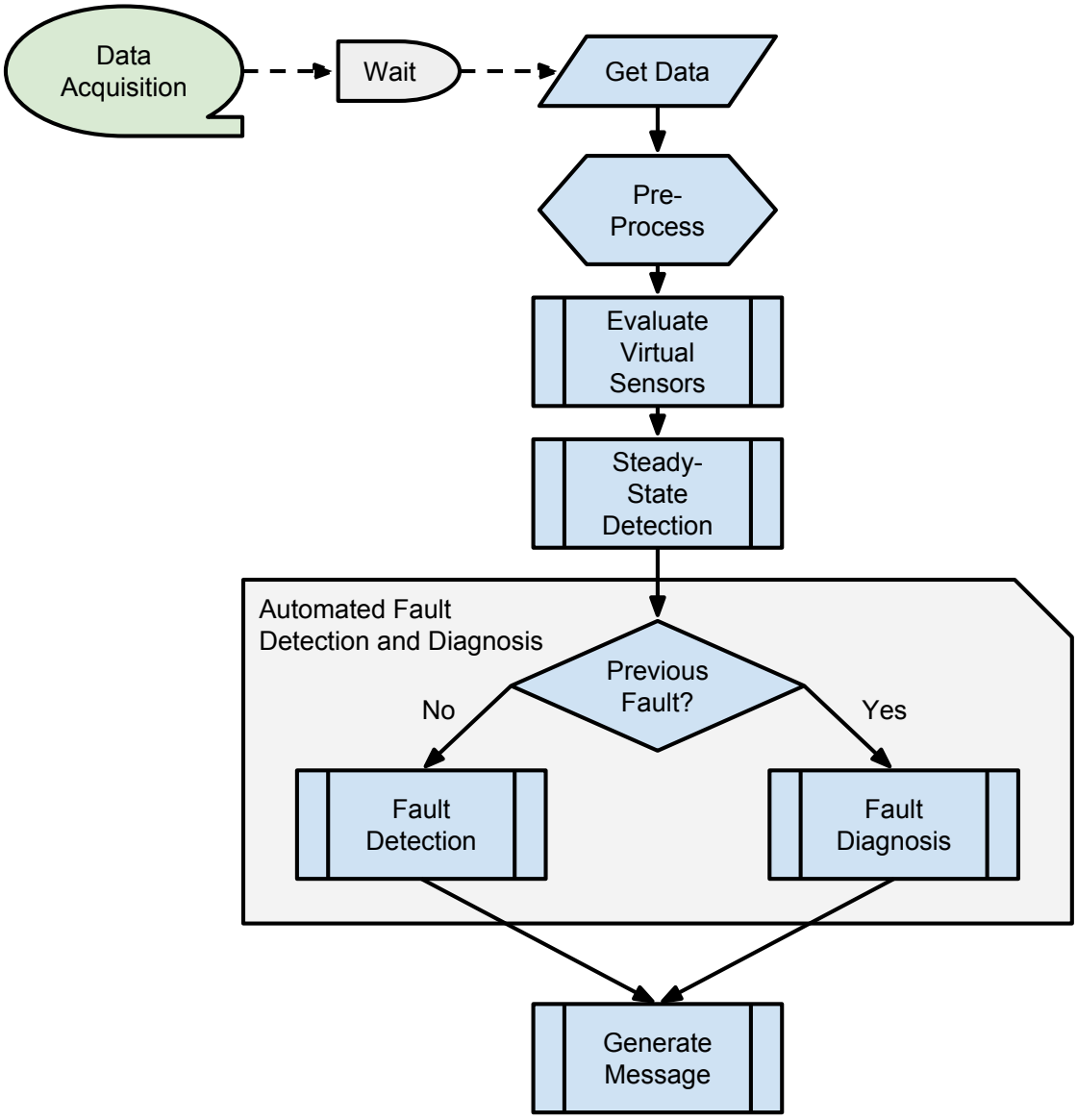

Figure 4.1. Overall economizer fault detection and diagnosis method flow chart.

A steady-state filter is used to filter any transient data that may cause fault detection false alarms or diagnosis misclassifications. This detector is applied to the inputs of the fault detection and diagnosis input variables and is described in more detail in Section 4.2.1.

Automated fault detection and diagnosis is performed after the steady-state detector has filtered the input parameters. If no previous faults have been identified, or if the RTU is in an active heating or cooling mode, fault detection is conducted using a Bayesian fault classifier. At this stage, data is collected and the state of the equipment is determined. If a fault has been previously detected and the RTU has no call for heating or cooling, the active economizer diagnosis state is entered. During this state, the damper position is manipulated and a fault diagnosis is determined based on the observed performance. Finally, the current status of the RTU economizer is reported back to the building operator or service provider containing fault detection and diagnoses if present.

The information required by the FDD method includes the four ventilation air temperatures: outdoor, return, mixed, and supply. One other measurement of outdoor-air temperature is optionally required in order to improve diagnostic performance. This measurement could be a condenser-air inlet temperature or from a local weather station. Control signals that are monitored are the outdoor air damper actuator signal and the indoor fan control frequency. The thermostat call for heating or cooling is also used in order to determine whether the heating coil or compressor is on. The presented system is for a high-limit or differential dry-bulb economizer. This is not really a limitation of the AFDD method and could be extended to enthalpy-based economizer control which use humidity measurements (see Section 4.4).

4.2.1 Steady-State Detector

In order to exclude the effects of system dynamics on the FDD method, a steady-state detector is used to filter unsteady operation. Since many packaged units operate in a quasi-steady state for much of the day, filtering out points that may cause false alarms is important.

This is especially true for economizers since the damper control is based on the cooling demand signal and ambient temperature/enthalpy conditions.

To determine when the economizer (and RTU ventilation) has become steady, two previously proposed calculations are performed on-line and compared with respective thresholds, [5–7]. First, the trend of the time-series is determined using a simple least-squares fit applied to the samples in the moving window. If the slope of the line over the moving window exceeds a trend threshold, FDD is not applied and the procedure is repeated once a new sample has been recorded. The second test performed is a moving variance calculation. If the variance calculated exceeds a variance threshold, FDD is not applied and the procedure is repeated after a new sample is recorded. Moreover, in order to perform FDD the data must meet both criteria.

4.2.2 Fault Detection Method

Rossi describes a method for using a Bayesian classifier to detect and diagnose refrigerant-side faults on packaged air-conditioners [5]. This method will be described and extended to detecting economizer faults caused by incorrect or stuck damper positions and temperature sensor faults. A Bayes classifier for a normal distribution is given by Equation (4.1) [25],

$$\frac{1}{2}\left(X-M_1\right)^T\Sigma_1^{-1}\left(X-M_1\right)-\frac{1}{2}\left(X-M_2\right)^T\Sigma_2^{-1}\left(X-M_2\right)+\frac{1}{2}\ln\frac{|\Sigma_1|}{|\Sigma_2|}\gtrless\ln\frac{\mathbb{P}_1}{\mathbb{P}_2} \quad (4.1)$$

where M is the mean vector, Σ is the covariance matrix, X is the current information vector, and $\mathbb{P}$ is the *a priori* probability for the distribution. The subscripts 1 and 2 correspond to the normal performance which is determined based on models developed from laboratory testing and the current performance which is determined using recent measurements, respectively. Equation (4.1) is a rule for determining whether current operation is normal or faulty by minimizing the error of a wrong decision. If a fault mostly impacts the difference between the expected normal and current performance (i.e. the mean vectors), then it can be assumed

that $\Sigma_1 = \Sigma_2 = \Sigma$ without loss of accuracy. With this simplification, Equation (4.1) can be reduced to

$$(M_2 - M_1)^T \Sigma^{-1} X + \frac{1}{2}\left(M_1^T \Sigma^{-1} M_1 + M_2^T \Sigma^{-1} M_2\right) \gtrless \ln \frac{\mathbb{P}_1}{\mathbb{P}_2} \tag{4.2}$$

where Σ can be determined using a weighted average of Σ_1 and Σ_2:

$$\Sigma = s\Sigma_1 + (1+s)\Sigma_2. \tag{4.3}$$

In order to minimize the probability of making a wrong decision (and maximizing detection performance), the value of s is determined using an optimization algorithm. The procedure for determining the minimum s is as follows [25].

1. Calculate:
$$V = \left[s\Sigma_1 + (1-s)\,\Sigma_2\right]^{-1}(M_2 - M_1)\,. \tag{4.4}$$

2. Calculate:
$$\sigma_i^2 = V^T \Sigma_i V \quad \text{for } i = 1 \text{ and } 2\ . \tag{4.5}$$

3. Calculate:
$$v_0 = -\frac{s\sigma_1^2 V^T M_2 + (1-s)\,\sigma_2^2 V^T M_1}{s\sigma_1^2 + (1-s)\,\sigma_2^2}. \tag{4.6}$$

4. Calculate:
$$\eta_i = V^T M_i + v_0 \quad \text{for } i = 1 \text{ and } 2\ . \tag{4.7}$$

5. Calculate the classification error:
$$\epsilon = \mathbb{P}_1 \operatorname{erfc}\left(-\frac{\eta_1}{\sqrt{2\sigma_1^2}}\right) + \mathbb{P}_2 \operatorname{erfc}\left(-\frac{\eta_2}{\sqrt{2\sigma_2^2}}\right). \tag{4.8}$$

6. Find s between 0 to 1 that minimizes ϵ.

The underlying theory of the fault detection procedure can be visualized in Figure 4.2 and 4.3. Using fault-free training data, an expected performance model can be learned. This model could then be compared with recent observed data to calculate a performance residual. When no faults exist in the system, the observed distribution should closely overlap the

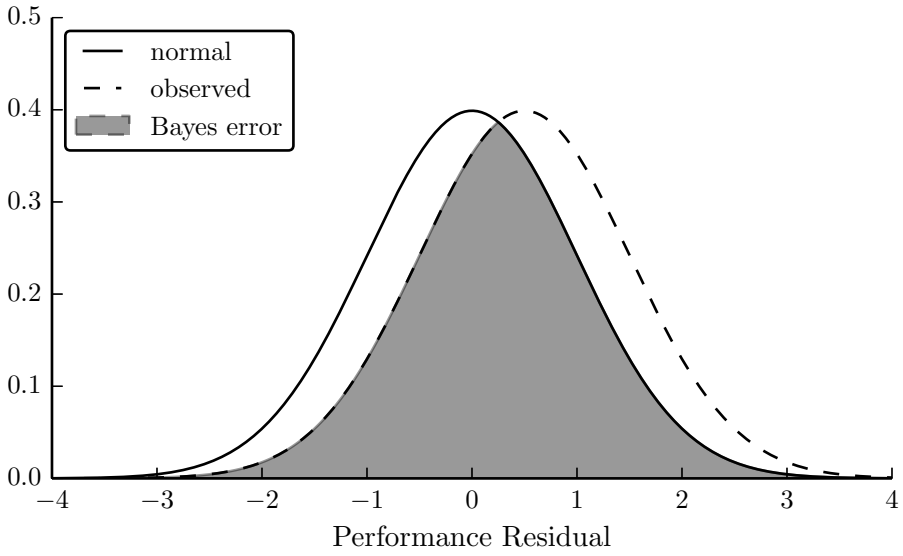

Figure 4.2. When the system operates normally, the expected and observed residual distributions should overlap significantly. This overlap area is equal to the classification error.

expected distribution based on fault-free data, as shown in Figure 4.2. During this scenario, insufficient evidence exists to detect a fault.

However, if a fault is introduced to a system or an existing problem becomes more severe in the system, normally expected and observed distributions will start to deviate, shown in Figure 4.3. When error between the two distributions becomes small enough, a fault would be declared by the Bayes classifier. Determining the threshold between normal and faulty diagnoses is accomplished by specifying a level of confidence in determining a fault condition. If a $99\,\%$ level of confidence was desired before declaring a fault, the maximum Bayes error would be $1\,\%$, since the overlapping area between the two distributions is maximum at unity.

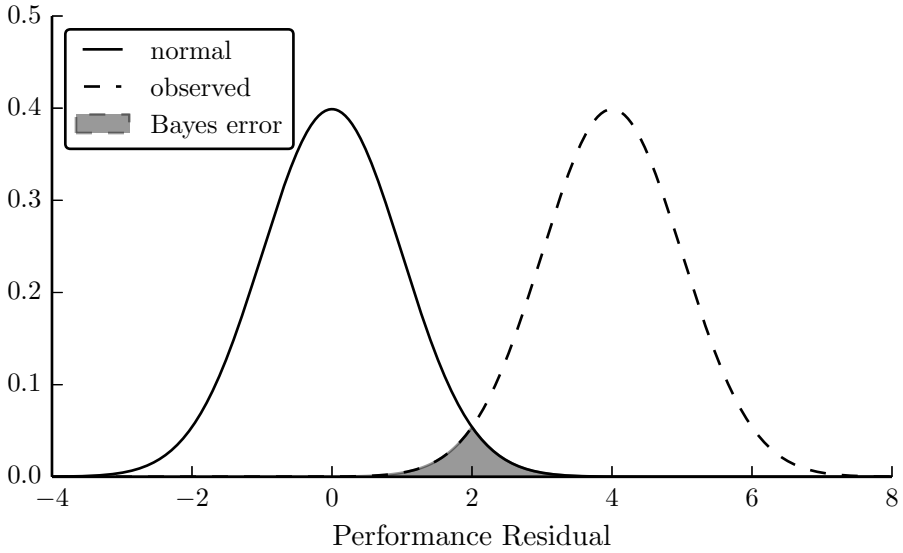

Figure 4.3. When a fault is introduced to the system, the observed distribution will deviate from the expected normal distribution. When the overlapping area becomes less than a threshold, a fault can be declared.

In order to detect economizer performance deviations, it is natural to use outdoor-air fraction (OAF) observations. Current OAF estimations based on temperature measurements, OAF_{ma} and OAF_{sa}, can be determined using Equations (3.12) and (3.13) respectively. These measurements can be compared the predicted outdoor-air fraction, OAF_{oad}, determined

using Equation (3.14). When a significant deviation persists between the estimated and predicted outdoor-air fractions, a fault may be detected.

For any mode of operation when the indoor fan is operating, the difference between OAF_{oad} and OAF_{ma} can be calculated. This residual, given by Equation (4.9), can be characterized during normal operation using experimental test data under different ambient conditions and operating modes,

$$r_{\text{ma}} = \text{OAF}_{\text{oad}} - \text{OAF}_{\text{ma}}. \tag{4.9}$$

The distribution of these residuals is shown in Figure 4.4 after applying the outdoor-air, mixed-air, and supply-air temperature correction models. A normal distribution was assumed to describe the experimental data and the resulting probability density function determined using the mean, μ, and standard deviation, σ, is shown on Figure 4.4 as well.

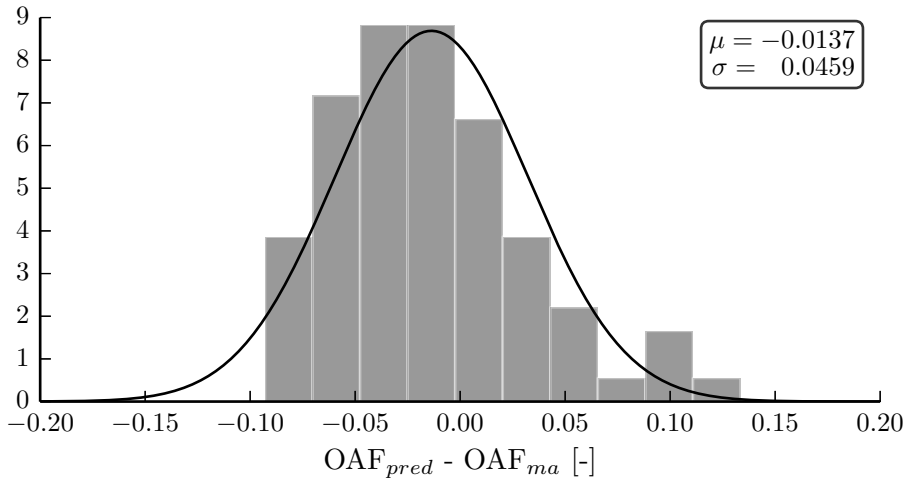

Figure 4.4. Distribution of the normal outdoor-air fraction residual determined experimentally when the damper is operating properly and there are no temperature sensor faults. A normal distribution was assumed and the resulting empirical probability density function is shown.

When the RTU enters ”fan-only” mode, a better estimate of outdoor-air fraction can be made using the supply-air temperature. During this operating mode, a residual between estimated and predicted OAF using Equation (4.10),

$$r_{\text{sa}} = \text{OAF}_{\text{oad}} - \text{OAF}_{\text{sa}}. \tag{4.10}$$

In order to determine an expected model for this residual, normal operation experimental data was used to determine the distribution. These experimental data and the empirical probability density function are shown in Figure 4.5

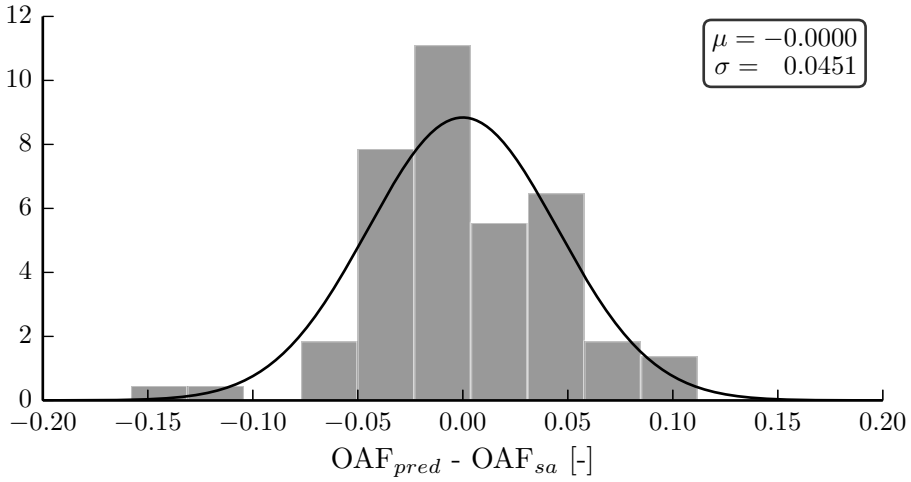

Figure 4.5. Distribution of the normal outdoor-air fraction residual calculated using supply-air temperature determined experimentally when the damper is operating properly and there are no temperature sensor faults. A normal distribution was assumed and the resulting empirical probability density function is shown.

4.2.3 Fault Diagnoses Method

A limitation of passive fault detection methods is the masking of faults that are not affecting system performance under a given set of operating conditions. Because the faults are masked, diagnoses of the faults are impossible. In order to overcome this issue, it is

possible in some cases to take control of the system in order to produce situations when the fault can be observed. Such methods are known as active testing or diagnoses methods. In the case of the RTU with integrated economizer, control of the damper actuator can be used to force the system into operation expressing fault symptoms.

The fault diagnoses method relies on actuating the the outdoor-air damper fully-closed and then fully-open. At these two damper positions, sensor redundancy is achieved since mostly return-air and outdoor-air are supplied at the respective damper positions. A flow chart of the fault diagnosis method is shown in Figure 4.6. When a fault is present in the system, the system measurements will respond in a certain way, lending itself to classification. Before exploring fault symptoms, however, the normal response of the system should be understood.

When the outdoor-air damper is fully-closed, the expected air-flow streams are shown in Figure 4.7. In this position, the return-air temperature, T_{ra}, and mixed-air temperature, T_{ma} should be nearly equal if leakage is negligible. The difference between T_{ra} and T_{ma} can be used as an indicator of normal or faulty operation,

$$r_1 = \left| T_{\text{ra}} - T_{\text{ma}} \right| . \tag{4.11}$$

When certain faults are present in a system, r_1 will become larger than when the system has no faults. For instance, if the damper becomes stuck partially open, outdoor-air will enter the mixing box causing T_{ma} to deviate from T_{ra}. Some faults will not affect r_1, like an outdoor-air temperature sensor fault since it is not considered in Equation (4.11).

When "fan-only" mode is enabled, no mechanical heating or cooling is provided by the RTU. Keeping this in mind, the difference between supply-air temperature, T_{sa}, and T_{ma} should be negligible,

$$r_2 = \left| T_{\text{sa}} - T_{\text{ma}} \right| . \tag{4.12}$$

This is especially true if the indoor fan temperature rise is accounted for using $T_{\text{sa,adj}}$. From Figure 4.8, it can be seen that this performance residual would be affected by only T_{ma} and T_{sa} sensor faults. This is useful in differentiating between damper and temperature faults.

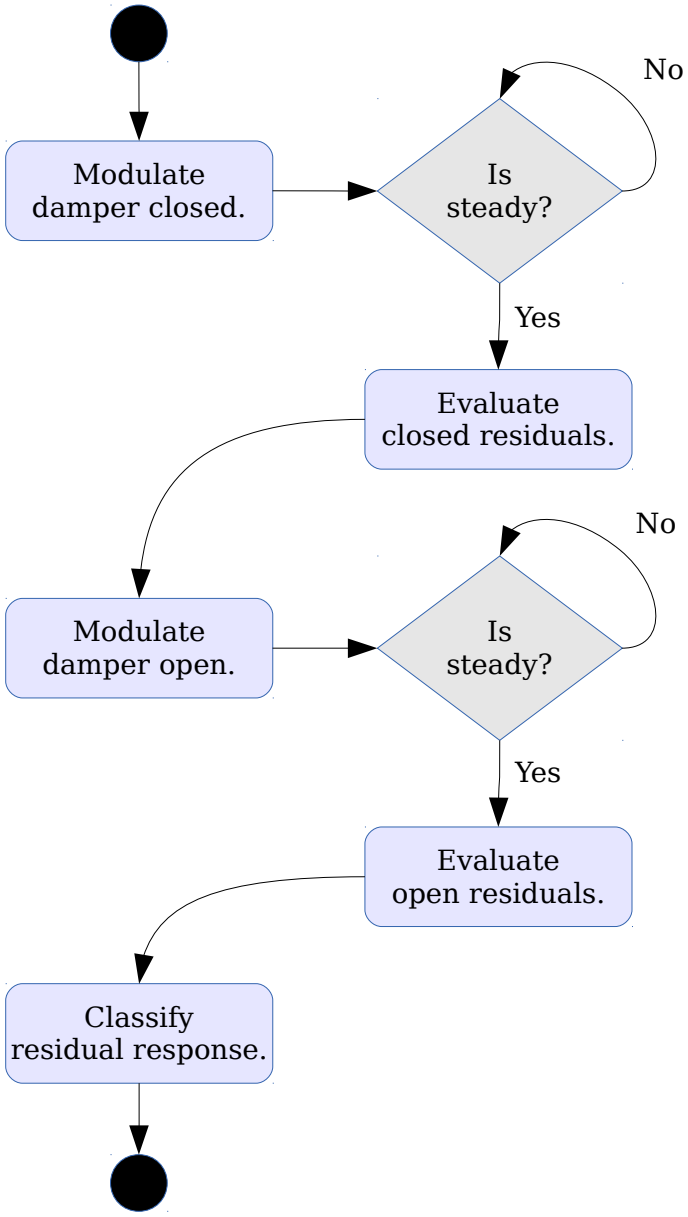

Figure 4.6. Fault diagnosis process using outdoor-air damper control.

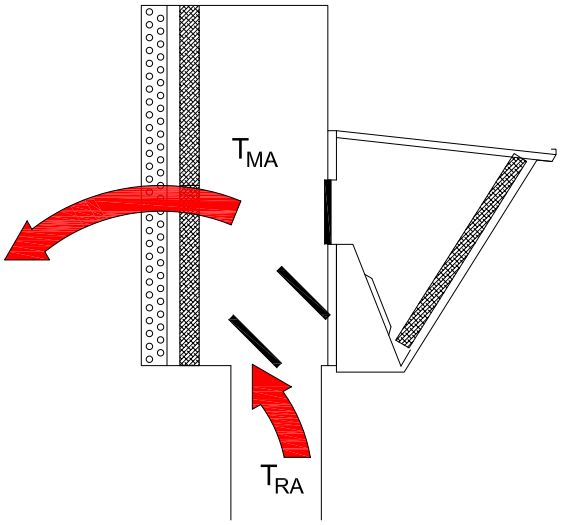

Figure 4.7. When the damper is in the fully-closed position, the return-air temperature, T_{ra}, and mixed-air temperature, T_{ma} should be nearly the same, neglecting leakage.

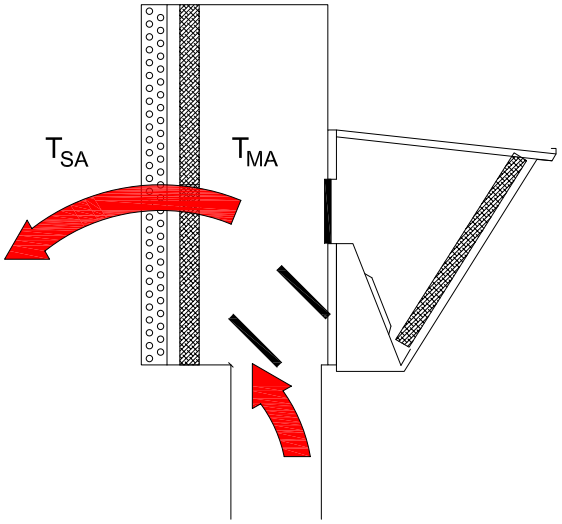

Figure 4.8. When the damper is in the fully-closed position and the RTU is in "fan-only" mode, the supply-air temperature, T_{sa}, and mixed-air temperature, T_{ma} should be nearly equal, after accounting for indoor fan temperature rise.

Differences between predicted outdoor-air fractions, OAF_{oad} and temperature-based outdoor-air fractions, OAF_{ma} and OAF_{sa}, should be small when the outdoor-air damper is closed and the RTU is in "fan-only" mode. Performance residuals formed by these differences can be calculated using Equations (4.13) and (4.14),

$$r_3 = \left|\text{OAF}_{\text{oad}} - \text{OAF}_{\text{ma}}\right|, \tag{4.13}$$

$$r_4 = \left|\text{OAF}_{\text{oad}} - \text{OAF}_{\text{sa}}\right|. \tag{4.14}$$

These residuals are useful in identifying both stuck damper faults and temperature sensor faults. Additionally, when taken together, they can be used to isolate T_{ma} and T_{sa} faults.

A final performance residual that can be calculated when the outdoor-air damper is closed, is one between the outdoor-air temperature, T_{oa}, and a different measurement of the ambient temperature. An indicator of an outdoor-air temperature sensor fault is a large value of r_5 relative to what is expected normally,

$$r_5 = \left|T_{\text{oa}} - T_{\text{oa,robust}}\right|. \tag{4.15}$$

The robust outdoor-air ambient temperature, $T_{\text{oa,robust}}$ can be a measurement retrieved from an external weather service or from a condenser air-outlet temperature used for refrigerant-side FDD methods. Since multiple RTUs are commonly installed on small-to-midsize commercial buildings, a more robust ambient measurement can be estimated using the T_{oa} measurement on each RTU installed at the site.

When the outdoor-air damper is fully-open, different performance residuals can be calculated in order to diagnoses a problem. Under normal operation, the outdoor-air temperature, T_{oa}, should be nearly the same as the mixed-air temperature, T_{ma}, shown by Figure 4.9. Equation (4.16) can be used as an indicator of faulty operation,

$$r_6 = \left|T_{\text{oa}} - T_{\text{ma}}\right|. \tag{4.16}$$

In order to account for the return-air recirculation discussed in Chapter 3, the T_{oa} correction model should be used when calculating Equation (4.16).

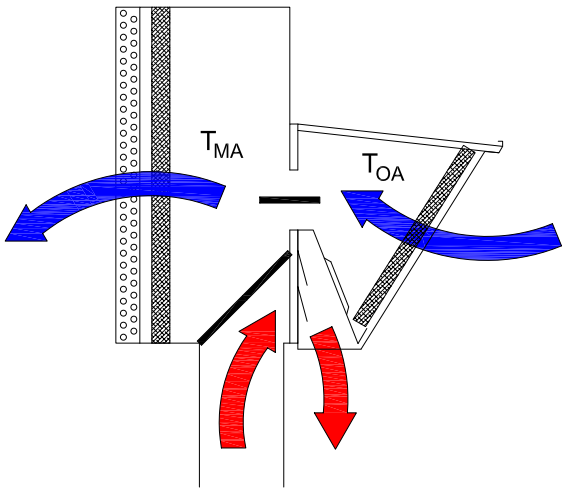

Figure 4.9. When the damper is in the fully-closed position, the return-air temperature, T_{ra}, and mixed-air temperature, T_{ma} should be nearly the same, neglecting leakage.

Just as when the damper is closed, the difference between T_{sa} and T_{ma} should be nearly zero when the RTU is in "fan-only" mode, shown by Figure 4.10. This is especially true when $T_{\text{sa,adj}}$ and $T_{\text{ma,corr}}$ are used in place of T_{sa} and T_{ma} in Equation (4.17),

$$r_7 = \left| T_{\text{sa}} - T_{\text{ma}} \right| . \tag{4.17}$$

Because of return-air recirculation effects and temperature stratification at the mixed-air temperature location, it is especially important to use $T_{\text{ma,corr}}$ when calculating r_7.

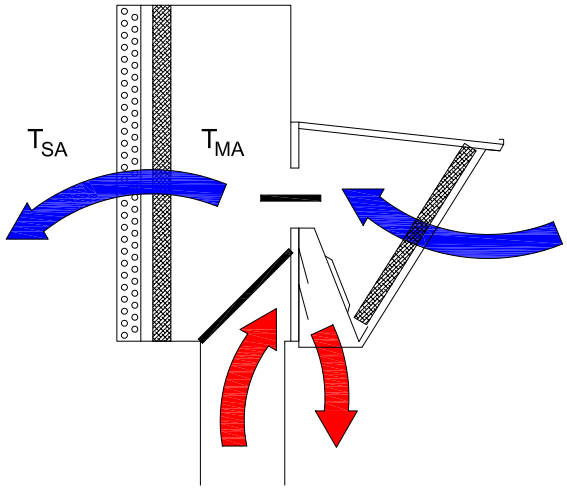

Figure 4.10. When the damper is in the fully-closed position and the RTU is in "fan-only" mode, the supply-air temperature, T_{sa}, and mixed-air temperature, T_{ma} should be nearly equal, after accounting for indoor fan temperature rise.

The predicted outdoor-air fraction can be compared with temperature-based estimations when the outdoor-air damper is fully-open as well. Neglecting return-air leakage through the return-air damper, performance residuals can be calculated between OAF_{oad} and the OAF estimations, OAF_{ma} and OAF_{sa},

$$r_8 = \left| \text{OAF}_{\text{oad}} - \text{OAF}_{\text{ma}} \right| , \tag{4.18}$$

$$r_9 = \left| \text{OAF}_{\text{oad}} - \text{OAF}_{\text{sa}} \right| . \tag{4.19}$$

Note that r_9 is only useful as a economizer diagnostic performance residual when the unit is "fan-only" mode, since $T_{\text{sa,adj}}$ can be used as a surrogate for the T_{ma} measurement.

The nine economizer diagnostic performance residuals described are summarized in Table 4.1. The sensor required to evaluate the performance residuals include the sensors required for the fault detection method: return-air temperature, T_{ra}, corrected outdoor-air temperature, $T_{\text{oa,corr}}$, corrected mixed-air temperature, $T_{\text{ma,corr}}$, and adjusted supply-air temperature, $T_{\text{sa,adj}}$. One additional outdoor-air measurement must be provided that can be trusted even when the installed outdoor-air temperature sensors has failed or is faulty, $T_{\text{oa,robust}}$.

Table 4.1.
Summary of economizer diagnosis performance residuals used to isolate outdoor-air damper and temperature sensor faults, along with the required damper position and sensors needed. These residuals are calculated during the active diagnosis procedure conducted in the RTU's "fan-only" mode.

Residual	Calculation	Damper Position	Sensor Requirement
r_1	$\lvert T_{\text{ra}} - T_{\text{ma}} \rvert$	Fully-Closed	T_{ra}, $T_{\text{ma,corr}}$
r_2	$\lvert T_{\text{sa}} - T_{\text{ma}} \rvert$	Fully-Closed	$T_{\text{ma,corr}}$, $T_{\text{sa,adj}}$
r_3	$\lvert \text{OAF}_{\text{oad}} - \text{OAF}_{\text{ma}} \rvert$	Fully-Closed	T_{ra}, $T_{\text{oa,corr}}$, $T_{\text{ma,corr}}$
r_4	$\lvert \text{OAF}_{\text{oad}} - \text{OAF}_{\text{sa}} \rvert$	Fully-Closed	T_{ra}, $T_{\text{oa,corr}}$, $T_{\text{sa,adj}}$
r_5	$\lvert T_{\text{oa}} - T_{\text{oa,robust}} \rvert$	Fully-Closed	$T_{\text{oa,corr}}$, $T_{\text{oa,robust}}$
r_6	$\lvert T_{\text{oa}} - T_{\text{ma}} \rvert$	Fully-Open	$T_{\text{oa,corr}}$, $T_{\text{ma,corr}}$
r_7	$\lvert T_{\text{sa}} - T_{\text{ma}} \rvert$	Fully-Open	$T_{\text{ma,corr}}$, $T_{\text{sa,adj}}$
r_8	$\lvert \text{OAF}_{\text{oad}} - \text{OAF}_{\text{ma}} \rvert$	Fully-Open	T_{ra}, $T_{\text{oa,corr}}$, $T_{\text{ma,corr}}$
r_9	$\lvert \text{OAF}_{\text{oad}} - \text{OAF}_{\text{sa}} \rvert$	Fully-Open	T_{ra}, $T_{\text{oa,corr}}$, $T_{\text{sa,adj}}$

The diagnosis method was designed to identify the outdoor-air damper faults and temperature sensor faults, listed in Table 4.2. An outdoor-air damper fault, more specifically,

is a fault which causes the damper to be stuck or in the wrong position. For stuck dampers, there is no requirement for the damper to be in a certain position in order to be detected, for instance, fully-closed, fully-open, or at minimum position. A stuck damper will be diagnosed regardless of the actual stuck position. A damper fault will also be diagnosed if the damper is partially modulating or modulating incorrectly.

Table 4.2.
Fault classes used by the Bayesian diagnosis classifier with descriptions of the corresponding faults.

Fault Class	Description
C_0	No Fault - Normal
C_1	Damper Fault
C_2	T_{ra} Fault
C_3	T_{ma} Fault
C_4	T_{oa} Fault
C_5	T_{sa} Fault

Temperature sensors faults can also be classified using the performance residuals defined in Table 4.1. The type of sensor fault identified using the fault diagnosis method are temperature bias faults and by extension, temperature sensor drift faults since a drift is just a bias growing over time. In mathematical terms the temperature sensor measurement, T_{meas} can be described as

$$T_{\text{meas}} = T_{\text{actual}} + e_{\text{normal}} \tag{4.20}$$

where T_{actual} is the actual temperature of fluid or surface being measured and e_{normal} is random error that is normally distributed. When the sensor is operating normally, the expected value of this error should be zero, $\mathbb{E}\left[e_{\text{normal}}\right] = 0$. When a bias is present, the measurement error will deviate from zero, $\mathbb{E}\left[|e_{\text{normal}}|\right] > 0$.

Using the performance residuals in Table 4.1, expected responses to different faults can be predicted. These expected responses are shown in Table 4.3 for each fault class. When faults are present in the system, the magnitudes of certain residuals should deviate from their corresponding normal values. In order for these responses to have value for fault diagnosis, each type of fault should affect the residuals differently. From Table 4.3, it is seen that each faults impacts the residuals uniquely.

Table 4.3.
Expected diagnosis performance residual responses for different economizer faults. Note that each of the responses is unique, revealing a "fault signature" corresponding to each class of fault.

	$r_1 = \lvert T_{\text{ra}} - T_{\text{ma}} \rvert$	$r_2 = \lvert T_{\text{sa}} - T_{\text{ma}} \rvert$	$r_3 = \lvert \text{OAF}_{\text{oad}} - \text{OAF}_{\text{ma}} \rvert$	$r_4 = \lvert \text{OAF}_{\text{oad}} - \text{OAF}_{\text{sa}} \rvert$	$r_5 = \lvert T_{\text{oa}} - T_{\text{oa,robust}} \rvert$	$r_6 = \lvert T_{\text{oa}} - T_{\text{ma}} \rvert$	$r_7 = \lvert T_{\text{sa}} - T_{\text{ma}} \rvert$	$r_8 = \lvert \text{OAF}_{\text{oad}} - \text{OAF}_{\text{ma}} \rvert$	$r_9 = \lvert \text{OAF}_{\text{oad}} - \text{OAF}_{\text{sa}} \rvert$
C_0 - No Fault									
C_1 - Damper Fault	↑		↑	↑		↑		↑	↑
C_2 - T_{ra} Fault	↑		↑	↑				↑	↑
C_3 - T_{ma} Fault	↑	↑	↑			↑	↑	↑	
C_4 - T_{oa} Fault			↑	↑	↑	↑		↑	↑
C_5 - T_{sa} Fault		↑		↑			↑		↑

In order to verify the predicted fault responses, the fault diagnosis residuals were calculated using experimental data. In order to simulate the the response to normal operation, data representing how the economizer would preform under normal conditions was used to calculate the residuals. This means r_{1-5} were calculated using only data with the damper

fully-closed in "fan-only" mode. Likewise, r_{6-9} were calculated under the same conditions with the damper at the fully-open position. Since not all the residuals share the same units, the standard score of the residuals were calculated in order to compare relative magnitudes of each. The standard score, z, of a residual x is

$$z = \frac{x - \mu}{\sigma}. \tag{4.21}$$

A convenient way to show graphical representations of numerical data and their quartiles can be accomplished using a box plot. An example box plot with the median, first and third quartiles (Q1 and Q3), and innerquartile range (IQR) labeled is shown in Figure 4.11. Additionally, the variability of the data outside the upper and lower quartiles is shown by lines extending from the box (called whiskers). The extents of the whiskers for the plot in Figure 4.11 are the lowest point still within 1.5 IQR of the lower quartile and the highest point still within 1.5 IQR of the upper quartile. Any data that is not between the extents of the whiskers is plotted with a $+$ symbol.

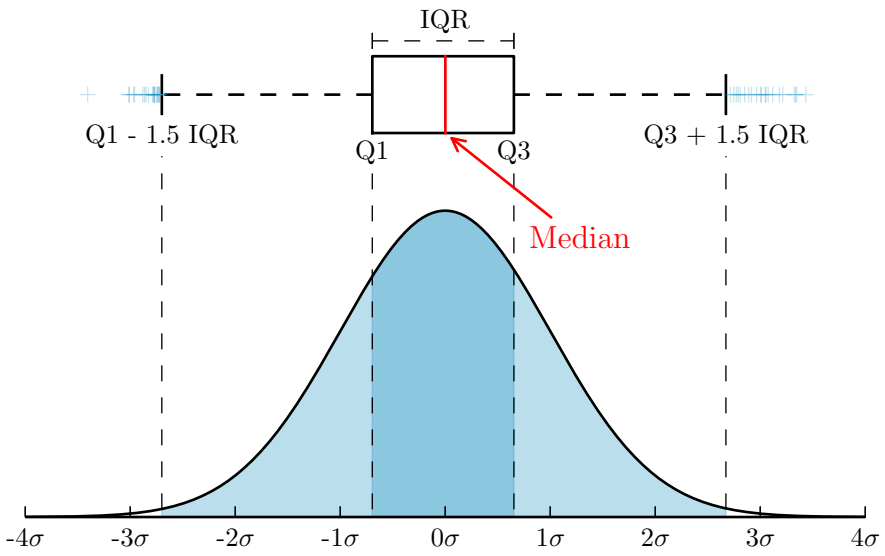

Figure 4.11. Box plot with labels indicating the lower and upper quartiles, inner quartile range, and median. Additionally the whiskers are labeled along with any outlier points. Also plotted is a normal probability density function for the data depicting the extents of the quartiles and whiskers.

Box plots of the absolute value of the standard score of each diagnosis residual is shown in Figure 4.12. These plots show the baseline values of the residuals when no faults are present. The box plot shows that there are no distinguishing feature between the residuals for normal performance data.

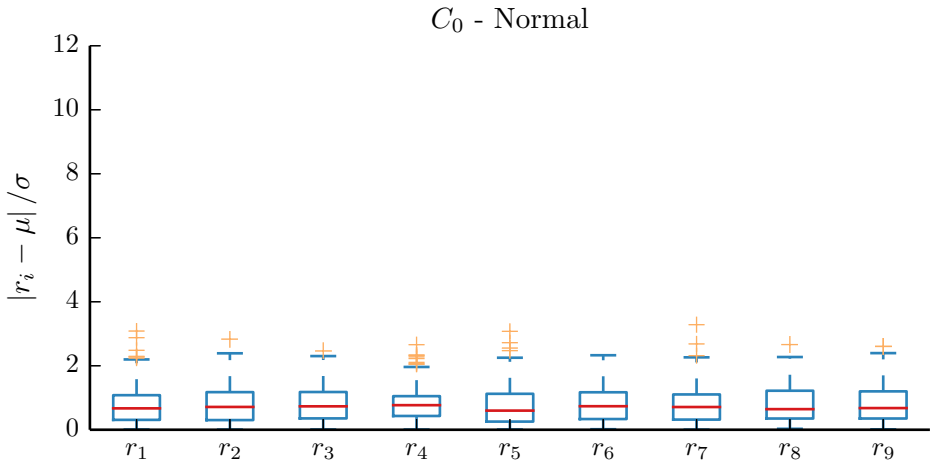

Figure 4.12. Fault diagnosis performance residual response to normal training data. The magnitude of these residuals are taken as the baseline performance of a correctly operating unit. When individual residuals deviate from this normal performance, a fault may be diagnosed.

Experimental data was used to simulate stuck damper faults by holding the damper position constant during the calculation of the residuals. For instance, to simulate a fault condition when the damper was stuck at $50\,\%$, residuals r_{1-5} were calculated using data when the damper was at the $50\,\%$ instead of $0\,\%$; r_{6-9} were calculated using the same data instead of $100\,\%$ damper position data. The absolute standard scores under these conditions are shown in Figure 4.13. The residuals calculated using the simulated stuck-damper fault data respond in the manner predicted in Table 4.3 for stuck damper faults. The box plots also show that the mean-values of the diagnosis residuals calculated using the faulty values deviate from the normal values significantly when affected by the fault.

Temperature sensor faults were simulated by applying uniformly distributed biases to individual temperature sensors within the data representing normal damper behavior. This

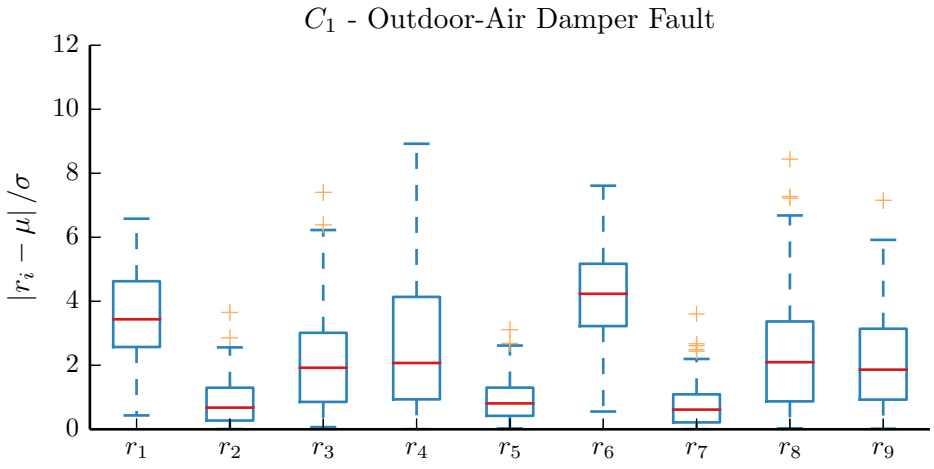

Figure 4.13. Fault diagnosis performance residual response to stuck damper training data. The response of the fault diagnoses residuals to a stuck damper matches the prediction.

bias was not applied during lab test, rather after data collection. This should not be a large issue since the RTU was manually controlled during testing, and thus temperature sensors errors would not affect operation. The biases applied ranged from $\pm 1.0\,°\text{C}$ to $\pm 3.0\,°\text{C}$ and were randomly distributed uniformly.

The resulting diagnosis residuals after applying return-air temperature sensor faults are shown in Figure 4.14. The response displayed by the these residuals matches that of the predicted response in Table 4.3. Additionally, the response shows that residuals calculated using sensors not requiring T_{ra} were unaffected by the fault. Similar behavior was observed for mixed-air temperature, outdoor-air temperature, and supply-air temperature faults shown in Figures 4.15, 4.16, and 4.17, respectively. It should also be noted that the average condenser-air inlet temperature was used for the robust outdoor-air temperature, $T_{\text{oa,rbst}}$. This was the most accurate temperature of the ambient outdoor room temperature that was controlled for each test.

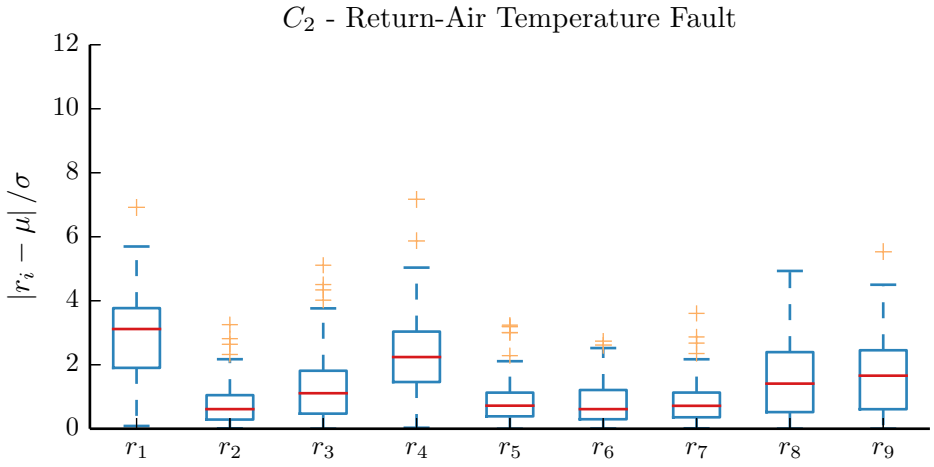

Figure 4.14. Fault diagnosis performance residual response to return-air temperature sensor fault training data. The response of the fault diagnoses residuals to this fault matches the prediction.

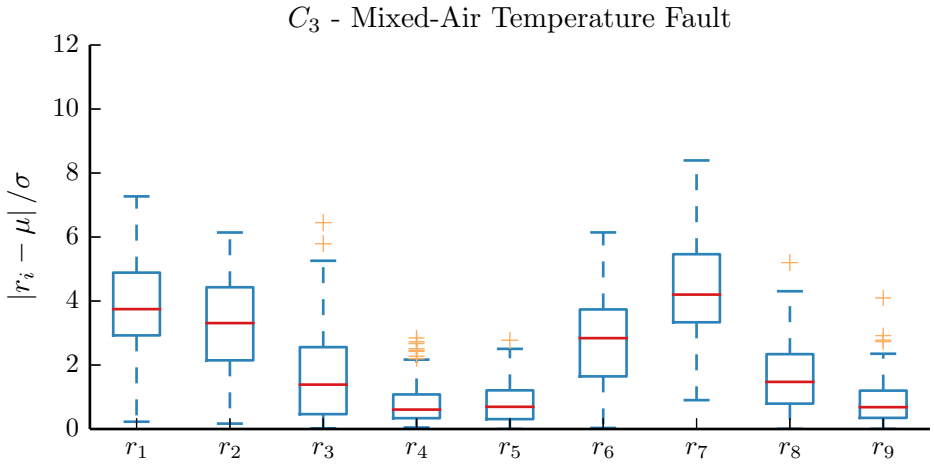

Figure 4.15. Fault diagnosis performance residual response to mixed-air temperature sensor fault training data. The response of the fault diagnoses residuals to this fault matches the prediction, described in Table 4.3.

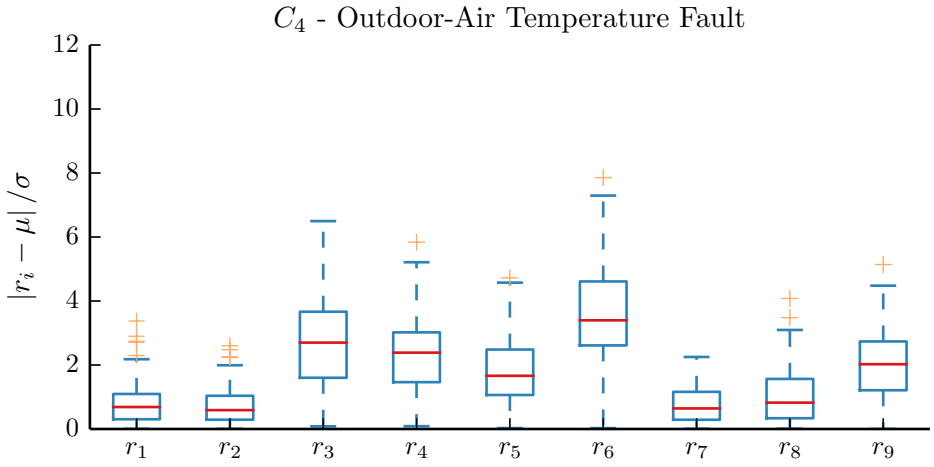

Figure 4.16. Fault diagnosis performance residual response to outdoor-air temperature sensor fault training data. The robust temperature sensor measurement used for this study was the average condenser-air inlet temperature. The response of the fault diagnoses residuals to this fault matches the prediction, described in Table 4.3.

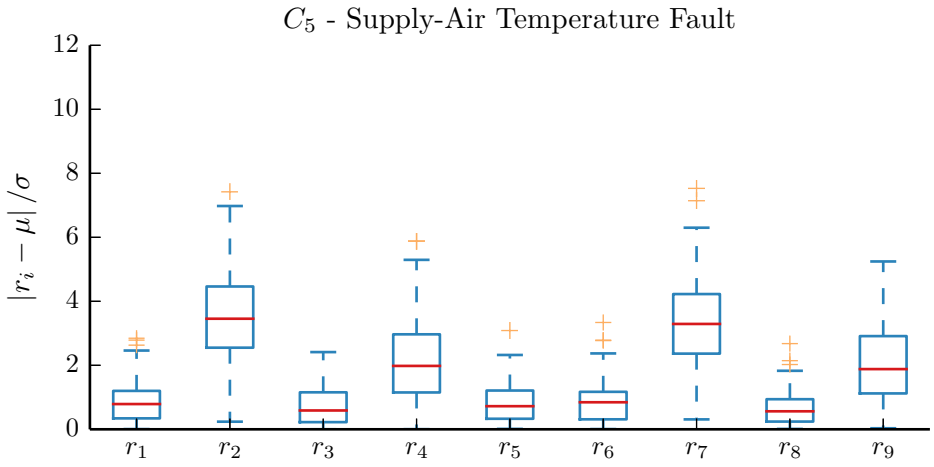

Figure 4.17. Fault diagnosis performance residual response to supply-air temperature sensor fault training data. The response of the fault diagnoses residuals to this fault matches the prediction, described in Table 4.3.

A conditional probability model $\mathbb{P}(\mathbf{C}|\mathbf{r})$ was used to classify the faults where $\mathbf{C}$ is the dependent class variable of the different possible diagnoses and $\mathbf{r}$ is the feature vector composed of the performance residuals r_i for $i = 1$ to 9. The conditional probability model outputs the probability of each diagnoses class given a a set of performance residuals. The probability model can expressed alternatively using Bayes' theorem,

$$\mathbb{P}(\mathbf{C}|\mathbf{r}) = \frac{\mathbb{P}(\mathbf{C})\,\mathbb{P}(\mathbf{r}|\mathbf{C})}{\mathbb{P}(\mathbf{r})}. \tag{4.22}$$

Using the experimental data, the conditional probability model of the residual vector given the fault class, $\mathbb{P}(\mathbf{r}|\mathbf{C})$ is learned. A prior probability model for the fault class, $\mathbb{P}(\mathbf{C})$ is specified *a-priori*. This is the probability of the different types of fault classes occurring before accounting for the evidence given by the residual vector. Since no expert knowledge was assumed for this application to predict the frequency different types of economizer faults, equal likelihood for each fault class was assumed for each fault.

4.3 Testing and Evaluation

4.3.1 Fault Detection Performance

The performance of the fault detector using the outdoor-air fraction residual, r_{ma}, determined by Equation (4.9) when the system is operating normally is shown in Figure 4.18. The detector was successfully able to avoid false alarms when tested using the experimental data since all the points were greater than the Bayes error threshold. Additionally, the fault detector showed little dependence on outdoor-air temperature, indicating that the fault detector is unlikely to declare false alarms in a real application.

The performance of the fault detector using the outdoor-air fraction residual, r_{sa}, determined by Equation (4.10) when the system is operating normally is shown in Figure 4.19. Similar performance was achieved using r_{sa} as the detector input compared with using r_{ma}. This is mostly on account of the correction models applied to T_{ma} and T_{sa}, which increases their respective accuracy. The detector successfully avoided most false alarms when tested using the experimental data, with only one point close to the threshold.

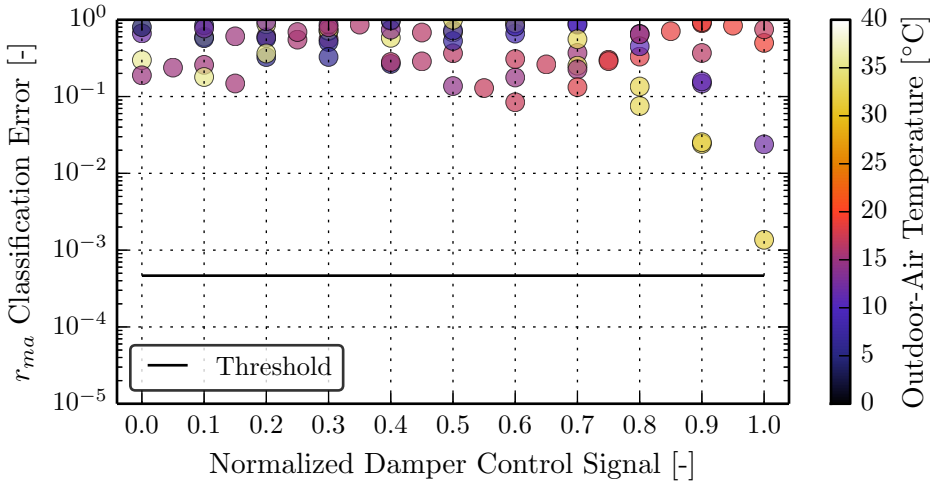

Figure 4.18. Fault detector performance under normal test conditions using the residual between OAF_{oad} and OAF_{ma}. Points less than the threshold are classified as false alarms.

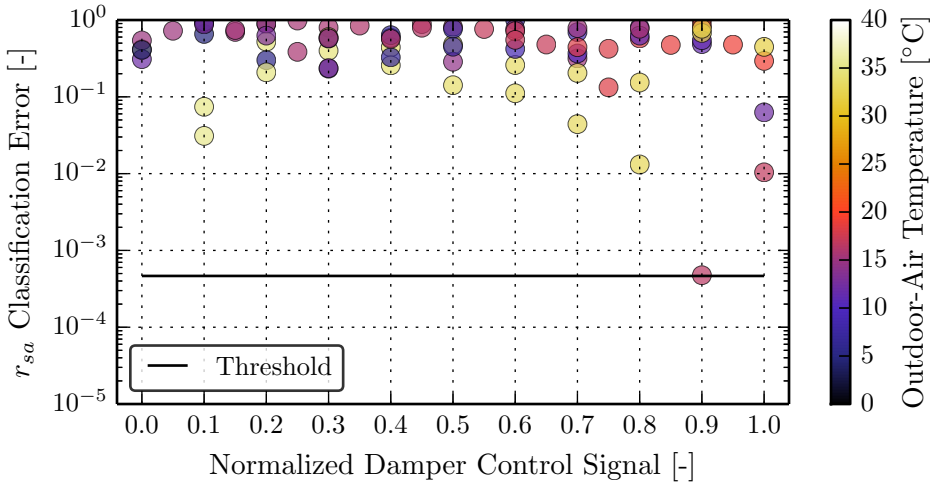

Figure 4.19. Fault detector performance under normal test conditions using the residual between OAF_{oad} and OAF_{sa}. Points less than the threshold are classified as false alarms.

In order to study the performance of the fault detector when the damper is stuck at different positions, faults were simulated using the experimental data by overriding the actual damper control signal. For instance, for stuck closed damper faults, the predicted outdoor-air fraction, OAF_{oad}, was evaluated using $0\,\%$ instead of the actual value used to collect the data. The fault detection performance for stuck closed dampers is shown in Figure 4.20 when using r_{ma} as the input. The same fault conditions were tested using r_{sa} as the input to the fault detector and similar performance was observed, shown in Figure 4.21. When the damper is expected to be at a position greater than $\gamma_{\text{oad}} = 30\,\%$, the fault detector was successfully able to detect a fault.

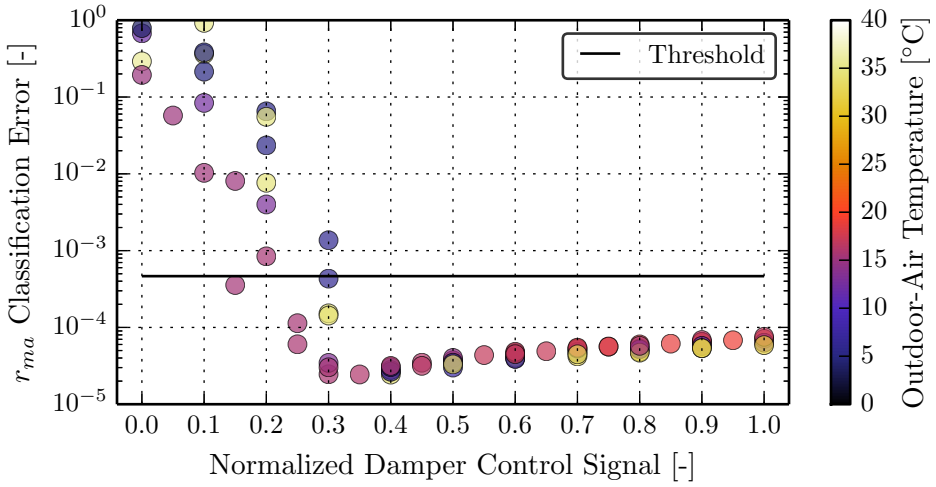

Figure 4.20. Fault detector performance using the residual between OAF_{oad} and OAF_{ma} when the damper is stuck closed, $\gamma_{\text{oad}} = 0\,\%$. Points less than the threshold are classified as correct. When the damper is expected to be at a position greater than $30\,\%$, the faults are all detected correctly.

Figures 4.20 and 4.21 illustrate a disadvantage of passive fault detection. Passive methods are unable to detect faults when the fault is masked by the current operation. In the cases above, the damper fault was unable to be detected when the damper was closed since the damper was suppose to be closed. More correctly, the fault under these conditions is not detected because under the conditions, they are not truly faults. Additionally, these faults

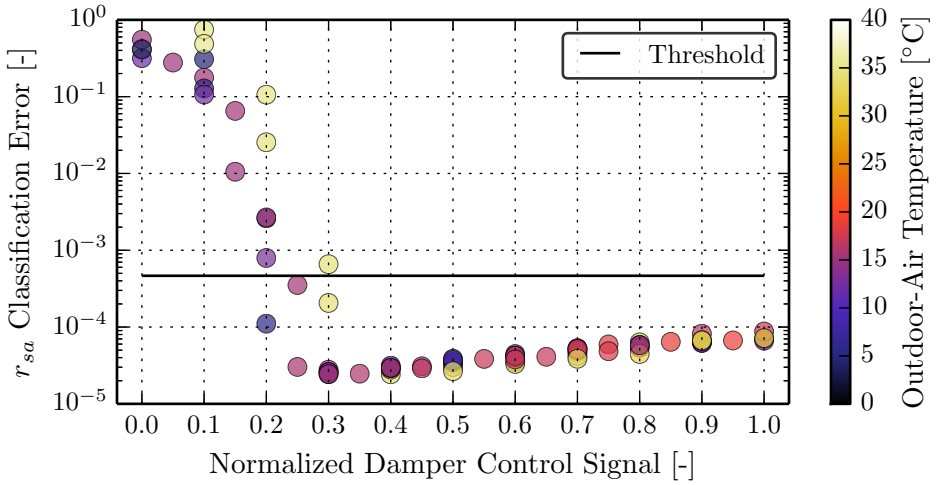

Figure 4.21. Fault detector performance using the residual between OAF_{oad} and OAF_{sa} when the damper is stuck closed, $\gamma_{\text{oad}} = 0\,\%$. Points less than the threshold are classified as correct. When the damper is expected to be at a position greater than $30\,\%$, the faults are all detected correctly.

cause no increase in energy consumption or compressor run-time. In order to overcome this limitation, an active detection method could be employed which is able to force the system into desired conditions.

The fault detection performance for stuck open dampers is shown in Figure 4.22 when using r_{ma} as the input. The same fault condition were tested using r_{sa} as the input to the fault detector and similar performance was observed, shown in Figure 4.23. Nearly all possible faults were detected when the damper was expected to be at positions less than $\gamma_{\text{oad}} = 80\,\%$. The limitation of this method is observed once again, when the damper is stuck in positions greater than $\gamma_{\text{oad}} = 80\,\%$.

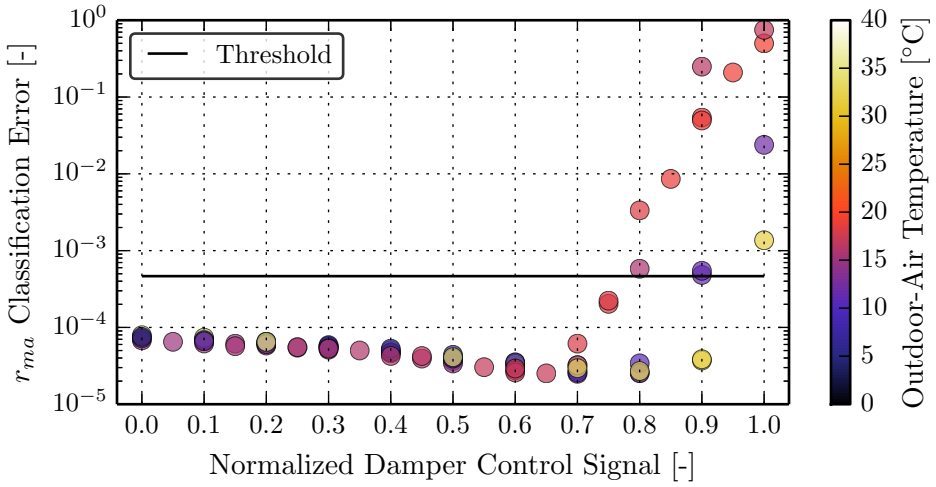

Figure 4.22. Fault detector performance using the residual between OAF_{oad} and OAF_{ma} when the damper is stuck open, $\gamma_{\text{oad}} = 100\,\%$. Points less than the threshold are classified as correct. When the damper is expected to be at a position less than $80\,\%$, the faults are all detected correctly.

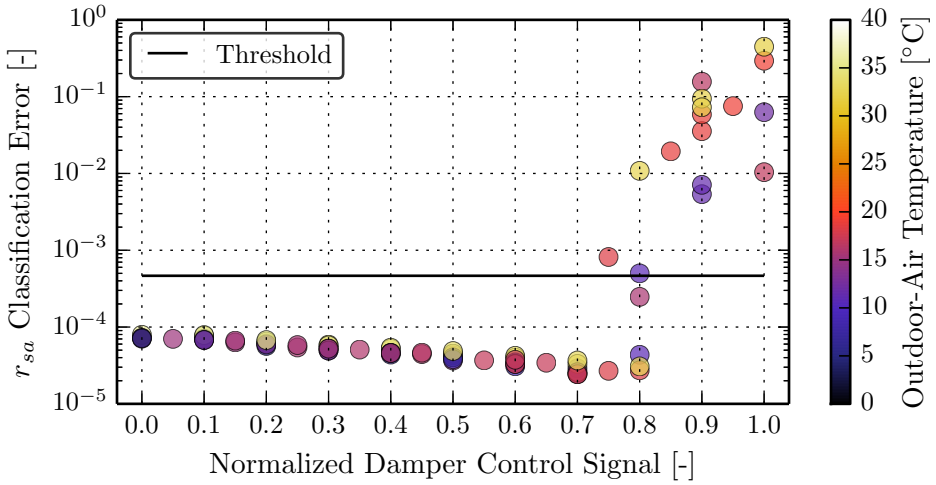

Figure 4.23. Fault detector performance using the residual between OAF_{oad} and OAF_{sa} when the damper is stuck open, $\gamma_{\text{oad}} = 100\,\%$. Points less than the threshold are classified as correct. When the damper is expected to be at a position less than $80\,\%$, nearly all the possible faults are detected.

4.3.2 Fault Diagnosis Performance

Stuck Damper Faults

Using experimental data, the performance of diagnosing different faults was examined. Stuck damper faults were tested using the same method as was used in fault detection evaluation. Experimental data was collected under different outdoor-air temperature conditions and damper positions. The active diagnostics method was simulated by not modulating the damper to fully-closed and fully-open positions in order to also simulate the fault. For instance, if the damper was meant to be stuck at $50\,\%$ open, the performance residuals r_{1-5} were calculated with the damper at $50\,\%$ instead of $0\,\%$. Furthermore, residuals r_{6-9} were calculated when the damper was at the 50% position as well. This simulates a stuck damper, unable to modulate from its current position.

The posterior fault probability of each fault class is shown as a function of different stuck damper positions in Figure 4.24. The diagnosis method showed a an affinity for diagnosing stuck damper faults well regardless of the damper positions. The posterior probability of a damper fault, a measure of confidence in the decision is very close to 1 for most of the damper positions test. This probability is degraded when the damper is stuck between the $60\,\%$ to $70\,\%$ positions, but still remains above $90\,\%$ confident in the fault. This slight degradation is most likely due to the effect of hysteresis in damper position detailed in Figure 3.15, since this effect was most prevalent near these damper positions. One test when the damper position was stuck at $80\,\%$ showed relatively poor performance. This again was mostly likely the result of damper hysteresis on the mixed-air temperature, shown in Figure 3.14. Even so, the Bayesian classifier used to diagnose faults still predicted the stuck damper as the most likely cause of the fault for this case.

Another positive attribute of the fault diagnosis performance shown by Figure 4.24 is the very low probability of misdiagnosing the system as being normal for stuck damper faults. Because of this, the likelihood of a damper fault unknowingly persisting in the system for an extended period of time is very low after the active diagnostics procedure is performed. As previously stated, the fault may go undetected by the passive fault detection method if it

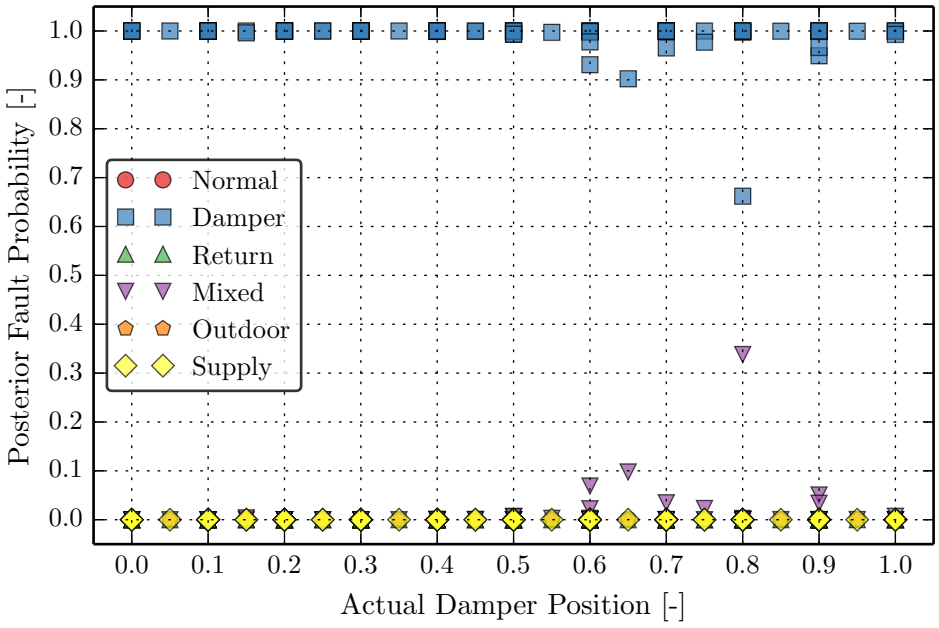

Figure 4.24. Stuck outdoor-air damper fault diagnosis performance. The fault diagnosis method showed good diagnostic performance for the range of possible stuck damper positions.

is stuck in the same position being controlled by the system. However, during this time the fault has no impact on the RTU's performance, so detection and diagnosing is not necessary. When the economizer controller eventually commands the damper to modulate to another position, the fault detector and diagnostic tool is able to identify the fault before causing a larger energy impact.

Return-Air Temperature Sensor Faults

It is relatively difficult to implement sensor faults into a system repeatably. Because of this, temperature sensor faults were injected into the experimental data at increasing severity after collection. Thus, experimental data was collected when all the temperature sensors were working properly under different ambient and operational conditions and used to build system models and for fault detection and diagnosis false alarm performance. Once

faults were implemented into the data, the modified experimental data was used to assess diagnostic performance.

Return-air sensor faults were injected into the experimental data by incrementing the magnitude of the error component of the sensor using Equation (4.20). The diagnosis method's performance for diagnosing return-air temperature sensor bias faults ranging from $-3.0\,°C$ to $3.0\,°C$ is shown in Figure 4.25. The figure shows increasing probability in return-air temperature sensor faults as the magnitude of the sensor bias increases. Additionally, the diagnosis tool is able to diagnose normal behavior when no temperature sensor bias is added to the data. For return-air temperature sensor biases greater than $\pm 1.0\,°C$, the diagnosis classifier returned probabilities nearly equal to 1. Lesser performance was achieved for faults smaller than $\pm 1.0\,°C$, decreasing towards zero as the biases approached $0.0\,°C$.

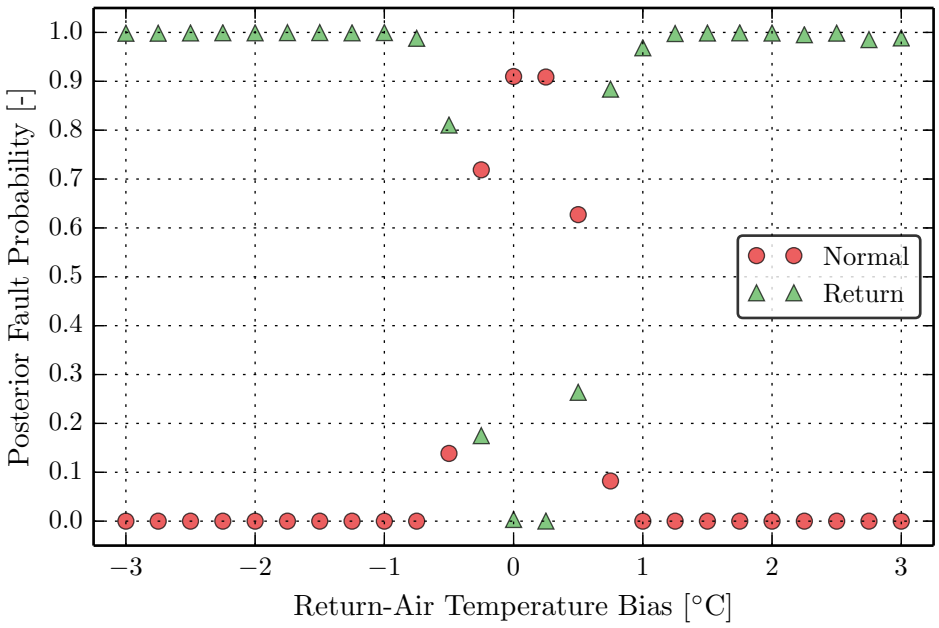

Figure 4.25. Return-air temperature sensor fault diagnosis performance. For increasing severity of return-air temperature sensor bias faults, the diagnosis method shows improving performance. When the bias exceeds $\pm 1.0\,°C$, the diagnostic method diagnoses the fault with a probability close to 1.

Mixed-Air Temperature Sensor Faults

The diagnostic classifier performance identifying mixed-air temperature bias faults is shown in Figure 4.26 for faults ranging between $\pm 3.0\,^{\circ}\mathrm{C}$. Faults greater then $1.0\,^{\circ}\mathrm{C}$ are detected with near certainty. Lesser performance is observed for faults with smaller magnitude, however these faults have small impact, especially considering the rated accuracy of the thermocouples used were $\pm 1.0\,^{\circ}\mathrm{C}$. The plot also shows that despite the mixed-air temperature sensors inaccuracy due to nonuniform flow and temperature stratification, the Bayesian classifier does a good job of distinguishing between normal operation and faulty operation.

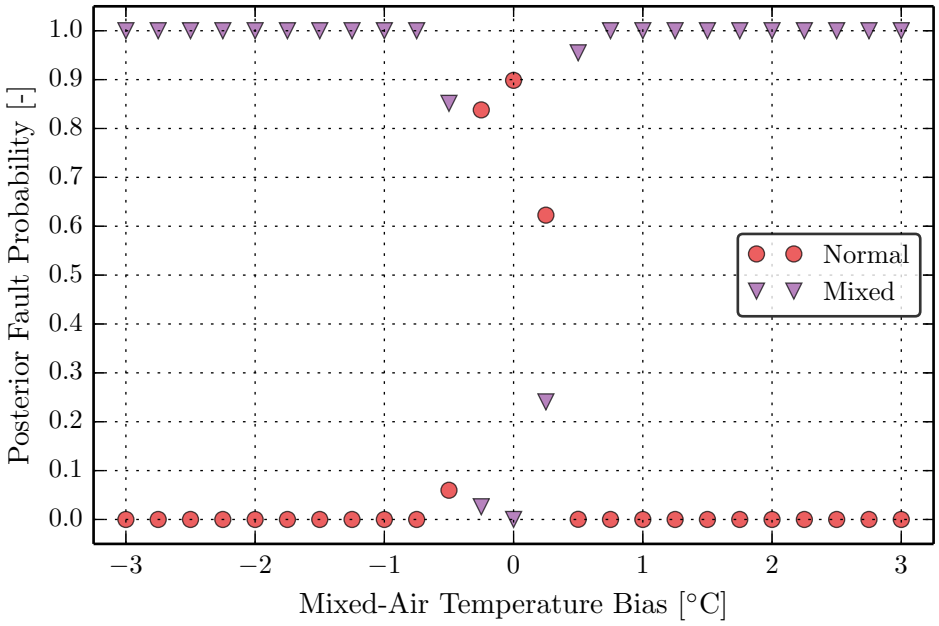

Figure 4.26. Diagnosis performance when a mixed-air temperature sensor fault is present in the system. For increasing severity of mixed-air temperature sensor bias faults, the diagnosis method shows improving performance. When the bias exceeds $\pm 1.0\,^{\circ}\mathrm{C}$, the diagnostic method diagnoses the fault with a probability close to 1.

Outdoor-Air Temperature Sensor Faults

An important sensor used for economizer operation is the outdoor-air temperature sensor since the mode of operation is determined using it. Therefore, diagnosing when this temperature has deviated from calibration is an important feature of the economizer FDD method. This diagnostic performance is shown in Figure 4.27 for varying degrees of outdoor-air temperature sensor error biases. Like the previous sensor faults examined, the diagnosis classifier is able to identify outdoor-air temperature sensor faults consistently for faults exceeding $\pm 1.0\,°\text{C}$ in bias. For trivial faults, or in the case of $0.0\,\%$ bias, normal conditions, the classifier determines the system is normal with higher probabilities.

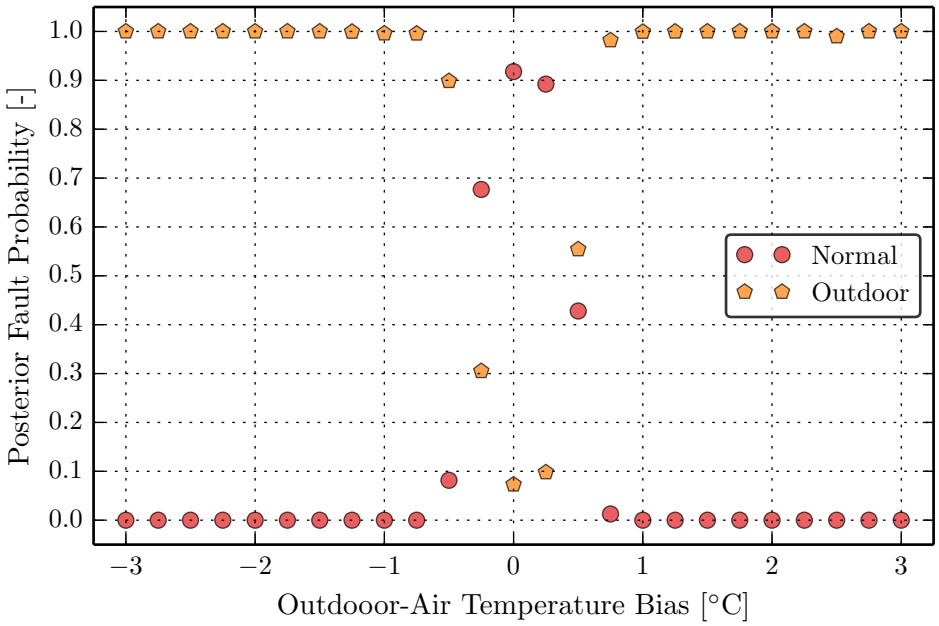

Figure 4.27. Diagnosis performance when an outdoor-air temperature sensor fault is present in the system. For increasing severity of outdoor-air temperature sensor bias faults, the diagnosis method shows improved performance. When the bias exceeds $\pm 1.0\,°\text{C}$, the diagnostic method diagnoses the fault with a probability close to 1.

It should be noted once again that for this evaluation, the true outdoor-air temperature was used as the $T_{\text{oa,rbst}}$. Because of this, actual outdoor-air temperature sensor fault diagnosis

performance could be degraded in field settings where a less reliable measurement of the outdoor-air temperature is used. Performance could be significantly worse if the "robust" outdoor-air temperature measurement was faulty, since the classifier was designed under the assumption that this measurement could be obtained reliably.

Supply-Air Temperature Sensor Faults

The supply-air temperature sensor is used within the economizer FDD implementation as a more robust means of estimating the outdoor-air fraction when the RTU operates in "Fan-Only" mode. Therefore, identifying when this temperature is not valid is important in order to ensure a robust economizer diagnostic tool. Different supply-air temperature sensor faults are shown in Figure 4.28 along with the FDD ability to isolate them. The diagnosis classifier was able to diagnose faults as small as ± 0.75 °C with near certainty. This is better performance than the other temperature sensor faults since the supply-air stream is generally well mixed in the RTU and the indoor fan temperature rise adjustment is accurate.

4.4 Summary of Results

The passive fault detection method utilizes normal performance models developed using laboratory test data to statistically determine when current economizer performance has become faulty. A statistical classifier has been applied to a residual between a outdoor-air fraction prediction and an estimation based on ventilation temperature sensors. The method can be performed during any operational mode of the RTU, however, a steady-state filter is used to remove transient measurements that may lead to false alarms. When using a suitable fault detection threshold, the method was able to eliminate false alarms for all the normal experimental data tested.

The fault detector was able to identify stuck damper faults in all the tests examined whenever the difference between the actual position and expected damper position became greater than $30\,\%$. For deviations less than this, the fault detector was unable to identify faults with consistency. This result shows a potential limitation of passive fault detection

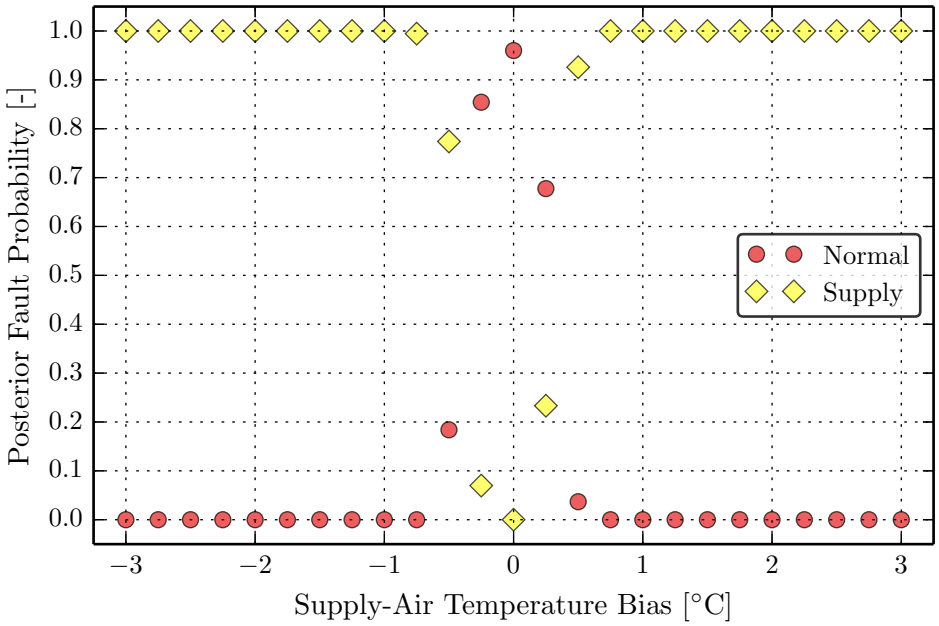

Figure 4.28. Diagnosis performance when an supply-air temperature sensor fault is present in the system. For increasing severity of supply-air temperature sensor bias faults, the diagnosis method shows improved performance. When the bias exceeds $\pm 1.0\,°C$, the diagnostic method diagnoses the fault with a probability close to 1.

since faults cannot be detected when the damper is stuck in the correct position. This fault has a minimal energy penalty, so these situations are not critical from a maintenance perspective.

An active fault diagnosis method was proposed that utilizes control of the outdoor-air damper in order to force the system into operations that provide measurement redundancy. These positions are when the damper is fully-closed and full-open. Nine performance residuals are calculated that are sensitive to different economizer faults. Moreover, each fault has a unique impact on the performance residuals as a whole. These fault signatures became the basis of a statistical fault diagnosis classifier that was trained using laboratory data.

A summary of the overall diagnostic performance for different economizer faults is illustrated in Figure 4.29 and Table 4.4. The false alarm rate of the fault detection method was approximately $1\,\%$ when normal performance experimental data was analyzed. The misdiagnoses rate of the diagnosis classifier for normal data was approximately $4.9\,\%$. When taken together, the overall false alarm rate of the AFDD tool was approximately $0.05\,\%$. This low false alarm rate can be attributed to the accuracy of the temperature sensor correction and outdoor-air fraction models that can be attained when using experimentally obtained training data for an individual RTU. In $4\,\%$ of these cases, an outdoor-air temperature sensor bias was diagnosed, a negative result. The most likely cause for these diagnoses are the impact of return-air recirculation on the outdoor-air temperature sensor error. While the model performed adequately for fault detection, a better model incorporating a virtual outdoor-air flow rate sensor could decrease this false alarm rate. Furthermore, the magnitude of return-air recirculation could be impacted by wind at the rooftop leading to more potential errors.

Stuck damper faults were identified over $93\,\%$ of the time when using the active diagnosis method. From Figure 4.24, the performance when the damper was stuck between $60\,\%$ to $80\,\%$ was slightly degraded. This is most likely the result of damper position hysteresis which causes a larger error on the outdoor-air fraction and mixed-air temperature sensor correction models. For this reason, there is $2.2\,\%$ misclassification error for mixed-air temperature sensor faults when the damper is stuck.

In order to evaluate the performance of the temperature sensor bias faults, a fault threshold was defined. For biases greater than $1.0\,^{\circ}$C, the temperature sensor affected by the bias was labeled as faulty. For biases less than the $1.0\,^{\circ}$C threshold, the sensors were labeled as normal. Using this convention, the diagnosis method was able to detect $97.6\,\%$ of the return-air temperature sensor faults. A remaining $1.7\,\%$ of the test cases were classified as damper faults. This is most-likely the effect of predicted fault signatures being very similar to each other, only differing by the response of residual r_6, shown by Table 4.3.

The remaining faults were classified with at least $91\,\%$ accuracy. Over $94.5\,\%$ of the mixed-air temperature sensors faults were identified. About $3\,\%$ and $2\,\%$ of the remaining

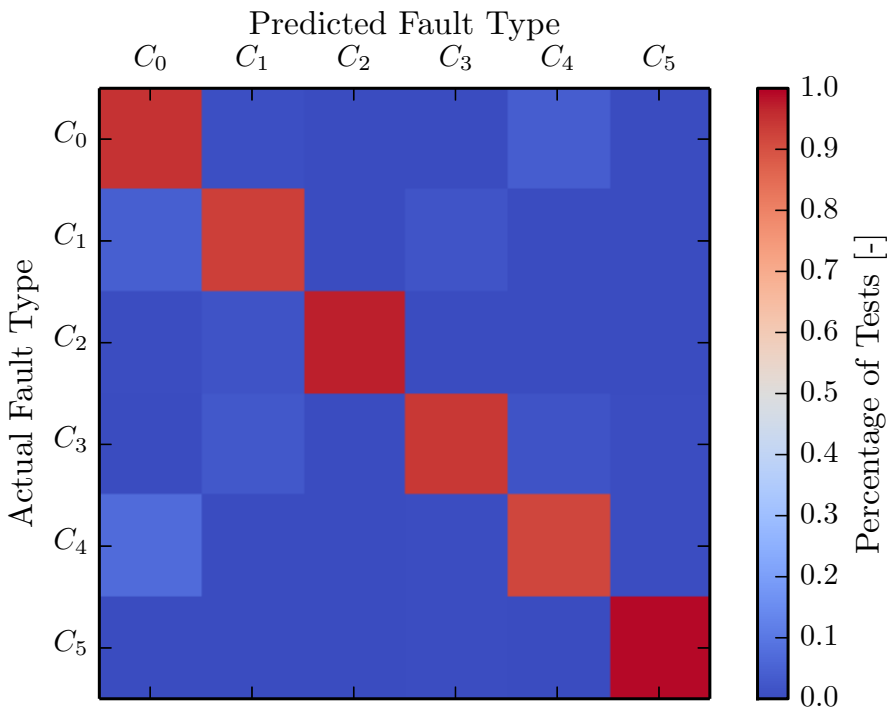

Figure 4.29. Fault diagnosis performance for different types of faults studied using experimental data. Temperature sensor faults were classified as active when the bias was greater than $\pm 1.0\,^{\circ}\mathrm{C}$ for evaluation. Faults with biases less than $\pm 1.0\,^{\circ}\mathrm{C}$ were labeled as normal.

diagnoses were for stuck damper faults and outdoor-air temperature sensor faults respectively. The poorest fault classification was for outdoor-air temperature sensor faults, with a diagnosis of accuracy of $91.8\,\%$. The remaining diagnoses were for the normal class, with approximately $7.4\,\%$ of the test cases. Nearly all of the supply-air temperature sensor faults were diagnosed correctly, $99.4\,\%$. The classifier is most effective at diagnosing this fault due to the relatively good supply-air temperature measurement accuracy, since the effects of thermal stratification or return-air recirculation have no effect on this sensor.

Multiple simultaneous economizer faults were not considered in this research and the proposed classifier is not predicted to perform well under these conditions. An assumption of independence was used when formulating the classifier and in the presence of multiple

Table 4.4.
Diagnosis prediction accuracy for different types of economizer faults, including stuck damper and biased temperature sensor faults.

	Predicted Fault Classes					
	C_0	C_1	C_2	C_3	C_4	C_5
C_0	0.951	0.008	0.001	0.000	0.040	0.000
C_1	0.045	0.932	0.001	0.022	0.000	0.000
C_2	0.005	0.017	0.976	0.002	0.002	0.000
C_3	0.003	0.030	0.000	0.945	0.018	0.004
C_4	0.074	0.000	0.000	0.004	0.918	0.004
C_5	0.000	0.000	0.000	0.005	0.001	0.994

faults would cause the fault residuals to respond in ways not predicted. It may be possible to produce more system measurement by installing humidity sensors at different locations in the system and incorporate these measurements into the classifier design. Another solution is to perform active diagnosis at regular intervals in order to diagnose system faults before additional faults are introduced.

5. ECONOMIZER FAULT PERFORMANCE IMPACT

5.1 Damper Fault Impact on RTU Cycle

In the presence of a damper fault, the RTU vapor-compression cycle is affected due to the changed mixed-air condition. Because of this, the evaporator saturation temperature increases or decreases depending on this new mixed-air condition. When the damper is stuck open and the outdoor-air is warmer and moister, the evaporator saturation temperature increases. This affect is shown under two different outdoor-air conditions in Figures 5.1 and 5.2. Additionally, it can be seen from the Figures that as the difference between the return-air and outdoor-air conditions become larger, the difference in normal and faulty evaporation temperatures becomes larger as well.

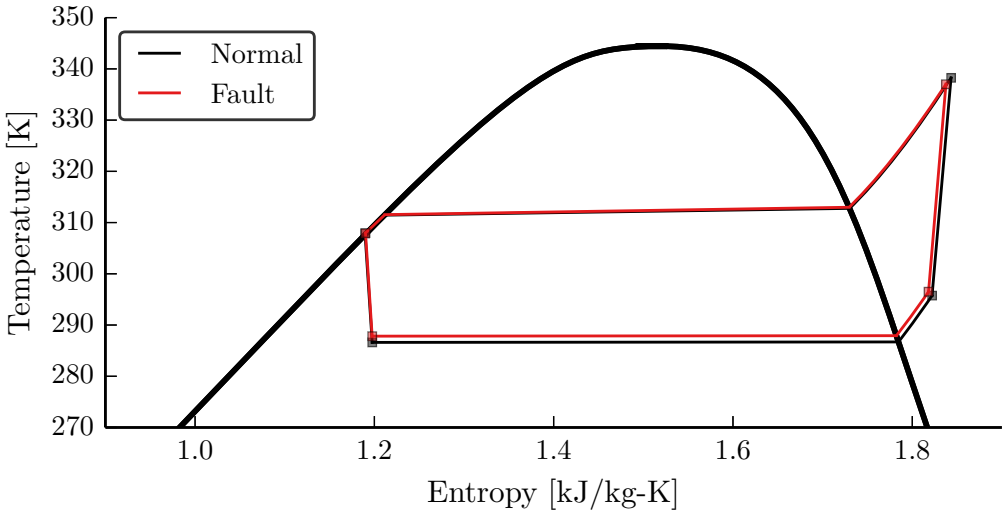

Figure 5.1. Effect of damper position on RTU capacity and COP under 37.78 °C, 50 % outdoor-air temperature and relative humidity, while maintaining 26.00 °C, 50 % return-air temperature and relative humidity.

It should also be noticed that the condenser saturation temperature is only slightly affected by the faulty damper. This is because the damper has a small impact on the compressor suction pressure, and thus a slight impact on compressor discharge pressure. Because of this, compressor work is decreased since the pressure ratio has decreased. In addition, greater cooling capacity is achieved at the higher evaporation temperature. The combined impact of these effects is a higher efficiency than would be normally expected under the set of outdoor-air and return-air conditions.

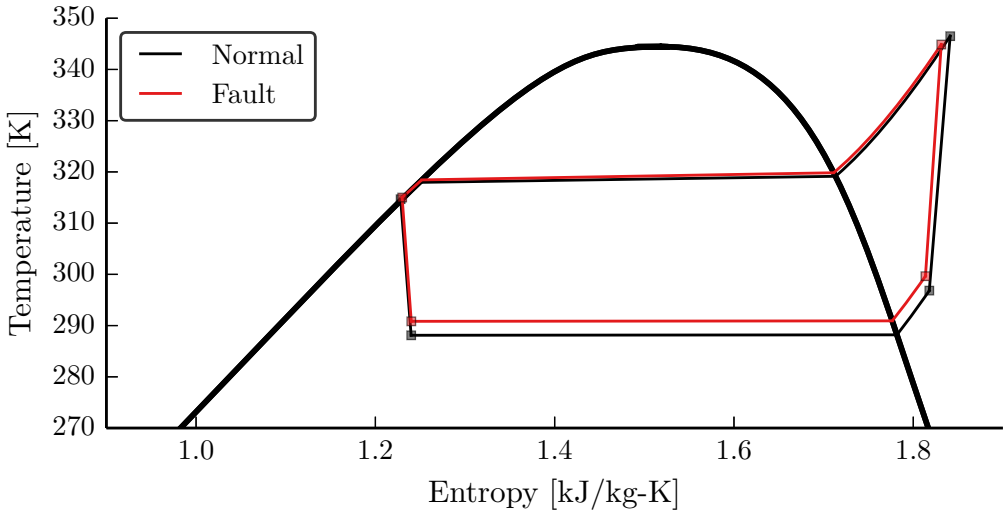

Figure 5.2. Effect of damper position on RTU capacity and COP under 37.78 °C, 50 % outdoor-air temperature and relative humidity, while maintaining 26.00 °C, 50 % return-air temperature and relative humidity.

When the ambient outdoor-air is cooler and more dry, the opposite effects can be noticed. While the condensing temperature remains approximately unchanged, the evaporating temperature decreases. This causes a larger pressure ratio across the compressor and thus, more required compressor work. At the lower evaporating temperature, a decrease in cooling capacity will be noticed, all leading to a lower efficiency.

An investigation of the quantifiable effects of stuck outdoor-air dampers on cooling capacity, compressor work, and cycle efficiency will be discussed in the following sections

when the outdoor-air is warmer and more moist than the return-air condition. Three outdoor-air test conditions were controlled while maintaining the return-air conditions at $26.00\,°C$ and $50\,\%$ relative humidity. These conditions are described in Table 5.1.

Table 5.1.
Outdoor-air temperature and relative humidity conditions for damper fault impact tests, along with the damper positions for each test.

T_{oa} [°C]	ϕ_{oa} [%]	Normal γ_{oad} [-]	Fault γ_{oad} [-]
31.50	40	10	30, 50, 70
31.50	50	20	40, 60, 80
37.78	50	0	33, 50, 67, 100

For each set of conditions, the outdoor-air damper was controlled to different positions in order to quantify the effect of the damper position on the fault impacts. Per each test condition, a normal damper position was designated as the baseline operation from which the relative impacts were calculated. In order to capture the possibility of different minimum outdoor-air fraction requirements, these normal positions varied from $0\,\%$ to $20\,\%$. However between this range, the outdoor-air fraction changes only slightly due to the damper characteristics shown by Figure 2.8. Because of this, tests conducted with a higher normal damper position will have smaller relative impacts for the same faulty position since the normal outdoor-air fraction is greater for these cases.

5.1.1 Cooling Capacity Impact

In Chapter 3, the damper characteristics were discussed. How the damper position influenced outdoor-air fraction was examined in detail and a model was made so that it could be used for fault detection. Figure 5.3 shows outdoor-air fraction as a function of the normalized damper position for each of the test cases described in Table 5.1. In order to

describe the relative increase in outdoor-air fraction caused by the faulty damper position, the outdoor-air fraction ratio, r_{OAF}, was defined:

$$r_{\text{OAF}} = \frac{\text{OAF}_{\text{actual}}}{\text{OAF}_{\text{normal}}} \tag{5.1}$$

where $\text{OAF}_{\text{actual}}$ is the actual or current outdoor-air fraction estimate and $\text{OAF}_{\text{normal}}$ is the normal or expected outdoor-air fraction under the current conditions. For the fault impact tests, three damper positions close to being closed were taken as the normal conditions, described in Table 5.1. The remaining test cases corresponded to faulty damper positions of increasing severity.

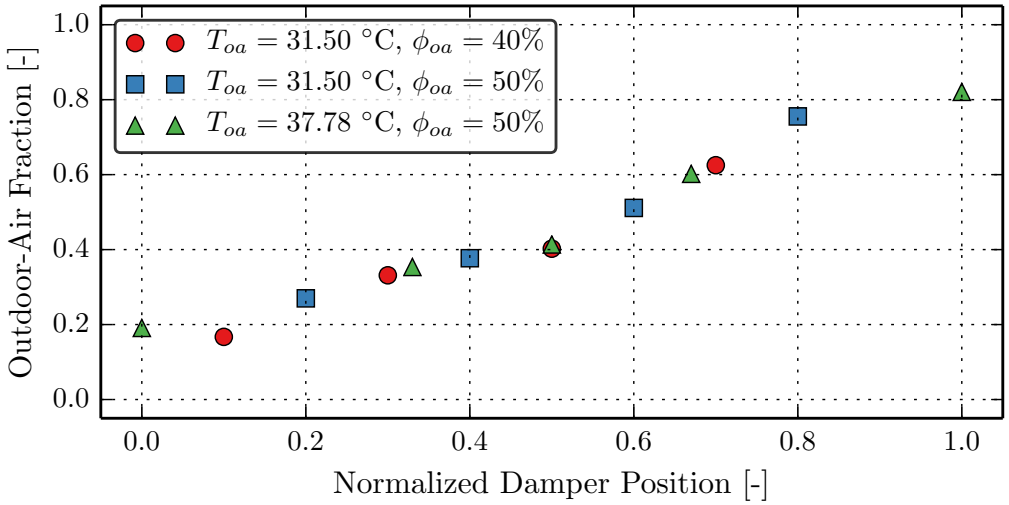

Figure 5.3. Outdoor-air fraction produced by various outdoor-air damper positions under they different test conditions used for damper fault impact analysis.

The outdoor-air fraction ratio is calculated for each test case in Figure 5.4. The r_{OAF} increases as the damper position increases within each test condition. The difference in rates of increase between test conditions is caused by the differences in outdoor-air fraction at the normal conditions. For instance, r_{OAF} are the least for Test Condition 2 because the normal outdoor-air fraction under these conditions was the greatest; each case has a different baseline.

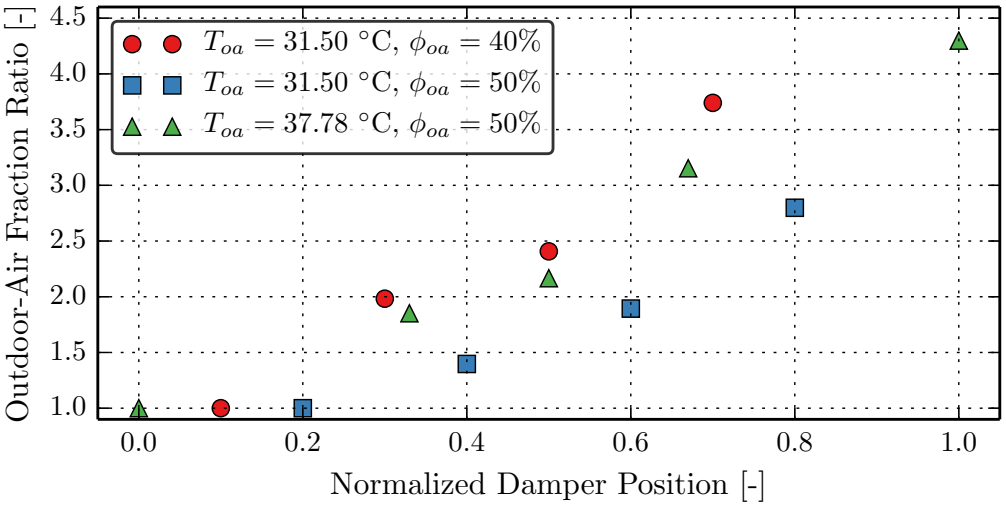

Figure 5.4. Outdoor-air fraction ratio as a function of outdoor-air damper position. The ratio is the equivalent to the relative increase in outdoor-air supplied to the RTU caused by the incorrect damper position.

The result of the increased fraction of outdoor-air entering the the RTU mixing box, and thus the evaporator, is an increase in cooling capacity because the outdoor-air enthalpy is greater than the return-air enthalpy. When the outdoor-air enthalpy is less than the return-air enthalpy, the effect of increased outdoor-air fraction is a decrease in cooling capacity. A cooling capacity ratio, r_{capacity}, is defined in order to compare the relative change in cooling capacity under different outdoor-air conditions and damper positions,

$$r_{\text{capacity}} = \frac{\dot{Q}_{\text{evap,actual}}}{\dot{Q}_{\text{evap,normal}}} \tag{5.2}$$

where $\dot{Q}_{\text{evap,actual}}$ is the measured cooling capacity and $\dot{Q}_{\text{evap,normal}}$ is the normal cooling capacity if the damper was in its correct position. The effects of additional outdoor-air supplied to the RTU on cooling capacity is shown in Figure 5.5. As the amount of warmer, more moist outdoor-air is supplied, the cooling capacity increases. These impacts are more pronounced for increasing outdoor-air enthalpy.

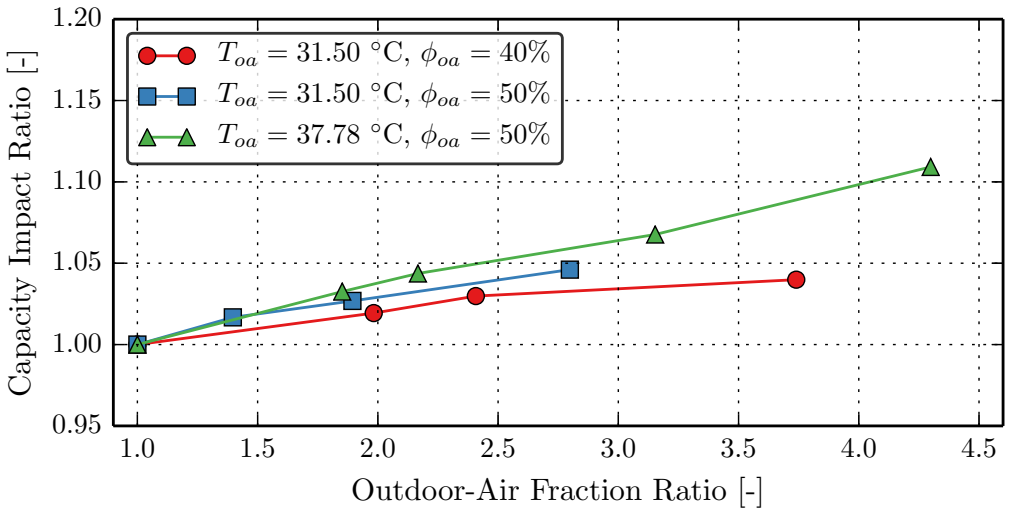

Figure 5.5. Increased cooling capacity caused by stuck dampers at different positions and under different outdoor-air conditions.

In addition to the capacity impact, the stuck damper causes the mass flow rate of refrigerant through the RTU to increases due to the higher density associated with higher

evaporating temperature. The expansion valve becomes more open to balance this flow at a reduced pressure differential and to maintain the superheat entering the compressor. The measured mass flow rate of refrigerant is shown in Figure 5.6. These trends would continue until the expansion valve reaches its maximum under very warm outdoor-air conditions or when the system is undercharged.

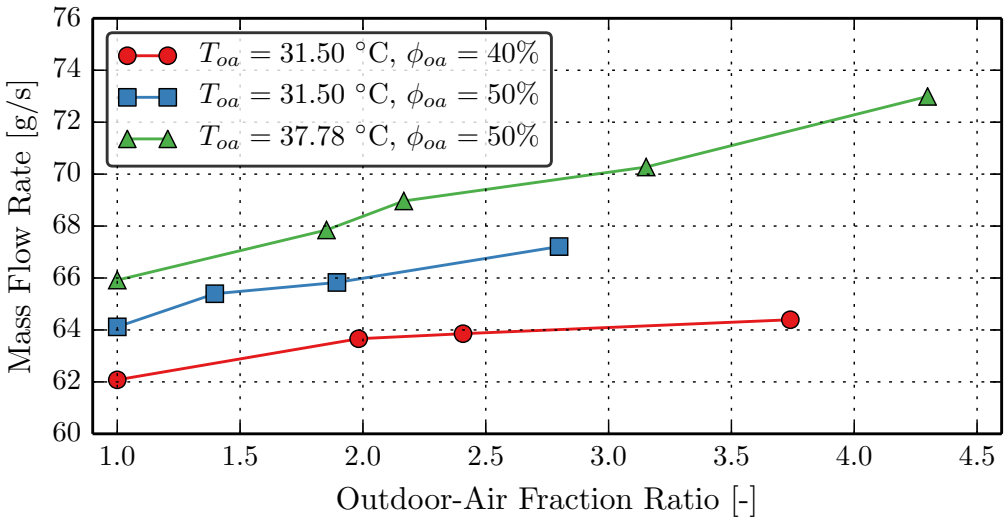

Figure 5.6. Refrigerant mass flow rate under different outdoor-air damper positions and outdoor-air conditions.

5.1.2 Compressor Power Impact

Since the condensing temperature and pressure are unchanged by the damper fault, the increasing evaporating pressure causes a change in required compressor work. The compressor power ratio, $r_{\dot{W}}$, is defined as the ratio of actual compressor power, $\dot{W}_{\text{comp,actual}}$, to the normal compressor power, $\dot{W}_{\text{comp,normal}}$:

$$r_{\dot{W}} = \frac{\dot{W}_{\text{comp,actual}}}{\dot{W}_{\text{comp,normal}}}. \tag{5.3}$$

The compressor power ratio is calculated for each test condition in Figure 5.7. The largest decrease in compressor power observed was less than $1.5\,\%$ and occurs at the outdoor-air

condition with the lowest enthalpy when the damper was 80 %. The compressor power ratio is observed to be inversely proportional to outdoor-air ambient enthalpy. This is reasonable since the pressure ratios become larger for greater outdoor-air temperature and humidity, so changes in evaporating pressure become less significant. Additionally, small decreases in compressor power can also be attributed to higher refrigerant mass flow rates that were required to maintain a constant superheat.

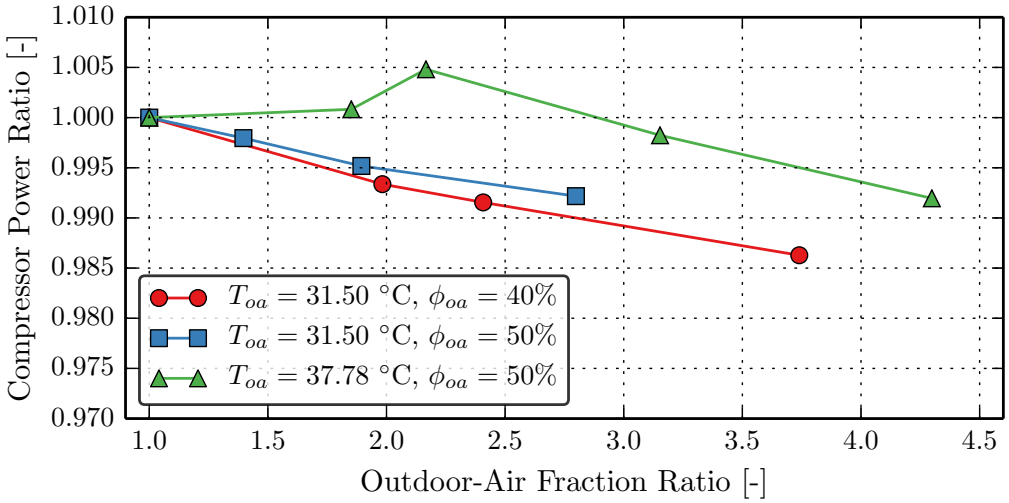

Figure 5.7. Compressor power ratio as a function of excess outdoor-air supplied to the RTU under different outdoor-air conditions. Modest decreases in compressor power are observed due to small increase in evaporating pressure and greater mass flow rates.

5.1.3 Cycle Efficiency Impact

With increases in capacity and decreases in required compressor power, the RTU cycle efficiency increases. An efficiency ratio, r_{COP}, is defined:

$$r_{\text{COP}} = \frac{\text{COP}_{\text{actual}}}{\text{COP}_{\text{normal}}} \tag{5.4}$$

where $\text{COP}_{\text{actual}}$ is the actual coefficient of performance and $\text{COP}_{\text{normal}}$ is the normal coefficient of performance if the system was operating normally. The coefficient of performance, COP is defined as the ratio of the cooling capacity to the required compression power:

$$\text{COP} = \frac{\dot{Q}_{\text{evap}}}{\dot{W}_{\text{comp}}} \tag{5.5}$$

The efficiency ratio is calculated for each damper fault impact test case in Figure 5.8. Increasing efficiency is achieved when the damper is stuck open at warmer outdoor-air conditions. When the damper is stuck $100\,\%$ open at the warmest condition tested, an improvement greater than $11\,\%$ in instantaneous efficiency is observed. Opposite trends would be observed when the outdoor-air enthalpy is less than the return-air enthalpy since decreases in capacity and increases in required power would be caused by stuck open dampers.

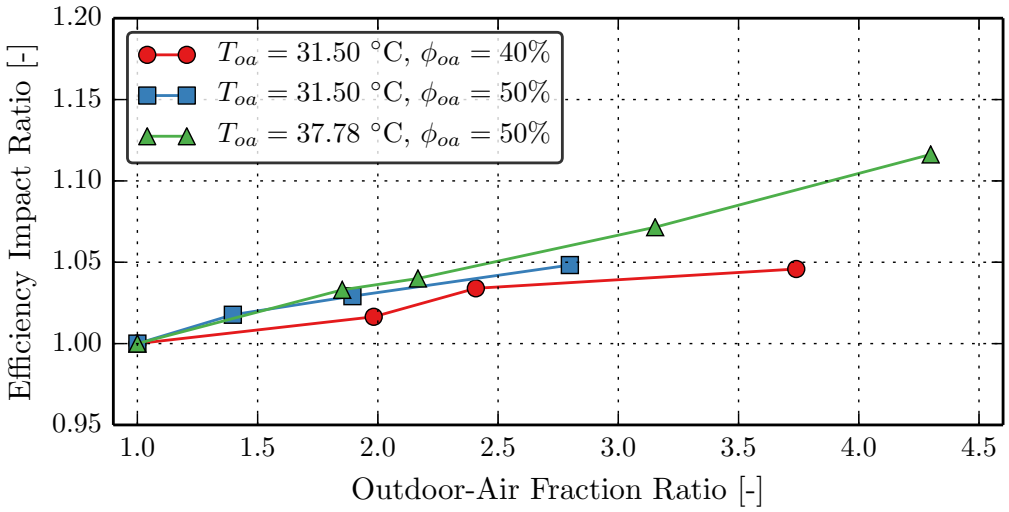

Figure 5.8. Improvement in cycle efficiency of the RTU under different combinations of damper positions and outdoor-air conditions caused by increased cooling capacity and decreased compressor power.

5.2 Ventilation Impact

Stuck outdoor-air dampers have a significant impact on the RTU ventilation process. For this analysis, four ventilation air streams will be considered, including the return-air, outdoor-air, mixed-air and supply-air streams. These air streams are plotted in Figure 5.9 when the system operates normally and subjected to $T_{\text{oa}} = 31.50\,°\text{C}$ and $\phi_{\text{oa}} = 50\,\%$. A mixing process between the return-air and outdoor-air takes place in the mixing box, so the mixed-air condition can be theoretically located anywhere on the line connecting these two points. Due to leakage however, the mixed-air may not be exactly the same as the return-air or outdoor-air conditions when the damper is $100\,\%$ open or closed. Depending on the cooling capacity of the system, the supply-air will be cooled and dehumidified during the cooling coil process.

There are several noticeable impacts of a stuck damper fault on the ventilation and cooling processes, as shown by Figure 5.10. The mixed-air conditions moves up the mixing process line closer to the outdoor-air condition since a greater fraction of outdoor-air enters the unit when the damper is stuck open. An interesting impact described earlier is the effect of return-air recirculation on the outdoor-air condition. Due to the geometry of the outdoor-air hood, a portion of the return-air that is exhausted out of the unit enters the outdoor-air stream. This effectively cools the outdoor-air before entering the RTU when $h_{\text{ra}} < h_{\text{oa}}$. Lastly, supply-air temperature and humidity is increased since the mixed-air conditions has more enthalpy. Even though the capacity of the RTU increases, the supply air enthalpy increases because the increase in capacity cannot overcome the increased ventilation load on the system.

The following sections will investigate the damper faults impact on ventilation load and sensible heat ratio. These are important considerations used to estimate the fault's impact on run-time, which will be discussed in a later section.

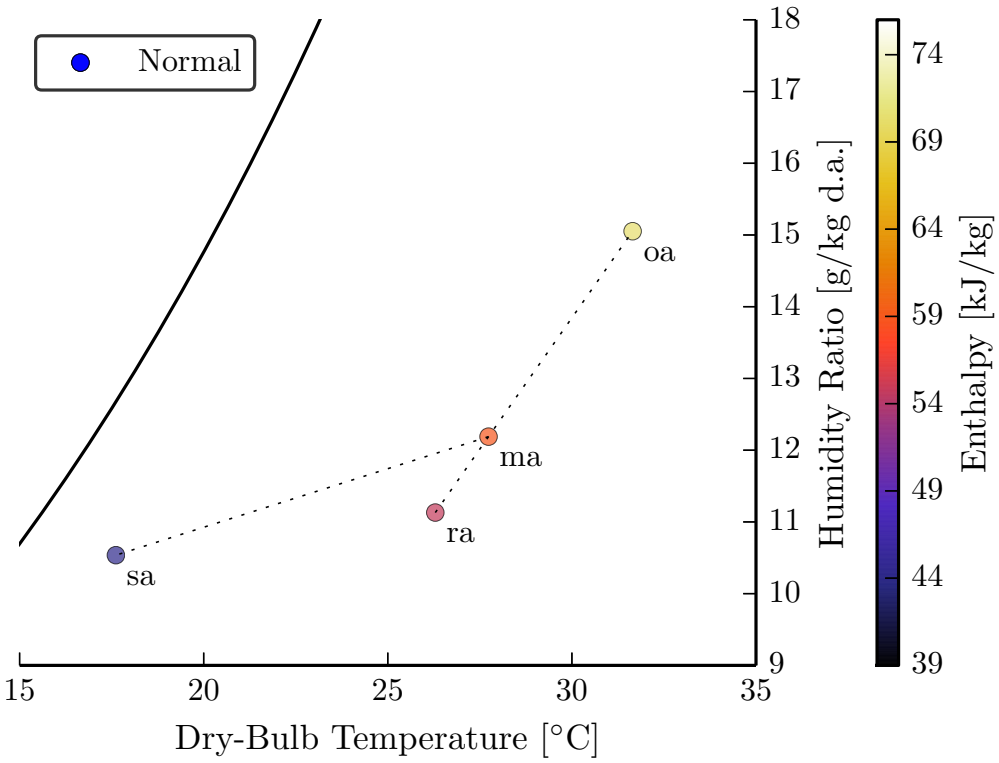

Figure 5.9. Ventilation and cooling processes plotted on a psychrometric chart when the outdoor-air temperature and relative humidity is 31.50 °C and 50%, respectively.

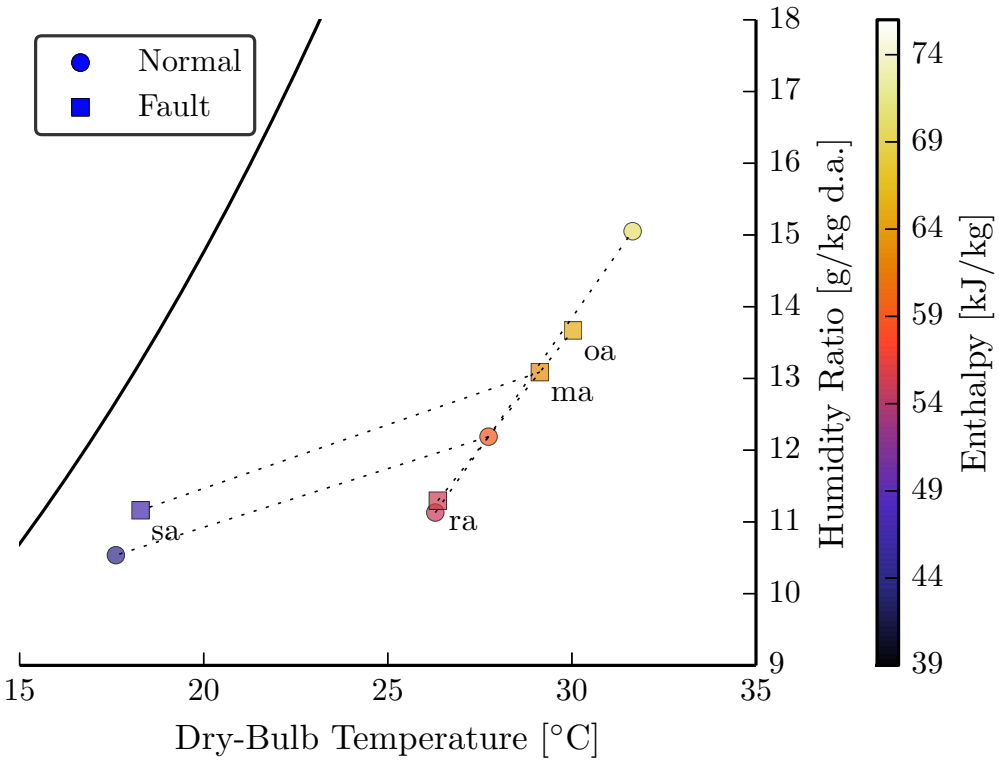

Figure 5.10. Ventilation and cooling processes plotted on a psychrometric chart when the outdoor-air temperature and relative humidity is 31.50 °C and 50%, respectively.

5.2.1 Ventilation Load Impact

The ventilation portion of the load can be calculated using Equation (5.6) as a function of the outdoor-air fraction and outdoor-air and return-air enthalpy, h_{oa} and h_{ra},

$$\dot{Q}_{\text{vent}} = \dot{m}_{\text{sa}}\text{OAF}\left(h_{\text{oa}} - h_{\text{ra}}\right) \tag{5.6}$$

where OAF is the outdoor-air fraction. The outdoor-air fraction can be calculated in terms of the mixing box air streams' enthalpy using Equation (5.7),

$$\text{OAF} = \frac{h_{\text{ma}} - h_{\text{ra}}}{h_{\text{oa}} - h_{\text{ra}}}. \tag{5.7}$$

Substituting Equation (5.7) into Equation (5.6) yields the ventilation load in terms of the mass air flow rate and difference between mixed-air and return-air enthalpy:

$$\dot{Q}_{\text{vent}} = \dot{m}_{\text{sa}}\left(h_{\text{ma}} - h_{\text{ra}}\right). \tag{5.8}$$

The ventilation load was calculated using Equation (5.8) for each of the test cases considered in Figure 5.11. With increasing outdoor-air fractions, the ventilation load entering the RTU increases when the outdoor-air enthalpy is greater than the return-air enthalpy. The ventilation load fraction is defined as the ratio of ventilation load to the total capacity of the RTU:

$$x_{\text{vent}} = \frac{\dot{Q}_{\text{vent}}}{\dot{Q}_{\text{evap}}}. \tag{5.9}$$

This fraction is plotted as a function of the outdoor-air fraction ratio for the different test conditions in Figure 5.12. For high temperature or humid conditions, the ventilation load can become a large fraction of the available cooling capacity. Furthermore, the ventilation could even become greater than the available cooling capacity if the damper is stuck almost fully-open during extreme outdoor-air conditions. In such cases, the RTU actually provides a net increase in the space load.

The relative impact of the stuck damper fault can be captured using the ventilation load ratio, given by Equation (5.10),

$$r_{\text{vent}} = \frac{\dot{Q}_{\text{vent,actual}}}{\dot{Q}_{\text{vent,normal}}}. \tag{5.10}$$

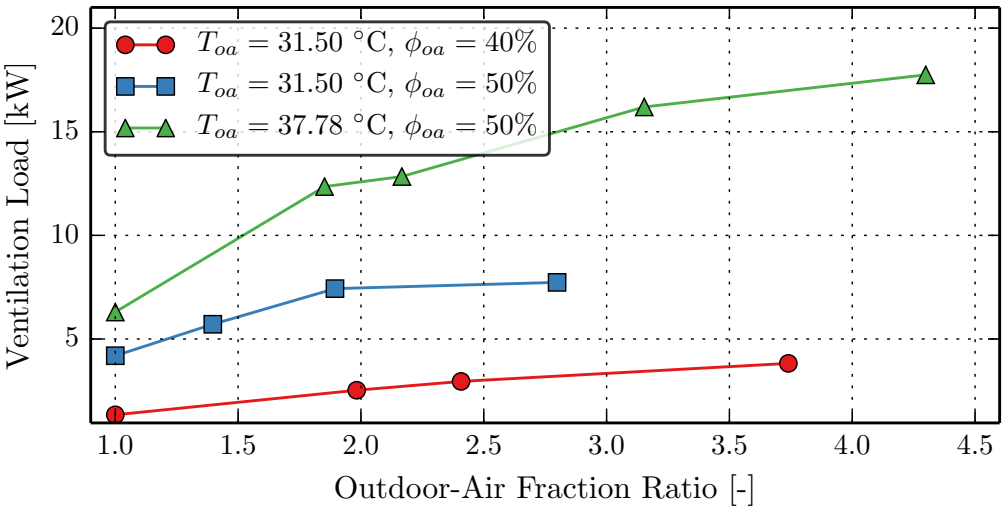

Figure 5.11. Ventilation load gained by mixing outdoor-air with return-air for different damper positions and outdoor-air conditions.

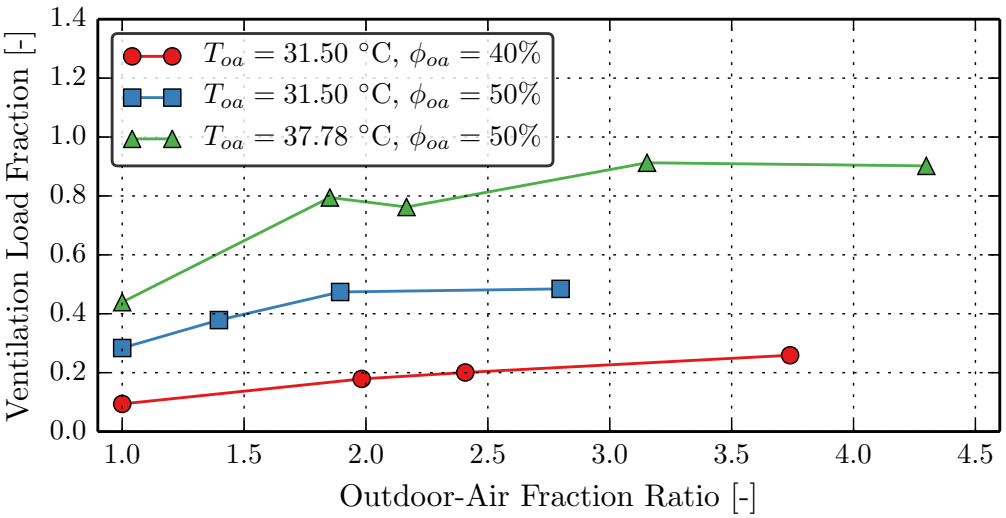

Figure 5.12. Ventilation load fraction for a range stuck open damper positions under different outdoor-air conditions.

Combining Equations (5.8) and (5.10) yields,

$$r_{\text{vent}} = \frac{\dot{m}_{\text{sa,actual}}}{\dot{m}_{\text{sa,normal}}} \frac{(h_{\text{ma}} - h_{\text{ra}})_{\text{actual}}}{(h_{\text{ma}} - h_{\text{ra}})_{\text{normal}}}. \tag{5.11}$$

For a outdoor-air damper fault, the impact on the supply-air flow rate is minimal. Under this assumption, the ventilation load ratio can be expressed as the ratio of mixed-air and return-air enthalpy differences,

$$r_{\text{vent}} = \frac{(h_{\text{ma}} - h_{\text{ra}})_{\text{actual}}}{(h_{\text{ma}} - h_{\text{ra}})_{\text{normal}}}. \tag{5.12}$$

Additionally, the fault may impact the return-air enthalpy in cases where the ventilation load becomes greater than the RTU capacity.

5.2.2 Sensible Heat Ratio Impact

The impact on sensible heat ratio is an important consideration when trying to characterize a faults overall impact on system performance. Since the sensible heat ratio, SHR, characterizes the fraction of sensible load to total load, any change in SHR will increase or decrease the latent heat removed during the cooling process. The evaporating temperature has an influence on SHR, and thus a stuck damper which causes a change in evaporator temperature may also change the SHR. The SHR impact ratio, r_{SHR} can be defined as the ratio of the faulty SHR to the SHR achieved when the RTU is operating correctly, Equation (5.13),

$$r_{\text{SHR}} = \frac{\text{SHR}}{\text{SHR}_{\text{normal}}} \tag{5.13}$$

where the SHR is calculated using air-side measurements:

$$\text{SHR} = \frac{C_p \left(T_{\text{ma}} - T_{\text{sa}}\right)}{h_{\text{ma}} - h_{\text{sa}}}. \tag{5.14}$$

The SHR impact ratio, r_{SHR} was calculated for each tested case and the results are shown in Figure 5.13. It should also be noted that the sensible heat ratio considered here is not the conditioned space sensible heat ratio, but ratio the ratio of sensible heat removed during the cooling coil process. The building will maintain its SHR while the RTU will meet this requirement.

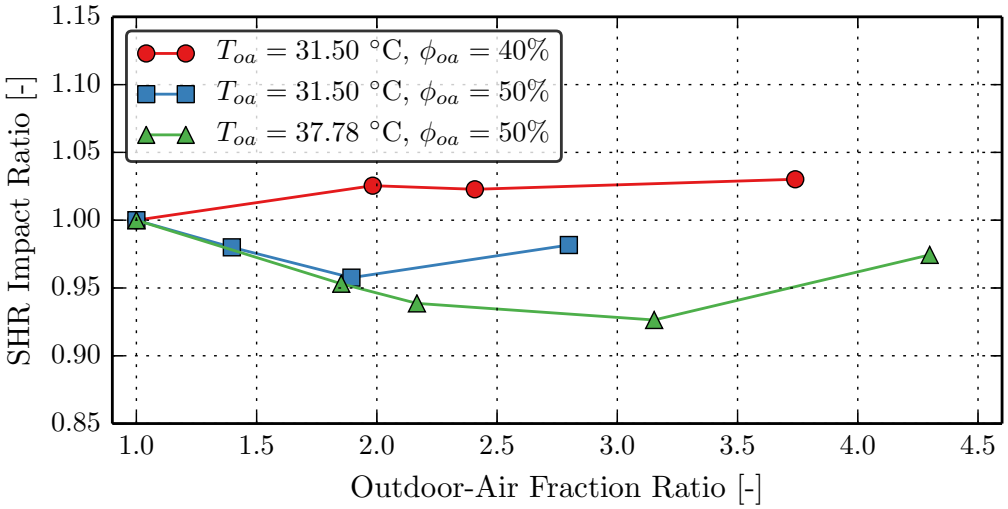

Figure 5.13. Equipment run-time impact under different outdoor ambient conditions and stuck damper positions. Note that for increasing outdoor-air enthalpy, the required run-time is increased due to the additional cooling load.

5.3 Run-Time Impact

A major impact of air conditioner faults, including damper faults is that of increased ventilation load during the cooling season. This additional ventilation load causes the total load on the RTU to increase. The total load on the RTU, Q_{load}, can be defined as a sum of the space load, Q_{space}, and the the ventilation load, Q_{vent},

$$Q_{\text{load}} = Q_{\text{space}} + Q_{\text{vent}}. \tag{5.15}$$

The time required to condition the total load, Δt_{load}, is given by Equation (5.16),

$$\Delta t_{\text{load}} = \frac{Q_{\text{load}}}{\dot{Q}_{\text{evap}}} \tag{5.16}$$

where $\dot{Q}_{\text{evap}}$ is the RTU cooling capacity. This time required, also called the run-time, can be rewritten as a function of Q_{space} and Q_{vent} by combining Equations (5.15) and (5.16),

$$\begin{aligned} \Delta t_{\text{load}} &= \frac{Q_{\text{space}} + Q_{\text{vent}}}{\dot{Q}_{\text{evap}}} \\ &= \frac{Q_{\text{space}}}{\dot{Q}_{\text{evap}}} + \frac{Q_{\text{vent}}}{\dot{Q}_{\text{evap}}}. \end{aligned} \tag{5.17}$$

Equation (5.17) as the sum of the time required to condition the space load component, Δt_{space}, and the time required to condition the ventilation load component, Δt_{vent},

$$\Delta t_{\text{load}} = \Delta t_{\text{space}} + \Delta t_{\text{vent}} \tag{5.18}$$

where

$$\Delta t_{\text{space}} = \frac{Q_{\text{space}}}{\dot{Q}_{\text{evap}}} \tag{5.19}$$

and

$$\Delta t_{\text{vent}} = \frac{Q_{\text{vent}}}{\dot{Q}_{\text{evap}}}. \tag{5.20}$$

From Equations (5.17) and (5.18), it is clear that an increase in the ventilation load caused by a stuck damper fault will increase the total run-time of the RTU.

From Equation (5.20), an increase in ventilation load or decrease in capacity will increase the ventilation load run-time requirement. A ratio can be defined between the actual and normal ventilation load run-time requirements using Equation (5.23),

$$r_{\Delta\text{vent}} = \frac{\Delta t_{\text{vent,actual}}}{\Delta t_{\text{vent,normal}}}. \tag{5.21}$$

The relative increase in run-time required to condition the ventilation load, $r_{\Delta\text{vent}}$, can be expressed in terms of the actual and normal ventilation load and capacity,

$$\begin{aligned} r_{\Delta\text{vent}} &= \frac{Q_{\text{vent,actual}}/\dot{Q}_{\text{evap,actual}}}{Q_{\text{vent,normal}}/\dot{Q}_{\text{evap,normal}}} \\ &= \frac{r_{\text{vent}}}{r_{\text{capacity}}} \end{aligned} \tag{5.22}$$

where r_{vent} is given by Equation (5.10) and r_{capacity} is given by Equation (5.2).

The space load run-time ratio, defined in Equation (5.23), is the relative increase or decrease in run-time required to condition the space load,

$$r_{\Delta\text{space}} = \frac{\Delta t_{\text{space,actual}}}{\Delta t_{\text{space,normal}}}. \tag{5.23}$$

With Equation (5.19), this can be expressed in terms of the actual and normal space load, Q_{space}, and capacity, $\dot{Q}_{\text{evap}}$,

$$\begin{aligned} r_{\Delta\text{space}} &= \frac{Q_{\text{space,actual}}/\dot{Q}_{\text{evap,actual}}}{Q_{\text{space,normal}}/\dot{Q}_{\text{evap,normal}}} \\ &= \frac{r_{\text{space}}}{r_{\text{capacity}}} \end{aligned} \tag{5.24}$$

where

$$r_{\text{space}} = \frac{Q_{\text{space,actual}}}{Q_{\text{space,normal}}}. \tag{5.25}$$

Li showed that RTU faults can have an impact on the space load by showing a dependence of r_{space} on r_{SHR} since the evaporation temperature is often impacted [26],

$$r_{\text{space}} = \frac{1}{r_{\text{SHR}}}. \tag{5.26}$$

Combining Equations (5.24) and (5.26) yields,

$$r_{\Delta\text{space}} = \frac{1}{r_{\text{SHR}} r_{\text{capacity}}}. \tag{5.27}$$

The actual run-time required to meet the total load in the presence of fault is given by,

$$\Delta t_{\text{load,actual}} = \Delta t_{\text{space,actual}} + \Delta t_{\text{vent,actual}}. \tag{5.28}$$

Equation (5.28) can be rewritten in terms of $r_{\Delta\text{vent}}$ and $r_{\Delta\text{space}}$ using Equations (5.22) and (5.24),

$$\Delta t_{\text{load,actual}} = r_{\Delta\text{space}} \Delta t_{\text{space,normal}} + r_{\Delta\text{vent}} \Delta t_{\text{vent,normal}}. \tag{5.29}$$

Using the normal ventilation load fraction, $x_{\text{vent,normal}}$, Equation (5.29) can be rewritten in terms of the normal total run-time, $\Delta t_{\text{load,normal}}$,

$$\Delta t_{\text{load,actual}} = r_{\Delta\text{space}} \left(1 - x_{\text{vent,normal}}\right) \Delta t_{\text{load,normal}} + r_{\Delta\text{vent}} x_{\text{vent,normal}} \Delta t_{\text{load,normal}}. \tag{5.30}$$

Dividing both sides of Equation (5.30) yields an expression for the relative increase in total run-time, $r_{\Delta\text{load}}$,

$$r_{\Delta\text{load}} = \left(1 - x_{\text{vent,normal}}\right) r_{\Delta\text{space}} + x_{\text{vent,normal}} r_{\Delta\text{vent}}, \tag{5.31}$$

or more explicitly,

$$\begin{aligned} r_{\Delta\text{load}} &= \left(1 - x_{\text{vent,normal}}\right) \frac{1}{r_{\text{SHR}} r_{\text{capacity}}} + x_{\text{vent,normal}} \frac{r_{\text{vent}}}{r_{\text{capacity}}} \\ &= \frac{1}{r_{\text{capacity}}} \left[\frac{1}{r_{\text{SHR}}} \left(1 - x_{\text{vent,normal}}\right) + r_{\text{vent}} x_{\text{vent,normal}} \right] \end{aligned} \tag{5.32}$$

The run-time impact ratio, $r_{\Delta\text{load}}$, was calculated and plotted for each test case in Figure 5.14. As ambient outdoor-air enthalpy increases, stuck open damper faults have increasing impact on required equipment run-time. This is due to the additional ventilation load brought into the system by the incorrect damper position. Note also that even relatively modest stuck damper faults can cause significant increases in run-time under very warm conditions. The run-time impact starts to saturate for higher outdoor-air fraction ratios due to the return-air recirculation effect. Because return-air recirculates back into the mixing box with the outdoor-air, especially when the damper is fully open, the impact does not increase linearly.

There are several effects of increased equipment run-time. Because the unit is required to run longer, more electricity must be consumed by the cooling process. Depending on

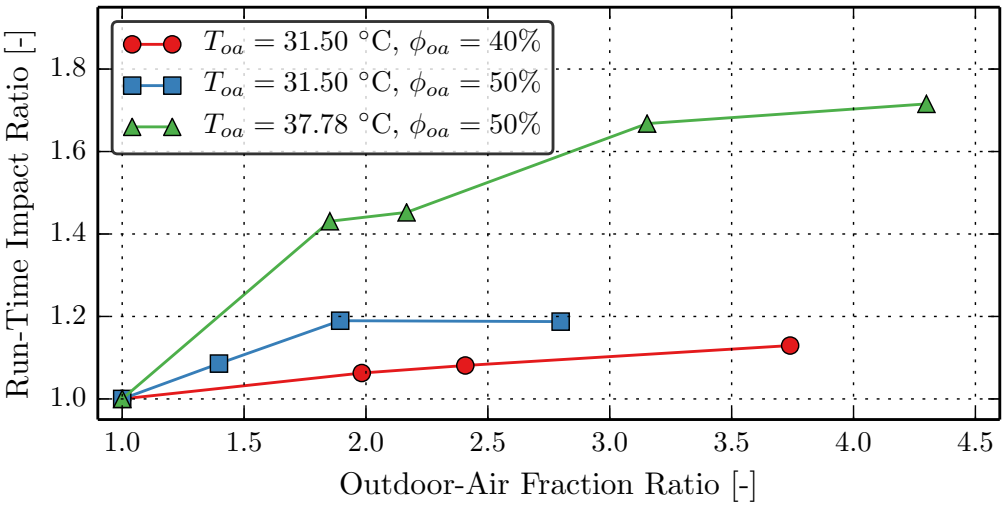

Figure 5.14. Equipment run-time impact under different outdoor ambient conditions and stuck damper positions. Note that for increasing outdoor-air enthalpy, the required run-time is increased due to the additional cooling load.

the ambient conditions, the actual amount of additional energy consumed is tied to the instantaneous efficiency and cooling capacity of the RTU:

$$\begin{aligned} W_{\text{elec}} &= \dot{W}_{\text{comp}} \Delta t_{\text{load}} \\ &= \frac{\dot{Q}_{\text{evap}}}{\text{COP}} \Delta t_{\text{load}}. \end{aligned} \tag{5.33}$$

In previous sections it was shown that there are modest gains in cooling capacity and efficiency on account of the increased evaporation temperature caused by the stuck open damper. However, these benefits are outweighed by the negative impact on RTU run-time caused by the significantly increased ventilation load. The relative impact of the required energy consumption can be defined using Equation (5.34),

$$r_W = \frac{W_{\text{elec}}}{W_{\text{elec, normal}}} \tag{5.34}$$

where $W_{\text{elec, normal}}$ is the expected energy consumption under normal operation. Combining Equations (5.33) and (5.34), the energy impact ratio can be rewritten,

$$r_W = \frac{r_{\text{capacity}}}{r_{\text{COP}}} r_{\Delta\text{load}}. \tag{5.35}$$

Equation (5.35) was evaluated for each test case and the results are shown in Figure **??**.

An additional outcome of the increased run-time is the degradation in equipment life. If it is assumed the RTU has a fixed number of lifetime run-time hours, any increase in required run-time decreases the expected life of the unit. Earlier than expected equipment replacement times are the effect of increased equipment run-time. Moreover, this increases the cost to run the equipment per unit time.

5.4 Conclusion

An investigation into the impact of stuck open damper faults during warm or humid outdoor-air conditions was conducted using experimental data. It was shown that because of a higher evaporation temperature, the RTU cooling capacity and efficiency is benefited from the higher outdoor-air fraction. Additionally, a small decrease in power consumption was shown for the test cases. Besides the cycle impact, a larger impact was observed on the

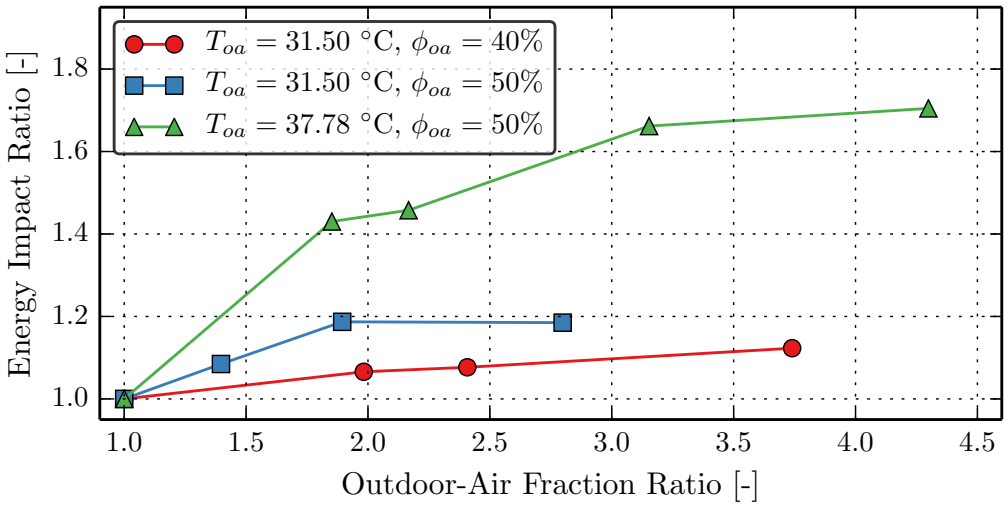

Figure 5.15. RTU energy impact under different outdoor ambient conditions and stuck damper positions. Note that for increasing outdoor-air enthalpy, the required energy increases due to the additional ventilation load.

ventilation load. Because more outdoor-air is provided to the unit when the damper is stuck open, the mixed-air temperature increases. The affect of this is a higher supply-air enthalpy and also an increased run-time. Run-time is increased because a larger portion of the cooling capacity must be used to cool the ventilation load. In the warmest, most humid case studied, this portion of the load was equivalent to over 80% of the total cooling capacity. Its also possible that there might not be any left-over cooling capacity left-over after treating the ventilation load during very hot or humid conditions.

The result of these operational performance impacts on the RTU leads to increased energy usage and increased equipment costs. Equipment costs are increased due to the longer run-time requirement caused by the damper fault. Since the equipment must run longer and harder for the same building loads, more frequent equipment replacement can be expected.

Besides these impacts, there are also impacts on building occupant comfort. This is an impact of both the higher supply-air enthalpy as well as the increased time run-time. A higher outdoor-air fraction can lead to higher moisture content in the conditioned space since the evaporation temperature is increased under warmer outdoor-air conditions. With the additionally ventilation load caused by the stuck damper, a higher supply-air temperature is supplied to the conditioned space. Because of this, it may take longer for the occupants to feel comfortable. In cases when the outdoor-air becomes very warm and moist, its possible the ventilation load becomes greater than the RTU cooling capacity. In these cases, a net increase in load is produced by the RTU on the conditioned space. This will most definitely cause comfort complaints unless alternative cooling systems are available to supplement the faulty system.

While only stuck open damper faults during warm or humid outdoor conditions were considered in this study, other types of outdoor-air damper faults exists. Its also possible that the outdoor-air damper could be stuck closed during times when “free-cooling” is available. In such cases, the fault is a missed opportunity to use cooler outdoor-air to reduce or eliminate the need to use mechanical cooling. A further study of these conditions is recommended in order to develop a methodology for quantifying these fault impacts.

Lastly, a methodology for quantifying the long-term impact of outdoor-air damper faults should be pursued. A starting point for this might be a modification to the economic performance degradation index (EPDI) proposed by Li [6]. Additionally, since the outdoor-air conditions are transient and ultimately the driving force behind stuck damper fault impacts, the model should be able to account for this unsteady nature.

6. SUMMARY AND RECOMMENDATIONS

The primary objective of this research was to develop a low-cost fault detection and diagnosis method for rooftop unit economizers. A set of common faults affecting rooftop unit economizers, including stuck dampers and temperature sensor faults, was made and the method designed to address these issues. The proposed method was designed to be integrated into the economizer controller and use low cost sensors in order to minimize installation costs. Integrating the FDD method into the controller simplifies many of its components. Instead of focusing on many different types of RTUs and economizer combinations, a more simple method was designed for an individual unit. This simplified the RTU modeling and FDD training as well and also allowed the methods to be experimentally validated using data collected from well-controlled laboratory testing.

Previous literature suggested that using a single-point mixed-air temperature sensor for FDD is especially error-prone due to large thermal stratification within rooftop air conditioner mixing boxes [18]. The RTU studied in this research was no exception to this rule, so a mixed-air temperature correction model was created in order to reduce the mixed-air temperature sensor error. The model corrected the measured mixed-air temperature and adjusted it based on the outdoor- and return-air temperatures and the controlled damper position. A final term was added to the linear model in order to account for effects of air flow rate through the RTU. The resulting model yielded a RMSE of $0.652\,^{\circ}\mathrm{C}$, an improvement of $70.4\,\%$ improvement from a baseline of $2.20\,^{\circ}\mathrm{C}$.

The design of the outdoor-air intake hood required a similar correction to be applied to the outdoor-air temperature sensor. Because of the location of the barometric relief vent and the outdoor-air intake, return-air that was exhausted from the unit recirculated back into the RTU with outdoor-air. This problem produced thermal stratification at the outdoor-air temperature sensor location producing error dependence on the damper position. The more open the outdoor-air damper was, more return-air was recirculated back into the unit. From

a baseline of $2.162\,°C$, the outdoor-air temperature sensor RMSE was reduced by $64.5\,\%$ to $0.789\,°C$.

Many economizer FDD tools and methods require estimations of the outdoor-air fraction when the damper is fully-closed, fully-opened, and at the position providing the minimum acceptable outdoor-air requirement [10, 14, 17, 18]. These are difficult to estimate on-site since there is generally no air-flow measurement devices installed on RTUs. It also precludes fault detection when the economizer controls the outdoor-air damper to an intermediate position, possibly during "free-cooling" mode. In order to overcome these limitations, an outdoor-air fraction model was developed based on only the outdoor-air damper actuator control signal. A third-order linear model was trained using laboratory data to capture the relationship between outdoor-air fraction and the damper control signal. The RMSE of the outdoor-air fraction model was $4.51\,\%$ when compared with estimates based on a RTU energy balance. Further, much of this error is caused hysteresis in the damper stroke which was neglected but was shown to be significant.

Additional models were made to characterize the indoor fan. The first model developed was used to correct the supply-air temperature measurement for the temperature rise between the evaporator outlet and and supply-air caused by indoor fan. A linear model for indoor fan temperature rise based on indoor fan speed and mass air flow rate was developed and achieved an RMSE of $0.048\,°C$. The mass air flow rate is estimated using an indoor fan mass air flow rate model. This model was developed based on an experimentally derived indoor fan performance map. A nonlinear model taking the form of a sigmoidal function was trained using least-squares regression on indoor fan differential pressure and speed. The mass-air flow rate model achieved an RMSE of $2.67\,\%$. A similar model was developed for indoor fan power and had an RMSE of $3.01\,\%$.

Using the models created for normal performance, a passive fault detection method was designed. The method observes the measured outdoor-air fraction estimation based on mixing box temperature measurements and compares the value with the outdoor-air fraction prediction model based on the actuator control signal. A Bayesian classifier previously developed for refrigerant-side fault detection was adapted to identify economizer fault

problems by statistical determination of when the OAF estimation and prediction have deviated [5, 7]. When using a required confidence of $99.994\,\%$, false alarms were eliminated entirely when normal experimental test data was tested. The fault detection was able to identify faults when a $30\,\%$ difference in expected and actual damper position was present. For deviations greater than this, the method was able to identify the fault in all tests. The required difference between the expected and actual damper positions could be reduced by reducing the required confidence level. However this would also lead to higher percentage of false alarms, which is not advisable.

The results also showed a potential limitation of passive fault detection methods if the goal is to identify problems as quickly as possible. For faulty damper positions that were near the expected damper position, a fault cannot be detected until the damper is controlled to a different position. Alternatively, this also highlights a situation when faults might not have an impact on actual system performance and detection during these times is not necessarily important. This can be supported from an energy perspective since no significant energy or run-time would be required during these situations.

An active diagnosis method was proposed to diagnose the following faults:

- stuck outdoor-air damper faults
- outdoor-air temperature sensor bias faults
- return-air temperature sensor bias faults
- mixed-air temperature sensor bias faults
- supply-air temperature sensor bias faults.

Previous economizer FDD methods using functional testing have been proposed, however all have used rule-based strategies as the primary diagnosis method [20]. The method first sweeps the outdoor-air damper fully-open and fully-closed while calculating a set of diagnosis performance residuals based on mass and energy balance when the damper is at these positions. An enabling characteristic of these residuals is that they are impacted by different faults uniquely. Because of this, the response of the diagnosis residuals can

be classified as belonging to different fault types. This classification is performed by a Bayesian diagnosis classifier trained using experimental data.

The diagnosis method was tested under different fault conditions using experimental data in order to assess its performance. The diagnosis method was able to diagnosis normal performance correctly in greater than $95\,\%$ of the test cases analyzed. When taken with the fault detection false alarm rate, the false alarm rate of the entire FDD tool was approximately $0.05\,\%$. This low false alarm rate can be attributed to the accuracy of the temperature sensor correction and outdoor-air fraction models that can be attained when using experimentally obtained training data for an individual RTU. The diagnosis tool was also able to correctly identify greater than $90\,\%$ of the different faults studied correctly.

An investigation into the impacts of stuck damper faults on RTU performance was conducted using experimental data. The results of the analysis showed that an increase in cycle efficiency and cooling capacity is achieved by supplying a larger percentage of warmer outdoor-air to the unit due to the increase in evaporation temperature and pressure. Because only the low-side pressure is affected by the fault, the compressor pressure ratio is decreased. In addition to the cycle impacts, the ventilation load is increased significantly as the outdoor-air fraction and outdoor-air enthalpy is increased. In extreme cases, this ventilation can account for a large portion of the cooling capacity provided by the RTU. Because more of the cooling capacity is required to cool a larger fraction of outdoor-air, the remaining capacity used to cool the conditioned space is reduced. When this occurs, the RTU must run for a longer time in order to meet the equivalent load. This run-time impact will lead to increased energy consumption and shortened equipment life.

Based on the results of this research, the following recommendations are proposed.

- The difference between the return-air inlet and the ambient pressures is an important consideration due to its affects on the return-air recirculation characteristic, however it was not considered in this research. Since this is highly dependent on the building geometry and duct layout, a mechanism to re-train the RTU models should be investigated before this technology realistically can be added to the marketplace.

- The FDD method designed focused on a system using a dry-bulb economizer controller and as such no humidity sensor faults were considered. The method could be expanded to include enthalpy based economizer controllers which typically rely on relative humidity sensors calculate enthalpy with the temperature measurements. This could be accomplished by adding a set of additional diagnosis residuals that could be calculated when humidity sensors are used.

- A method that is able to decouple the different economizer faults should be explored. This would enable the diagnosis of simultaneous economizer faults.

- The thresholds used to analyze the performance of the FDD method were chosen based on minimizing false alarm rate and maximizing the fault detection and diagnosis sensitivity. However, a more through investigation in determining optimal thresholds based on energy, comfort, and equipment health impact caused by the fault. A optimal decision should be recommended based on these impacts and an estimated cost to perform service.

- Economizer fault impact models should be designed to provide accurate estimates of energy and cost impacts. In order to do this, a wider range of ambient test conditions should be tested in order to capture the impact of not only additional outdoor-air during warmer or more humid outdoor conditions but also when insufficient outdoor-air is supplied when it would be advantageous to open the damper. Missed opportunities to provide "free-cooling" could be a significant energy impact in some climate regions.

- Extensive testing was used to train the models and AFDD methods developed in this thesis. While the accuracy yielded from this testing was sufficient, it would be helpful determine if it is possible to reduce the training size while maintaining adequate accuracy and robustness. Moreover, "standardized" or recommended procedures should be defined in order to aid in developing these models.

LIST OF REFERENCES

LIST OF REFERENCES

[1] Energy Information Agency (EIA). Commercial buildings energy consumption survey 2003. Technical report, US Department of Energy, Washington, DC, December 2008.

[2] S. Katipamula and S. Gaines. Characterization of building controls and energy efficiency options using commercial building energy consumption survey. Technical Report PNWD-3247, Iowa Energy Center, Iowa State University, Ames, Iowa, February 2003.

[3] S. Katipamula and M. R. Brambley. Methods for fault detection, diagnostics, and prognostics for building systemsa review, part I. *HVAC&R Research*, 11(1):3–25, 2005.

[4] S. Katipamula and M. R. Brambley. Methods for fault detection, diagnostics, and prognostics for building systemsa review, part II. *HVAC&R Research*, 11(2):169–187, 2005.

[5] T. M. Rossi. *Detection, Diagnosis, and Evaluation of Faults in Vapor Compression Cycle Equipment*. PhD thesis, Purdue University, December 1995.

[6] H. Li. *A Decoupling-Based Unified Fault Detection and Diagnosis Approach for Packaged Air Conditioners*. PhD thesis, School of Mechanical Engineering, Purdue University, 2004.

[7] W. Kim. *Fault Detection and Diagnosis for Air Conditioners and Heat Pumps based on Virtual Sensors*. PhD thesis, School of Mechanical Engineering, Purdue University, 2013.

[8] Work Order 32 EM and V Team. WO32 EM and V interim findings memo for commercial quality maintenance - volume 1 - field observations. Technical report, DNV KEMA Energy and Sustainability Robert Mowris and Associates, Inc., August 2013.

[9] Work Order 32 EM and V Team. WO32 EM and V interim findings memo for commercial quality maintenance - volume 2 - laboratory tests. Technical report, DNV KEMA Energy and Sustainability Robert Mowris and Associates, Inc., August 2013.

[10] M. Brambley, R. Pratt, D. Chassin, S. Katipamula, and D. Haley. Diagnostics for outdoor air ventilation and economizers. *ASHRAE Journal*, pages 49–55, October 1998.

[11] California Building Standards Commission. 2013 building energy efficiency standards for residential and nonresidential buildings. Technical Report CEC-400-2012-004-CMF, California Energy Commission, Sacramento, CA, May 2012.

[12] S. Katipamula, R. G. Pratt, D. P. Chasin, Z. T. Taylor, and M. R. Brambley. Automated fault detection and diagnostics for outdoor-air ventilation systems and economizers: Methodology and results from field testing. *ASHRAE Transactions*, 105(1):258–265, 1999.

[13] J. M. House, H. Vaezi-Nejad, and J. M. Whitcomb. An expert rule set for fault detection in air-handling units. *ASHRAE Transactions*, 107(1):858–871, 2001.

[14] J. E. Seem and J. M. House. Integrated control and fault detection of air-handling units. *HVAC&R Research*, 15(1):25–55, 2009.

[15] J. Schein, S. T. Bushby, and J. M. House. Results from laboratory testing of embedded air handling unit and variable air volume box fault detection tools. Technical Report NISTIR 7036, National Institute of Standards and Technology, Gaithersburg, MD 20899-8530, August 2003.

[16] J. Schein and S. T. Bushby. Fault detection & diagnostics for ahus and vav boxes. *ASHRAE Journal*, pages 58–63, July 2005.

[17] J. Schein. Results from field testing of embedded air handling unit and variable air volume box fault detection tools. Technical Report NISTIR 7365, National Institute of Standards and Technology, Gaithersburg, MD 20899-8530, October 2006.

[18] A. J. Wichman. *Evaluation of Fault Detection and Diagnosis Methods for Refrigeration Equipment and Air-Side Economizers*. Master's thesis, Purdue University, West Lafayette, Indiana 47907-2031, August 2007.

[19] A. Wichman and J. E. Braun. A smart mixed-air temperature sensor. *HVAC&R Research*, 15(1):101–115, 2009.

[20] N. Fernandez, M. R. Brambley, and S. Katipamula. Self-correcting hvac controls: Algorithms for sensors and dampers in air-handling units. Technical Report PNNL-19104, Pacific Northwest National Laboratory, December 2009.

[21] Steven T. Taylor and C. Hwakong Cheng. Economizer high limit controls and why enthalpy economizers don't work. *ASHRAE Journal*, 15(1):1–11, 2010.

[22] T. M. Rossi and J. E. Braun. A statistical rule-based fault detection and diagnostic method for vapor compression air conditioners. *International Journal of HVAC&R Research*, 3(1):19–37, 1997.

[23] H. Friedman and M. A. Piette. Comparative guide to emerging diagnostic tools for large commercial hvac systems. Technical Report LBNL Report 48629, Lawrence Berkeley National Laboratory, Berkeley, CA, May 2001.

[24] C. Sun, F. Finaish, and H. J. Sauer. Parametric study of thermal mixing characteristics in a mixing chamber. Technical report, Department of Mechanical, Aerospace Engineering and Engineering Mechanics, University of Missouri-Rolla, Rolla, Missouri 65409, 2001.

[25] K. Fukunaga. *Introduction to Statistical Pattern Recognition*. Academic Press, Purdue University, West Lafayette, IN, USA, 1990.

[26] H. Li and J. E. Braun. An overall performance index for characterizing the economic impact of faults in direct expansion cooling equipment. *International Journal of Refrigeration*, 30:299–310, 2007.

APPENDIX

A. EXPERIMENTAL DATA

A.1 Indoor Fan Performance Test Data

Table A.1.
Indoor fan temperature rise measured for different indoor fan operating conditions, tests 1 to 20.

Test	γ_{idf}	ΔP_{idf}	T_{ma}	T_{sa}	ΔT_{idf}
	%	Pa	°C	°C	°C
1	50.00	92.13	23.37	24.03	0.66
2	66.67	126.26	23.88	24.56	0.68
3	58.33	94.78	23.82	24.42	0.61
4	41.67	20.02	24.93	25.32	0.39
5	41.67	41.22	23.40	23.82	0.42
6	58.33	62.57	24.88	25.35	0.47
7	75.00	185.63	24.31	25.12	0.81
8	58.33	107.89	24.82	25.43	0.61
9	75.00	222.64	24.07	25.11	1.04
10	33.33	41.09	23.10	23.61	0.50
11	41.67	56.07	24.62	25.19	0.57
12	91.67	233.87	23.97	24.95	0.98
13	83.33	165.81	23.70	24.58	0.88
14	66.67	159.38	24.09	24.88	0.80
15	75.00	127.26	23.17	23.96	0.79
16	50.00	42.59	23.39	23.85	0.46
17	66.67	196.37	23.95	25.10	1.15
18	91.67	215.50	23.90	24.87	0.97
19	58.33	145.42	23.80	24.90	1.10
20	83.33	245.69	23.94	25.01	1.07

Table A.2.
Indoor fan temperature rise measured for different indoor fan operating conditions, tests 21 to 41.

Test	γ_{idf}	ΔP_{idf}	T_{ma}	T_{sa}	ΔT_{idf}
	%	Pa	°C	°C	°C
21	83.33	238.54	24.34	25.27	0.93
22	66.67	150.31	24.04	24.80	0.76
23	50.00	30.66	24.95	25.37	0.42
24	58.33	122.62	23.90	24.60	0.70
25	83.33	214.26	24.41	25.29	0.88
26	50.00	108.51	23.62	24.72	1.10
27	83.33	196.13	24.49	25.34	0.86
28	66.67	78.23	23.75	24.45	0.70
29	66.67	97.40	23.70	24.32	0.62
30	75.00	239.01	24.04	25.15	1.11
31	66.67	207.59	23.62	25.14	1.52
32	50.00	74.95	24.78	25.33	0.55
33	50.00	61.86	24.81	25.30	0.48
34	41.67	75.31	23.48	24.55	1.07
35	58.33	82.51	24.90	25.43	0.53
36	70.00	99.47	23.00	23.72	0.72
37	76.18	155.47	24.19	24.95	0.76
38	75.00	202.44	24.18	25.07	0.89
39	66.67	173.46	24.02	24.99	0.97
40	58.33	40.48	22.81	23.39	0.58
41	41.67	32.26	23.62	24.15	0.54

Table A.3.
Indoor fan flow rates measured for different indoor fan operating conditions, tests 1 to 20.

Test	γ_{idf}	ΔP_{idf}	$\dot{V}_{\text{sa}}$	$\dot{m}_{\text{sa}}$
	%	Pa	m^3/s	kg/s
1	50.00	92.13	0.2278	0.2637
2	66.67	126.26	0.5668	0.6553
3	58.33	94.78	0.5026	0.5811
4	41.67	20.02	0.5564	0.6422
5	41.67	41.22	0.4137	0.4794
6	58.33	62.57	0.6872	0.7932
7	75.00	185.63	0.5427	0.6265
8	58.33	107.89	0.4186	0.4829
9	75.00	222.64	0.2519	0.2911
10	33.33	41.09	0.1460	0.1691
11	41.67	56.07	0.2784	0.3214
12	91.67	233.87	0.7938	0.9169
13	83.33	165.81	0.8396	0.9704
14	66.67	159.38	0.3230	0.3733
15	75.00	127.26	0.8186	0.9478
16	50.00	42.59	0.6056	0.7010
17	66.67	196.37	0.1549	0.1789
18	91.67	215.50	0.8668	1.0013
19	58.33	145.42	0.1524	0.1761
20	83.33	245.69	0.4312	0.4977

Table A.4.
Indoor fan flow rates measured for different indoor fan operating conditions, tests 21 to 41.

Test	γ_{idf}	ΔP_{idf}	$\dot{V}_{sa}$	$\dot{m}_{sa}$
	%	Pa	m^3/s	kg/s
21	83.33	238.54	0.4779	0.5515
22	66.67	150.31	0.3948	0.4563
23	50.00	30.66	0.6671	0.7699
24	58.33	122.62	0.2786	0.3224
25	83.33	214.26	0.6322	0.7295
26	50.00	108.51	0.1244	0.1438
27	83.33	196.13	0.7040	0.8121
28	66.67	78.23	0.7940	0.9186
29	66.67	97.40	0.7387	0.8544
30	75.00	239.01	0.1966	0.2271
31	66.67	207.59	0.1236	0.1428
32	50.00	74.95	0.3893	0.4492
33	50.00	61.86	0.4759	0.5492
34	41.67	75.31	0.1033	0.1196
35	58.33	82.51	0.5748	0.6631
36	70.00	99.47	0.8034	0.9309
37	76.18	155.47	0.6993	0.8076
38	75.00	202.44	0.3672	0.4241
39	66.67	173.46	0.2351	0.2716
40	58.33	40.48	0.7702	0.8929
41	41.67	32.26	0.2752	0.3187

Table A.5.
Indoor fan power measured for different indoor fan operating conditions, tests 1 to 20.

Test	γ_{idf}	ΔP_{idf}	$\dot{W}_{\text{idf}}$
	%	Pa	W
1	50.00	92.13	164.21
2	66.67	126.26	499.43
3	58.33	94.78	411.84
4	41.67	20.02	335.03
5	41.67	41.22	295.52
6	58.33	62.57	417.97
7	75.00	185.63	560.03
8	58.33	107.89	380.36
9	75.00	222.64	439.86
10	33.33	41.09	104.54
11	41.67	56.07	273.71
12	91.67	233.87	917.65
13	83.33	165.81	764.73
14	66.67	159.38	266.33
15	75.00	127.26	658.23
16	50.00	42.59	392.28
17	66.67	196.37	225.82
18	91.67	215.50	903.51
19	58.33	145.42	187.61
20	83.33	245.69	448.28

Table A.6.
Indoor fan power measured for different indoor fan operating conditions, tests 21 to 41.

Test	γ_{idf}	ΔP_{idf}	$\dot{W}_{\text{idf}}$
	%	Pa	W
21	83.33	238.54	602.20
22	66.67	150.31	420.02
23	50.00	30.66	351.18
24	58.33	122.62	207.55
25	83.33	214.26	694.24
26	50.00	108.51	150.31
27	83.33	196.13	735.49
28	66.67	78.23	547.44
29	66.67	97.40	517.78
30	75.00	239.01	287.41
31	66.67	207.59	222.91
32	50.00	74.95	328.15
33	50.00	61.86	353.72
34	41.67	75.31	121.72
35	58.33	82.51	440.03
36	70.00	99.47	588.75
37	76.18	155.47	655.55
38	75.00	202.44	342.54
39	66.67	173.46	381.33
40	58.33	40.48	456.07
41	41.67	32.26	261.74

A.2 Economizer Fault Impact Test Data

Table A.7.
Ventilation air temperatures and calculated outdoor-air fraction estimates for economizer fault impact tests under the different test conditions. Outdoor-air fraction estimates were calculated using Equation (3.3) and the average air temperature measurements within the mixing box.

Test	γ_{oad}	$T_{oa,ave}$	$T_{ra,ave}$	$T_{ma,ave}$	$T_{sa,ave}$	OAF_{ma}
	%	°C	°C	°C	°C	–
			Condition 1			
0	10.0	31.89	26.39	27.31	16.87	0.1671
1	30.0	31.75	26.34	28.14	17.35	0.3314
2	50.0	31.59	26.35	28.46	17.19	0.4023
3	70.0	30.58	26.29	28.97	17.12	0.6250
			Condition 2			
0	20.0	31.65	26.28	27.73	17.62	0.2698
1	40.0	31.64	26.35	28.34	18.04	0.3770
2	60.0	31.28	26.39	28.89	18.20	0.5112
3	80.0	30.03	26.36	29.13	18.28	0.7551
			Condition 3			
0	0.0	37.56	26.38	28.52	19.15	0.1909
1	33.0	37.47	26.39	30.31	20.48	0.3535
2	50.0	37.37	26.49	30.99	21.11	0.4136
3	67.0	37.27	26.51	32.12	21.50	0.6020
4	100.0	37.22	26.50	33.04	21.78	0.8207

Table A.8.
Ventilation air dew point temperatures measured for economizer fault impact tests under the different test conditions. The mixed-air dew points were estimated assuming Equation (2.4).

Test	γ_{oad}	D_{oa}	D_{ra}	D_{ma}	D_{sa}
	%	°C	°C	°C	°C
	Condition 1				
0	10.0	16.72	15.48	15.69	13.69
1	30.0	16.69	15.61	15.97	14.15
2	50.0	16.65	15.64	16.04	14.13
3	70.0	16.54	15.64	16.20	14.26
	Condition 2				
0	20.0	20.31	15.61	16.88	14.77
1	40.0	20.27	15.74	17.44	15.22
2	60.0	20.10	15.61	17.90	15.46
3	80.0	18.79	15.62	18.02	15.65
	Condition 3				
0	0.0	24.50	15.70	17.38	16.26
1	33.0	25.16	15.71	19.05	17.53
2	50.0	23.98	15.71	19.13	18.41
3	67.0	23.14	15.74	20.20	18.60
4	100.0	21.74	15.75	20.67	19.10

Table A.9.
Ventilation air enthalpy calculated using measured dry-bulb and dew point temperatures for the economizer fault impact tests under the different test conditions.

Test	γ_{oad}	h_{oa}	h_{ra}	h_{ma}	h_{sa}
	%	kJ/kg	kJ/kg	kJ/kg	kJ/kg
	Condition 1				
0	10.0	62.70	54.67	56.02	41.79
1	30.0	62.49	54.86	57.39	43.05
2	50.0	62.26	54.92	57.88	42.86
3	70.0	60.99	54.88	58.70	42.01
	Condition 2				
0	20.0	70.35	54.82	59.01	44.40
1	40.0	70.26	55.11	60.82	45.64
2	60.0	69.46	54.92	62.35	46.23
3	80.0	65.14	54.91	62.64	46.67
	Condition 3				
0	0.0	88.07	55.07	61.37	48.69
1	33.0	90.05	55.11	67.47	52.59
2	50.0	86.26	55.22	68.06	55.11
3	67.0	82.20	55.29	71.49	55.92
4	100.0	76.92	55.29	73.04	57.33

Table A.10.
Indoor fan measurements and supply-air flow rates for economizer fault impact tests under different test conditions.

Test	γ_{oad}	γ_{idf}	ΔP_{idf}	$\dot{V}_{sa}$	$\dot{m}_{sa}$	$\dot{W}_{idf}$
	%	Hz	Pa	m^3/s	kg/s	W
	Condition 1					
0	10.0	41.0	246.35	0.6665	0.7796	41.07
1	30.0	41.0	246.23	0.6943	0.8107	41.14
2	50.0	41.0	246.23	0.6673	0.7794	40.87
3	70.0	41.0	246.24	0.6724	0.7853	41.01
	Condition 2					
0	20.0	41.0	246.24	0.6681	0.7786	39.95
1	40.0	41.0	246.23	0.6665	0.7755	40.13
2	60.0	41.0	246.24	0.6640	0.7721	40.07
3	80.0	41.0	246.24	0.6747	0.7840	40.64
	Condition 3					
0	0.0	41.0	246.32	0.6672	0.7694	39.34
1	33.0	41.0	246.34	0.6636	0.7614	39.39
2	50.0	41.0	246.27	0.6578	0.7521	39.02
3	67.0	41.0	246.31	0.6637	0.7579	39.18
4	100.0	41.0	246.28	0.6589	0.7512	38.60

Table A.11.
Air-side indoor coil performance for economizer fault impact tests under different test conditions.

Test	γ_{oad}	$\dot{m}_{\text{sa}}$	h_{ma}	h_{sa}	$\dot{Q}_{\text{evap, air}}$	SHR
	%	kg/s	kJ/kg	kJ/kg	kW	–
			Condition 1			
0	10.0	0.7796	56.02	41.79	11.087	0.752
1	30.0	0.8107	57.39	43.05	11.629	0.771
2	50.0	0.7794	57.88	42.86	11.706	0.769
3	70.0	0.7853	58.70	43.01	12.319	0.775
			Condition 2			
0	20.0	0.7786	59.01	44.40	11.374	0.711
1	40.0	0.7755	60.82	45.64	11.776	0.697
2	60.0	0.7721	62.35	46.23	12.448	0.681
3	80.0	0.7840	62.64	46.67	12.518	0.698
			Condition 3			
0	0.0	0.7694	61.37	48.69	9.755	0.760
1	33.0	0.7614	67.47	52.59	11.326	0.724
2	50.0	0.7521	68.06	55.11	9.738	0.713
3	67.0	0.7579	71.49	55.92	11.802	0.704
4	100.0	0.7512	73.04	57.33	11.802	0.740